Tim Still

High Frequency Acoustics in Colloid-Based Meso- and Nanostructures by Spontaneous Brillouin Light Scattering

Springer

Springer Theses

Recognizing Outstanding Ph.D. Research

Aims and Scope

The series "Springer Theses" brings together a selection of the very best Ph.D. theses from around the world and across the physical sciences. Nominated and endorsed by two recognized specialists, each published volume has been selected for its scientific excellence and the high impact of its contents for the pertinent field of research. For greater accessibility to non-specialists, the published versions include an extended introduction, as well as a foreword by the student's supervisor explaining the special relevance of the work for the field. As a whole, the series will provide a valuable resource both for newcomers to the research fields described, and for other scientists seeking detailed background information on special questions. Finally, it provides an accredited documentation of the valuable contributions made by today's younger generation of scientists.

Theses are accepted into the series by invited nomination only and must fulfill all of the following criteria

- They must be written in good English.
- The topic of should fall within the confines of Chemistry, Physics and related interdisciplinary fields such as Materials, Nanoscience, Chemical Engineering, Complex Systems and Biophysics.
- The work reported in the thesis must represent a significant scientific advance.
- If the thesis includes previously published material, permission to reproduce this must be gained from the respective copyright holder.
- They must have been examined and passed during the 12 months prior to nomination.
- Each thesis should include a foreword by the supervisor outlining the significance of its content.
- The theses should have a clearly defined structure including an introduction accessible to scientists not expert in that particular field.

Tim Still

High Frequency Acoustics in Colloid-Based Meso- and Nanostructures by Spontaneous Brillouin Light Scattering

Doctoral Thesis performed at Max Planck Institute
for Polymer Research and accepted by
Johannes Gutenberg University,
Mainz, Germany

Author
Tim Still
Max Planck Institute for Polymer Research
Ackermannweg 10
55128, Mainz, Germany
still@mpip-mainz.mpg.de

Supervisor
Prof. Hans-Jürgen Butt
Max Planck Institute for Polymer Research
Ackermannweg 10
55128, Mainz, Germany
butt@mpip-mainz.mpg.de

Der Klügere gibt nach! Eine traurige Wahrheit,
sie begründet die Weltherrschaft der Dummheit.

(*The wiser man gives in! A distressing truth,*
it establishes the world domination of stupidity.)

Marie von Ebner-Eschenbach

Parts of this thesis have been published in the following journal articles:

T. Still, W. Cheng, M. Retsch, R. Sainidou, J. Wang, U. Jonas, N. Stefanou, G. Fytas, *Phys. Rev. Lett.* 2008, **100**, 194301. Copyright 2008 APS.

T. Still, W. Cheng, M. Retsch, U. Jonas, G. Fytas, *J. Phys. Condens. Matt.* 2008, **20**, 404203. Copyright 2008 IOP.

T. Still, R. Sainidou, M. Retsch, U. Jonas, P. Spahn, G. P. Hellmann, G. Fytas, *Nano Lett.* 2008, **8**, 3194. Copyright 2008 American Chemical Society.

T. Still, M. D'Acunzi, D. Vollmer, G. Fytas, *J. Coll. Interf. Sci.* 2009, **340**, 42. Copyright 2009, Elsevier, Inc. All rights reserved.

K. Kearns, T. Still (equal contribution), G. Fytas, M. D. Ediger, *Adv. Mater.* 2010, **22**, 39. Copyright 2010 Wiley-VCH.

T. Still, M. Retsch, U. Jonas, R. Sainidou, P. Rembert, K. Mpoukouvalas, G. Fytas, *Macromolecules* 2010, **43**, 3422. Copyright 2010 American Chemical Society.

Supervisor's Foreword

Materials that can mold the flow of elastic waves of certain energy in certain directions are called *phononic* materials. The present thesis deals essentially with such phononic systems, which are structured in the *mesoscale* (<1 μm), and with their individual components. Such systems show interesting phononic properties in the *hypersonic* region, i.e., at frequencies in the GHz range. It is shown that *colloidal systems* are excellent model systems for the realization of such phononic materials. Therefore, different structures and particle architectures are investigated by Brillouin light scattering, the inelastic scattering of light by phonons.

Both the mechanical properties of the individual colloidal particles, which manifest in their resonance vibrations (*eigenmodes*), as well as the acoustic propagation in colloidal structures have been investigated. The measurement of the eigenmodes allows for new insights into physical properties at the mesoscale, e.g., confinement effects, copolymer behavior, or the non-destructive determination of nanomechanical properties of core–shell particles, supporting the working groups aim to achieve a deeper understanding of 'soft mechanics' at small length scales. Another novel contribution assigned to this thesis is the first experimental realization of a phononic band gap arising from the interaction of these particle eigenmodes with the effective medium band (*hybridization gap*). This finding already gave new impulses to the whole field of phononics.

The thesis was performed between 03/2007 and 08/2009 at Max Planck Institute for Polymer Research, leading to several publications and presentations in international conferences, and was honored *summa cum laude* by the University of Mainz.

Mainz, March 2010   Prof. Dr. H.-J. Butt

Acknowledgments

Contents

Abbreviations

2D	Two-dimensional
3D	Three-dimensional
α	Angle incident laser/sample
α_η	Mark–Houwink parameter
$\beta_{(T,S)}$	(Isothermal, adiabatic) compressibility
ϵ	Dielectric constant
ϵ	Extinction coefficient
ϕ	Glancing angle
φ, ψ, χ	Scalar functions
Γ	Central point of *fcc* BZ
η	Viscosity
λ	Wave length
λ	Lamé coefficient
Λ	Phonon periodicity
μ	Lamé coefficient
v	Velocity of light in vacuum
θ	Scattering angle
ϱ	Mass density
σ	Poisson's ratio
σ	Scattering cross section
$\hat{\sigma}$	Normalized scattering cross section
σ_{ik}	Stress tensor
τ	Correlation time
ζ	Tandem FP angle
ω	Angular frequency
A	Free energy
A	Area under the curve
A	Absorbance
$A_{lml'm'}$	Structure constants
BLS	Brillouin light scattering
*n*BA	*n*-Butyl acrylate

BG	Bragg gap
c_F	Coefficient of finesse
$c_{l/t/\text{eff}}$	(Longitudinal/transverse/effective) sound velocity
$C_{p/T}$	Specific heat (at constant p/T)
C_{ik}	Components of the stiffness matrix
CCD	Charge-coupled device
d	Diameter
$d_{1/2}$	FP mirror distances
D	Diffusion coefficient
DOS	Density of states
DSC	Differential scanning calorimetry
DTA	Differential thermo analysis
DVB	Divenyl benzene
E	Young's modulus
$\boldsymbol{E}$	Electric field
E_0	Field amplitude
EMT	Effective medium theory
f	Frequency
F	Finesse
$\boldsymbol{F}$	Force
$f_{lm}(r, \theta, \phi)$	Solution of the scalar Helmholtz equation
fcc	Face centered cubic
FP	Fabry–Pérot interferometer
FSR	Free spectral range
G	Green's function
$\boldsymbol{G}$	Reciprocal space vector
$G(q, \tau)$	Time–correlation function
$g^2(q, \tau)$	Second order autocorrelation
GPC	Gel permeation chromatography
$h, \hbar$	Planck quantum ($/2\pi$)
hcp	Hexagonal close packing
HG	Hybridization gap
I	(Scattering) intensity
$\boldsymbol{I}$	Unit tensor
IMC	Indomethacin
k_B	Boltzmann's constant
KPS	Potassium persulfate
K	Gordon–Taylor parameter
K	Bulk modulus
K_η	Mark–Houwink parameter
$\boldsymbol{k}_{(i/sc)}$	(Incident/scattered) Wave vector
l	Longitudinal
L	Distinct point in reciprocal fcc lattice
L	Shear modulus
$\boldsymbol{l}, \boldsymbol{m}, \boldsymbol{n}$	Three independent vectors

LMS	Layer multiple scattering method
M	Distinct point in reciprocal *fcc* lattice
MMA	Methyl methacrylate
MPIP	Max Planck Institute for Polymer Research
MS	Multiple scattering method
m	Mass
m_e	Electron mass
M_n	Number averaged molecular weight
M_w	Weight averaged molecular weight
n	Refractive index
$\boldsymbol{n}_i$	Unit vector
NaPSS	Sodium sulfonated polystyrene
Nd:YAG	Neodym doped yttrium aluminium garnet (laser)
OG	Ordinary glass
p	Pressure
p	Momentum
PnBA	Poly (*n*-butyl acrylate)
PCS	Photon correlation spectroscopy
PDI	Polydispersity
PS	Polystyrene
PW	Plane wave method
PMMA	Poly (methyl methacrylate)
$\boldsymbol{q}$	Scattering wave vector
q	Absolute value of $\boldsymbol{q}$
$\boldsymbol{q}_{\text{para}}$	$\boldsymbol{q}$ Parallel to the sample plane
$\boldsymbol{q}_{\text{perp}}$	$\boldsymbol{q}$ Perpendicular to the sample plane
Q	Heat
r	Radius
$\boldsymbol{r}$	Space vector
R	Reflectivity
R	Rigidity
$\boldsymbol{R}$	Position vector
R	Absolute value of $\boldsymbol{R}$
R_h	Hydrodynamic radius
$R_l(k, r)$	Spherical Bessel functions
$\boldsymbol{R}_n$	Bloch's vector
RS	Raman scattering
S	Entropy
SCC	Supercooled liquid
SEM	Scanning electron microscope
SG	Stable glass
$\boldsymbol{T}$	T-Matrix
t	Time
t	Transverse
T	Temperature

T	Transmittance
TEM	Transmission electron microscope
TNB	$\alpha\alpha\beta$-1,3,5-tris-Naphthylbenzene
$\boldsymbol{u}$	Displacement vector
u_{ik}	Strain tensor
UV/VIS	Ultraviolet/visible light (spectroscopy)
V	(Scattering) volume
v	Velocity
w	Work
w	Relative width of a band gap
w_c	Degree of crystallization
X	Distinct point in reciprocal *fcc* lattice
$x(n, l)$	Eigenmode constant
Y_{lm}	Spherical harmonics

Chapter 1
Introduction

1.1 General Introduction

One of the most excitatory and technically promising new field in physics in the last decades was for sure the emerging possibility to control and manipulate the flow of light by engineering of macroscopic media with periodic dielectric function, i.e., with periodic variation of the refractive index in one, two, or three dimensions (Fig. 1.1). Since the first realization of such *photonic crystals*, an abundance of publications on this topic have been released, including several new high impact journals. Beside some quantum mechanical effects, the striking capability of a photonic crystal is its aptitude to prevent light from propagating in certain directions with specified frequencies, while they can operate as omnidirectional reflectors of light, independent from angle and polarization [1]. If the propagation of electromagnetic waves is forbidden at certain frequencies, one speaks about a *photonic band gap*.

The appearance of band gaps for distinct wavelengths in materials with periodic changed dielectric constant ϵ can be rationalized as an interference effect. The light is partially reflected at each layer interface. The multiple reflection interfere, and if the periodicity spacing is commensurate to the wavelength of the incident light, the destructive interference eliminates the forward propagation of the electromagnetic wave. In the simplest case of a one-dimensional (1D) photonic crystal, i.e., with periodic modulation of ϵ only in z-direction, with normal incident light, the gap occurs when the wavelength of the light λ_l is twice the crystals spatial period a, $\lambda_l = 2a$. In the concept of the reciprocal space that is commonly used in solid state physics, this belongs to a wave vector $k = 2\pi/\lambda_l$ (in this case k is identical to its component in z-direction) at the edge of the first Brillouin zone, i.e., $k = \pi/a$. The problem was first treated by Lord Rayleigh (1887), and such gap is usually called *Bragg gap*. It can be shown that the width of such a photonic gap depends on the dielectric contrast between the two components.

The concepts presented for the molding of electromagnetic waves can, in principle, be transferred to *mechanical waves*, i.e., sound waves. A material with
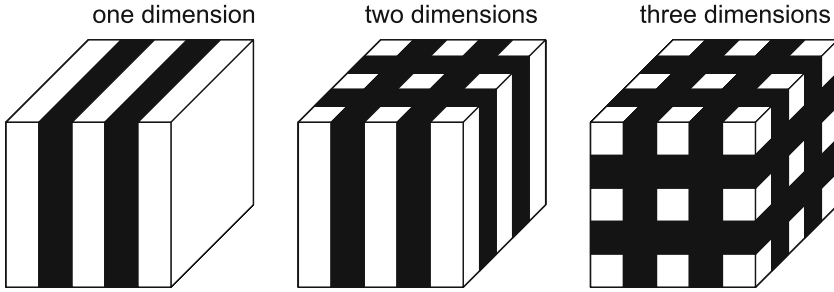
Fig. 1.1 Photonic or phononic crystals with periodicity in one, two, or three directions. In photonic crystals, *white* and *black* segments have different refractive index, while in phononic crystals the components must have different elastic moduli or densities

periodic modulation of the elastic properties, i.e., of the elastic moduli or the density, is called a *phononic crystal* after the quantized mode of vibration in a rigid crystal lattice—the phonon (in analogy to the photon in the photonic crystals) [2, 3]. However, the theoretical treatment of the propagation of mechanical waves is more complicated. While the light propagation can be fully described by a wave with distinct polarization and velocity, which depends on the refractive index of the passed medium, a mechanical wave can, in principle, propagate in two different ways.

Both mechanisms are schematically shown in Fig. 1.2. The longitudinal sound wave on the left side shows displacement along the propagation direction, while in the transverse sound wave the displacement is perpendicular to the propagation direction symbolized by the phonon wave vector **k**. Both waves propagate with different sound velocities c_l (longitudinal) or c_t (transverse), respectively. The relevant propagation mechanisms depend on the type of the material. In solid materials, both kind of waves can propagate, while in liquid or gaseous media only longitudinal waves are supported. Hence, the different mechanical waves are often distinguished between *elastic waves* in solids and *acoustic waves* in fluids. However, in this thesis the terms elastic wave, acoustic wave, or sound wave will be used synonymously for all kinds of mechanical waves.
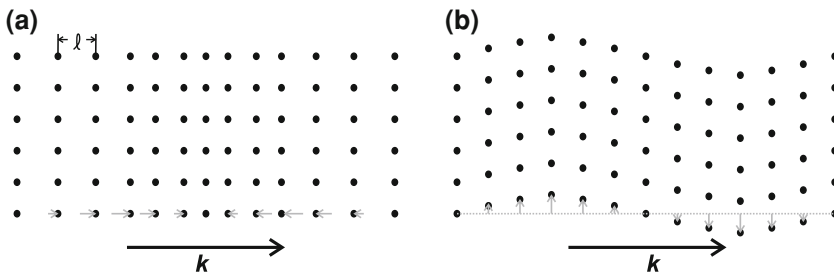
Fig. 1.2 Propagation mechanisms of mechanical waves: **a** longitudinal wave with displacement along the propagation direction (given by the direction of the wave vector **k**); **b** transverse sound wave with displacement perpendicular to the propagation direction

On an atomic scale, the concept of the phonon is used to describe for example the heat capacity of solids. The frequencies of the allowed mechanical waves are quantized as a function of the distance ℓ between neighboring atoms. The atoms (the black points in Fig. 1.2) are displaced, and the displacement of each atom is described by the displacement vector $\mathbf{u}(\mathbf{r}, t)$ as a function of position and time.

However, in this thesis the interest lays on much lower frequencies with phonon wavelength $\Lambda \gg \ell$, thus the allowed mechanical frequencies can be regarded as continuous. Figure 1.2 holds also in this case, but now the points represent volume elements containing many atoms. It should be noted that the spatial displacement of volume elements as a function of time leads to areas of instantaneously increased or decreased pressure (or local density), thus mechanical waves can be regarded as pressure waves. This picture also rationalizes why there is no propagation of transverse sound waves in fluids since fluids do not support shear (aside from very viscous liquids).

Phononic crystals can be designed by a one-, two-, or three-dimensional periodicity of their elastic properties in analogy to their electromagnetic counterparts (Fig. 1.1). The geometry of the periodic structure has strong influence on its mechanical properties. One of the first examples of a two-dimensional phononic crystal is a statue in Madrid, created by the artist E. Sempere [4]. The piece of art consist of a large number of hollow stainless-steel cylinders with diameter of 2.9 cm in a simple cubic arrangement in a $a = 10$ cm unit cell, the whole statue has a diameter of 4 m. A simple transmission experiment with a sound generator and detector in the range of audible frequencies (1–5 kHz) has shown the existence of phononic band gaps with strong sound attenuation depending on the orientation of source and receiver relative to the statue, i.e., as a function of the crystallographic direction.

Like in the case of photonic crystals, the Bragg gap appears at the edge of the first Brillouin zone, i.e., the phonon wavelength Λ is twice the lattice parameter a, $\Lambda = 2a$, and the corresponding wave vector is again $k = \pi/a$. The frequency is given by $2\pi f = c_l/\Lambda$. Since typical sound velocities are between 10^2 ms^{-1} (air) and 10^5 ms^{-1} (condensed matter), attenuation in the audible range requires periodicities in the centimeter to meter range, like in the example of the statue. Structures that would attenuate seismic waves would have to be constructed even in kilometer scales, the Bragg frequency scales with $1/a$. According to this, smaller, technically handier structures with spacing in the millimeter, micrometer, or even nanometer-scale correspond to frequencies in the MHz to THz scale.

Most of the realized phononic band gap systems are restricted to sonic and ultrasonic crystals with macroscopic periodicity, e.g., some millimeter-sized crystals assembled manually, which could be probed by simple acoustic transmission experiments in the commensurate frequency ranges [5–7]. Only recently, Cheng et al. [8] could show the realization of a hypersonic phononic crystal based on the self-assembly of sub-micron colloidal polymer crystals [9].

In fact, such mesoscopic structures have some advantages. They can be easily prepared by self-assembly methods or by interference lithography [3] on a (relative to the lattice spacing) large scale, they can show photo-thermal or photo-acoustic

effects, and their size is also commensurate to the wavelength of visible light. Therefore, it is possible to create a mesoscopic artificial crystal with periodic variation of refractive index and mechanical properties, which would act as a photonic and phononic crystal simultaneously. Sometimes, such 'blind and deaf' systems are called *phoXonic crystals* [10, 11]. Due to their size, colloidal crystals from mesoscopic spheres show nice colorful reflections of light depending on the scattering angle relative to their crystallographic direction as it can be found in natural opals. Therefore, such systems are often (also in the present thesis) called *artificial opals*. Figure 1.3 shows three photographs of a polished natural opal, an artificial opal, which consists of dense packed silica spheres ($d = 170$ nm) in a organic liquid matrix, and a layer of polystyrene spheres ($d = 550$ nm) on a glass substrate.

These artificial opals are examples for *colloid* particle systems. In general, a colloid is a particle or droplet of typical size between 1 nm and 10 μm that is dispersed in another gaseous, liquid, or solid medium, e.g., milk (fat droplets in water), fume (solid particles in gas), blood (solid particles in liquid), etc. In this thesis the word colloid is used in a less general way; here it means in particular the well defined colloidal solid particles, which are fabricated by the methods of material chemistry. Systems of these particles in a matrix material are referred to as *colloidal systems*.

Such colloidal systems have many advantages. Due to the onward development of colloidal and material science, nowadays it became possible to control a wide range of properties during the synthesis of colloids. Monodisperse spherical particles can be produced in a size range from few tens of nanometer to several microns, utilizing a wide range of materials like metals, oxides (e.g., silica), or
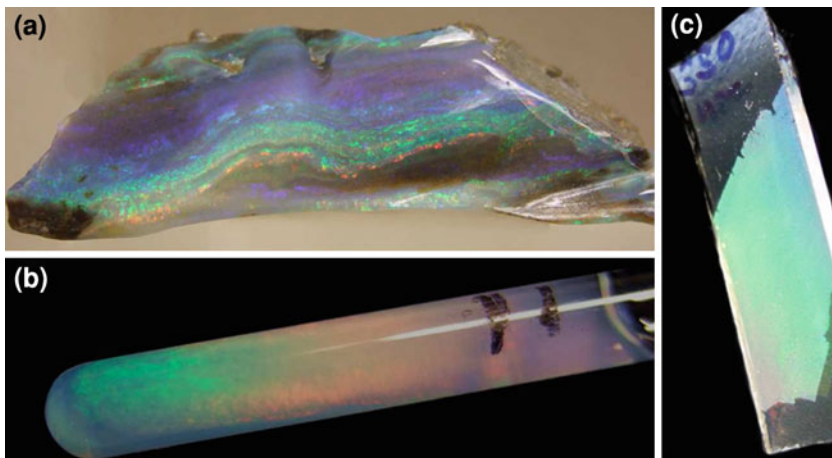
Fig. 1.3 Natural and artificial opals: **a** Natural opal (Australia, Museum Idar-Oberstein, Germany); **b** dense packed silica spheres ($d = 219$ nm, DKI Darmstadt) in organic liquid; **c** PS spheres ($d = 550$ nm, M. Retsch, MPIP) on glass substrate

(organic) polymers. However, colloid science is not generally limited to spherical particle shape. For metals, and with limitations for the form stability also for oxides, even smaller nanoparticles can be created. Mesoscopic colloids can be additionally structured in the nanoscale to manipulate or improve their physical and chemical properties, leading, e.g., to spherical hybrid core–shell particles investigated also in this thesis [12]. Another already mentioned advantage is the possibility to realize well ordered single or multi-component systems by self-assembly (colloidal crystals). In Fig. 3.1 (in Chap. 3) several techniques to achieve colloidal crystals will be presented, including sedimentation [13], electrodeposition [14], centrifugation, filtering, vertical deposition [15, 16], and compression molding [17]. Especially the last two techniques play a role in this thesis and will be introduced in more detail in the Sects. 3.1 and 3.2 in Chap. 3.

Since colloids exhibit outstanding physical and chemical properties (e.g., large surface, optical properties, solubility, etc.) and tunability (size, shape, softness, biodegradability, etc.) [18–20], this class of materials found numerous technical applications, e.g., in suspensions as pigment or sunscreen [21], for drug-delivery applications [22], or to improve the macroscopic mechanical properties of solids or polymers [23].

This thesis is devoted to the investigation of the acoustic, i.e., phononic, properties of colloidal particles and systems, which appear heterogeneous compared to the sound wavelength. Hence, rich unprecedented behavior is expected due to the large number of parameters involved and the sensitivity of elastic wave propagation to boundary conditions. As already pointed out, the characteristic frequencies scale with the inverse size of the observed systems, for mesoscopic colloids hypersound, i.e., GHz frequencies, become relevant. Such high frequencies are not accessible anymore by 'simple' sound generation and subsequent detection with membranes (audible sound) or piezo crystals (ultrasound). In fact, when measuring the sound propagating in a material, it is not absolutely necessary to generate the hypersound artificially, since hypersonic phonons are thermally excited at temperatures far away from 0 K [24]. These phonons can be probed by inelastic light scattering, i.e., spontaneous Brillouin light scattering (BLS) in the GHz-range (related to the mesoscopic length scale) and Raman scattering in the THz-range (for the nanoscopic length scale) [25, 26]. Another possibility is pump-probe spectroscopy, where a strong laser pulse impinges on a sample and a second probe laser is used to measure the reflectivity of the sample as a function of time [27, 28]. After Fourier transformation that approach also delivers information about the frequencies of sound in the probed material, however, after an induced perturbation and not spontaneously.

In this thesis, BLS is utilized to probe phonon propagation (and localization) in micro- and nanostructures. The main principle of this unique non-destructive and non-contact optical technique is the interaction of photon and phonon. In fact, the photons of the probing single-frequency laser light are scattered inelastically on the phonons in the probed material propagating along a selected direction, which is given by the scattering wavevector $\mathbf{q}$ that is a function of the scattering angle and the sample's refractive index. In homogeneous systems the interacting phonon is

the one whose phonon wavevector $\mathbf{k}$ is identical with $\mathbf{q}$ as a consequence of momentum conservation. Therefore, the BLS spectrum at a given $\mathbf{q}$ consists of a Doppler shift at angular frequencies $\omega = \pm c_{l,t} k$ for longitudinal (l) or transverse (t) sound velocity c. With other words, we measure the frequency shift of the probing light due to the creation or annihilation of a phonon as a function of the momentum (the magnitude of the wave vector) leading to the dispersion relation $\omega(\mathbf{q})$. The achieved frequency shifts in the GHz-range are tiny compared to the frequency of the laser light (10^{14} Hz), the required high resolution is attained by a multi-pass tandem Fabry–Pérot interferometer [29].

Of course, the use of BLS to investigate the mechanical properties of matter is not limited to colloidal systems. The last chapter of this thesis shows how BLS can be used to investigate the mechanics and kinetics of so-called stable organic glasses, i.e., organic glasses that are created by very slow vapor deposition on a temperate substrate [30, 31]. By doing so, the molecules have more time to rearrange in an energetically more favorable way, leading to elastic moduli comparable to normal glasses that are aged for at least several hundred years.

1.2 Aims and Motivation

Colloids are very promising systems in many terms. They are auspicious candidates to design hypersonic phononic systems that may be the basis of elaborated devices that deal with the concurrent interaction of phonons and light (functional phoXonic materials). However, so far there is no large knowledge about the details of the nano- and mesomechanical behavior of individual colloids and the manipulation of sound propagation in colloidal systems beyond the simple Bragg gap [8].

In this thesis a systematic approach is presented that captures the influence of different parameters on the mechanical waves localized in spherical (as the most accessible and theoretically best to capture model system), partially nanostructured, mesoscopic colloids as well as the propagation of sound waves in systems composed of such particles [12, 32]. The first realization of a so-called *hybridization gap* in polymer based colloids will be presented, which originates from the interaction between individual and collective colloid mechanical properties, leading to crystalline as well as amorphous omnidirectional hypersonic band gap systems [33].

These developments, however, must not be regarded as the end of the basic experimental investigation of such systems. It will be shown that for silica based systems with increasing mechanical contrast new effects occur, which will demand further strong efforts in the theoretical and experimental conquest of this young and promising field. Especially in consideration of the numerous appearing topics related to photo-acoustics [34], thermo-acoustics [35], or nano- and micromechanics [36, 37], it seems worth to investigate colloidal model systems *en detail* and the intimate relation of the heat conductivity in dielectric materials on phonons

can have impact on a directional heat flow in the future. This work may be a humble contribution to this exciting development.

1.3 Outline

The structure of this thesis is as follows:

In this chapter I introduce the theoretical and practical basics of the propagation of elastic waves and of light scattering, in particular of Brillouin light scattering and its applicability to colloidal particles and colloid based systems.

The second chapter is about other methods utilized in this thesis, including the theoretical calculations that are needed to quantitatively describe the experimental findings. If these first two chapters might appear to extend some few details beyond the absolutely necessary length, this is caused by the aim to present the important results in a common notation, which is not the case in the underlaying literature.

Chapter 4 describes the work done on the vibrations of individual colloids that can be investigated in multiple scattering or thick transparent samples. Herein, the influences of packing in a sample consisting of many spheres and that of the sphere material is reported as well as the discussion of general theoretical problems and their experimental answer concerning the selection rules for eigenvibrations in BLS and the light scattering intensity as a function of $\mathbf{q}$.

The next chapter proceeds to the collective phononic behavior, i.e., the propagation of sound waves, in colloidal systems embedded in a solid or liquid matrix. Starting from a short description of the state-of-the-art, the experimentally found effective medium velocities are discussed and a new kind of phononic band gap, the hybridization gap, is presented. It is demonstrated by the investigation of silica based colloidal systems that there seem to be additional mechanisms to manipulate the phononic band diagram.

Chapter 6 is the last experimental chapter and deviates from the scope on colloids in the other parts of the thesis since it is about the characterization of stable organic glasses.

Finally, this thesis concludes with main results and outlook in the concluding remarks (Chap. 7).

References

1. Joannopoulos JD, Johnson SG, Winn JN, Meade RD (2008) Photonic crystals: molding the flow of light, 2nd edn. Princeton University Press, Princeton
2. Economou EN, Zdetsis A (1989) Phys Rev B 40:1334
3. Maldovan M, Thomas EL (2008) Periodic materials and interference lithography. Wiley-VCH, New York
4. Martinez-Salazar R et al (1995) Nature 378:241

5. Montero de Espinosa FR, Jiménez E, Torres M (1998) Phys Rev Lett 80:1208
6. Liu ZY et al (2000) Science 289:1734
7. Vasseur JO et al (2001) Phys Rev Lett 86:3012
8. Cheng W et al (2006) Nat Mater 5:830
9. Thomas EL, Gorishnyy T, Maldovan M (2006) Nat Mater 5:773
10. Gorishnyy T, Maldovan M, Ullal C, Thomas E (2005) Phys World 18:24
11. Bernal MP, Roussey M, Baida F, Benchabane S, Khelif A, Laude V (2008) In: Ferraro P, Grilli S, De Natale P (eds) Ferroelectric crystals for photonic applications, vol 307. Springer, Heidelberg, pp 307–336
12. Still T et al (2008) Nano Lett 8:3194
13. Davis KE, Russel WB, Glantschnig WJ (1989) Science 245:507
14. Trau M, Saville DA, Aksay IA (1996) Science 272:706
15. Jiang P, Bertone JF, Hwang KS, Colvin VL (1999) Chem Mater 11:2132
16. Gu ZZ, Fujishima A, Sato O (2002) Chem Mater 14:760
17. Ruhl T, Spahn P, Hellmann GP (2003) Polymer 44:7625
18. Lyklema J (1991) Fundamentals of interface and colloid science. Academic Press, London
19. Lyklema J (2005) Fundamentals of interface and colloid science IV. Elsevier, London
20. Lyklema J (2005) Fundamentals of interface and colloid science V. Elsevier, Amsterdam
21. Magdassi S, Bassa A, Vinetsky Y, Kamyshny A (2003) Chem Mater 15:2208
22. Müller RH, Mäder K, Gohla S (2000) Eur J Pharm Biopharm 50:161
23. Pichot F, Pitts JR, Gregg BA (2000) Langmuir 16:5626
24. Meschede D (2006) Gerthsen Physik, 23rd edn. Springer, Heidelberg
25. Brillouin L (1922) Ann Phys (Paris) 17:88
26. Raman VV, Krishnan KS (1928) Nature 121:501
27. Mazurenko DA et al (2007) Phys Rev B 75:161102
28. Akimov AV et al (2008) Phys Rev Lett 101:033902
29. Mock R, Hillebrands B, Sandercock JR (1987) J Phys E Sci Instrum 20:656
30. Dyre JC, Olsen NB, Christensen T (1996) Phys Rev B 53:2171
31. Swallen SF et al (2007) Science 315:353
32. Still T et al (2008) J Phys Condens Matter 20:404203
33. Still T et al (2008) Phys Rev Lett 100:194301
34. Kippenberg TJ, Vahala KJ (2008) Science 321:1172
35. Damen EPN, Arts AFM, de Wijn HW (1995) Phys Rev Lett 74:4249
36. Cheng W et al (2008) Nano Lett 8:1423
37. Schliesser A et al (2008) New J Phys 10:095015

Chapter 2
Basics and Brillouin Light Scattering

In this chapter, first the basic expressions of elasticity will be introduced, especially with regard to the propagation of elastic waves in isotropic media and their description as spherical waves. Then the general principles of light scattering will be presented and applied to the special case of Brillouin light scattering, including the discussion of its technical realization.

2.1 Elastic Waves in Condensed Matter

2.1.1 Elasticity Theory Basics

In this part, fundamental concepts of the theory of elasticity are briefly introduced, following mostly the notation of the excellent textbook of Landau and Lifschitz [1].

Essential terms are the strain and stress tensors. To introduce them, we first define the displacement vector $\boldsymbol{u}$ that shifted a point P that can be found by following the vector $\boldsymbol{r}$ (with the three components $x_1 = x$, $x_2 = y$, and $x_3 = z$ in a Cartesian system) from the origin of the coordinate system to the point P' with coordinates given by the vector $\boldsymbol{r}'$, i.e.,

$$\boldsymbol{u} = \boldsymbol{r} - \boldsymbol{r}'. \tag{2.1}$$

The distance between any two infinitesimally adjacent points dl is given by

$$dl = \sqrt{dx_1^2 + dx_2^2 + dx_3^2} = \sqrt{dx_i^2}, \tag{2.2}$$

using the Einstein summation convention behind the second equal. After a deformation it becomes

$$dl' = \sqrt{dx_1'^2 + dx_2'^2 + dx_3'^2} = \sqrt{dx_i'^2} \tag{2.3}$$

Therefore, it is possible to write

$$dl'^2 = dx_i'^2 = (dx_i + du_i)^2 = dl^2 + 2\frac{\partial u_i}{\partial x_k}dx_idx_k + \frac{\partial u_i}{\partial x_k}\frac{\partial u_i}{\partial x_l}dx_kdx_l \tag{2.4}$$

substituting $du_i = \frac{\partial u_i}{\partial x_k}dx_k$ in the last step. With $\frac{\partial u_i}{\partial x_k}dx_idx_k = \frac{\partial u_k}{\partial x_i}dx_idx_k$ and swap of i and l in the last term, finally we get

$$dl'^2 = dl^2 + 2u_{ik}dx_idx_k. \tag{2.5}$$

The strain tensor u_{ik} is therein defined as

$$u_{ik} = \frac{1}{2}\left(\frac{\partial u_i}{\partial x_k} + \frac{\partial u_k}{\partial x_i} + \frac{\partial u_l}{\partial x_k}\cdot\frac{\partial u_l}{\partial x_i}\right) \approx \frac{1}{2}\left(\frac{\partial u_i}{\partial x_k} + \frac{\partial u_k}{\partial x_i}\right). \tag{2.6}$$

The last approximation is valid if second order terms can be neglected. Obviously, u_{ik} is a symmetric tensor. Each symmetric tensor can be diagonalized in any point. With the diagonal elements $u^{(1)}$, $u^{(2)}$, $u^{(3)}$ the strain in any point can be written as the sum of three independent terms, which give the strain in three orthogonal main directions.

$$dl'^2 = (1 + 2u^{(1)})dx_1^2 + (1 + 2u^{(2)})dx_2^2 + (1 + 2u^{(3)})dx_3^2. \tag{2.7}$$

For $u^{(i)} \ll 1$ and if higher order terms are neglected, the relative change of elongation becomes

$$\frac{dx_i' - dx_i}{dx_i} = \sqrt{1 + 2u^{(i)}} - 1 \approx u^{(i)}. \tag{2.8}$$

With that approximation we can write the relative volume change of an infinitesimal small volume element $dV \rightarrow dV'$ as the sum of the diagonal elements of the strain tensor [1].

$$\frac{dV' - dV}{dV} = u_{ii}. \tag{2.9}$$

The resulting force $\boldsymbol{F}$ on any partial volume of an elastic body can be written as the integral over the forces on any element of the volume $\int \boldsymbol{F}dV$. Because of the identity of actio and reactio for all forces between any two points within the volume the resulting force can also be written as the sum over the integrals of the three components F_i, $\int F_idV$, which can be translated into an integral over the surface:

$$\int F_idV = \int \frac{\partial \sigma_{ik}}{\partial x_k}dV = \oint \sigma_{ik}df_k. \tag{2.10}$$

Here, F_i is expressed as divergence of a second rank tensor, the stress tensor σ_{ik}:

$$F_i = \frac{\partial \sigma_{ik}}{\partial x_k} \tag{2.11}$$

In Eq. 2.10, df_i are the components of a vector that is always oriented in the direction normal to the surfaces. The nature of the stress tensor is visualized in Fig. 2.1. When placing the surfaces of the volume element in the principal plane of the coordinate system (xy, yz, or xz), the component σ_{ab} of the stress tensor equals to the a-component of the force that is normal to that x_b-axis.

The work δw that is achieved to perform a deformation is

$$\delta w = -\sigma_{ik}\delta u_{ik}. \tag{2.12}$$

For reversible, elastic deformations it follows for the free energy A ($A = U - TS$, $dU = TdS - \delta w$, S: entropy) that

$$\sigma_{ik} = \left(\frac{\partial A}{\partial u_{ik}}\right)_T. \tag{2.13}$$

It can be shown that the free energy after an elastic isothermal deformation of an isotropic body can be expressed after series expansion and neglecting higher order terms as

$$A = A_0 + \frac{\lambda}{2}u_{ii}^2 + \mu u_{ik}^2, \tag{2.14}$$

introducing the Lamé coefficients λ and μ. Note that λ and μ are force constants. Since it was already shown that the volume change during a deformation is expressed by the sum of the diagonal elements u_{ii}, it is obvious that, if the term containing the u_{ii} becomes zero, the last term expresses a pure shear deformation. Therefore, μ is also called the shear modulus, sometimes denoted by G.

Fig. 2.1 Illustration of the stress tensor for the σ_{ax}-components working on a surface normal to the x-axis. The picture is analogously valid for the other six components when applied to the surfaces normal to the y- and z-axis
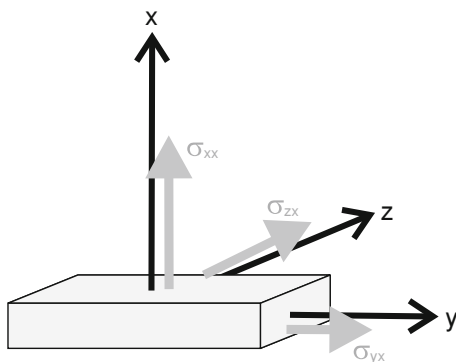
By writing the following identity

$$u_{ik} = \left(u_{ik} - \frac{1}{3}\delta_{ik}u_{ll} \right) + \frac{1}{3}\delta_{ik}u_{ll} \tag{2.15}$$

with $u_{ik} = \text{const} \cdot \delta_{ik}$ it follows directly that every deformation can be written as a sum of a pure shear deformation and a homogeneous dilatation. The term in brackets is surely a pure shear deformation, because the sum of the diagonal elements vanishes ($\delta_{ii} = 3$) and the other term is related to the homogeneous dilatation.

For a perfectly elastic body, Hook's law can be generalized to state that each component of the stress tensor is linearly related to each component of the strain tensor:

$$\sigma_{ik} = c_{iklm}u_{lm}. \tag{2.16}$$

Here, c_{iklm} is the fourth-rank stiffness tensor with $3^4 = 81$ components. Taking into account the symmetry of the strain and stress tensors, it is possible to reduce the number of coefficients to $6^2 = 36$. However, these 36 components are not independent. In the general case the following symmetry relations are valid:

$$c_{iklm} = c_{kilm} = c_{ikml} = c_{kiml}. \tag{2.17}$$

That is in an anisotropic body there are at most 21 independent components, which are usually noted in a matrix notation, which uses the itemized identities to abbreviate the tensor notation and to replace the tensor by a 6×6-matrix with only two indices per component. The following rules are adopted for the indices:

Tensor notation	11	22	33	23, 32	13, 31	12, 21
Matrix notation	1	2	3	4	5	6

With that notation one can rewrite Eq. 2.16 as

$$\begin{bmatrix} \sigma_1 \\ \sigma_2 \\ \sigma_3 \\ \sigma_4 \\ \sigma_5 \\ \sigma_6 \end{bmatrix} = \begin{bmatrix} C_{11} & C_{12} & C_{13} & C_{14} & C_{15} & C_{16} \\ C_{12} & C_{22} & C_{23} & C_{24} & C_{25} & C_{26} \\ C_{13} & C_{23} & C_{33} & C_{34} & C_{35} & C_{36} \\ C_{14} & C_{24} & C_{34} & C_{44} & C_{45} & C_{46} \\ C_{15} & C_{25} & C_{35} & C_{45} & C_{55} & C_{56} \\ C_{16} & C_{26} & C_{36} & C_{46} & C_{56} & C_{66} \end{bmatrix} \begin{bmatrix} u_1 \\ u_2 \\ u_3 \\ u_4 \\ u_5 \\ u_6 \end{bmatrix}. \tag{2.18}$$

While the discussion of the stiffness matrix for different crystal symmetries is done in specialized treatments, here only the isotropic case, which is a good approximation for many cases, including also most polymer systems, should be discussed in the rest of this section. For an isotropic body, it can be shown that

due to further symmetry considerations the stiffness matrix in Eq. 2.16 has the following form [2]:

$$
\begin{bmatrix}
\sigma_1 \\
\sigma_2 \\
\sigma_3 \\
\sigma_4 \\
\sigma_5 \\
\sigma_6
\end{bmatrix}
=
\begin{bmatrix}
C_{11} & C_{12} & C_{12} & 0 & 0 & 0 \\
C_{12} & C_{11} & C_{12} & 0 & 0 & 0 \\
C_{12} & C_{12} & C_{11} & 0 & 0 & 0 \\
0 & 0 & 0 & C_{44} & 0 & 0 \\
0 & 0 & 0 & 0 & C_{44} & 0 \\
0 & 0 & 0 & 0 & 0 & C_{44}
\end{bmatrix}
\begin{bmatrix}
u_1 \\
u_2 \\
u_3 \\
u_4 \\
u_5 \\
u_6
\end{bmatrix}.
\tag{2.19}
$$

Because the three remaining constants are related by the following relation

$$
C_{11} = C_{12} + 2C_{44},
\tag{2.20}
$$

there are, indeed, only two independent constants remaining. These two constants can be identified with the Lamé coefficients

$$
\lambda = C_{12} \quad \text{and} \quad \mu = C_{44},
\tag{2.21}
$$

while C_{11} is also called the longitudinal modulus. Beside the shear modulus $G = \mu$, some other elastic parameters are often encountered, namely the bulk modulus, the Young's modulus, or the Poisson's ratio.

The bulk modulus K measures a substance's resistance to uniform compressions. It is defined as the ratio of the hydrostatic pressure to the fractional volume change,

$$
K = -\frac{\partial p}{\partial u_{ii}} = \lambda + \frac{2}{3}\mu.
\tag{2.22}
$$

K should not be confused with the longitudinal bulk modulus

$$
M = C_{11}.
\tag{2.23}
$$

The Young's modulus E, also known as modulus of elasticity or tensile modulus, is a measure of the stiffness of an isotropic elastic material. It is given by the ratio of longitudinal stress (which has units of pressure) and the dimensionless longitudinal strain,

$$
E = \frac{\sigma_{11}}{u_{11}} = \frac{\mu(3\lambda + 2\mu)}{\lambda + \mu}.
\tag{2.24}
$$

The ratio of the lateral strain to the longitudinal strain defines the Poisson's ratio,

$$
\sigma = -\frac{u_{22}}{u_{11}} = \frac{\lambda}{2(\lambda + \mu)}.
\tag{2.25}
$$

2.1.2 Elastic Waves in Isotropic Media

When a body is deformed, the deformation usually goes along with changes in the temperature. However, the heat transport is normally much slower compared to periods of vibrations in the body. Therefore, one can regard the movements as (quasi)adiabatic. It can be shown that in the adiabatic case the values for the Young's modulus and the Poisson's ratio, given above for the isothermal case, change into

$$E_{\text{adiabatic}} = E + E^2 \frac{T\alpha^2}{9C_p} \quad \text{and} \quad \sigma_{\text{adiabatic}} = \sigma + (1+\sigma)E\frac{T\alpha^2}{9C_p}, \qquad (2.26)$$

where $\alpha = (\partial V/\partial T)_p$ and C_p is the specific heat at constant pressure [1]. In the following, σ and E mean their adiabatic values.

The general equation of movement can be written as

$$\varrho \frac{\partial^2 u_i}{\partial t^2} = \frac{\partial \sigma_{ik}}{\partial x_k} \qquad (2.27)$$

with mass density ϱ. For the isotropic elastic medium the equation of movement becomes

$$\varrho \frac{\partial^2 u_i}{\partial t^2} = \frac{E}{2(1+\sigma)} \nabla^2 u + \frac{E}{2(1+\sigma)(1-2\sigma)\text{grad div} u}. \qquad (2.28)$$

Regarding a plane elastic wave in x-direction in an infinite medium, i.e., the deformation u depends only on the x-coordinate (all derivatives with respect to y and z become zero), the components of the vector u become

$$\frac{\partial^2 u_x}{\partial x^2} - \frac{1}{c_l^2}\frac{\partial^2 u_x}{\partial t^2} = 0; \quad \frac{\partial^2 u_y}{\partial x^2} - \frac{1}{c_t^2}\frac{\partial^2 u_y}{\partial t^2} = 0; \quad \frac{\partial^2 u_z}{\partial x^2} - \frac{1}{c_t^2}\frac{\partial^2 u_z}{\partial t^2} = 0. \qquad (2.29)$$

The Eq. 2.29 are one-dimensional wave equations, c_l and c_t are their velocities of propagation. Obviously, the propagation in x-direction is different from that in the other directions. If the displacement u_x lies in the direction of propagation of the wave, the wave is called a longitudinal wave with longitudinal sound velocity c_l:

$$c_l = \sqrt{\frac{E(1-\sigma)}{\varrho(1+\sigma)(1-2\sigma)}} = \sqrt{\frac{\lambda + 2\mu}{\varrho}} = \sqrt{\frac{C_{11}}{\varrho}}. \qquad (2.30)$$

In the other directions, the displacement (u_y, u_z) lies in a plane normal to the direction of propagation of the wave. Such a wave is called a transverse wave with transverse sound velocity c_t:

$$c_t = \sqrt{\frac{E}{2\varrho(1+\sigma)}} = \sqrt{\frac{\mu}{\varrho}} = \sqrt{\frac{C_{44}}{\varrho}}. \qquad (2.31)$$

Accordingly, from Eqs. 2.21 and 2.23 it is clear that we can express longitudinal and shear modulus simply by

$$M = \varrho c_l^2 \qquad (2.32)$$

and

$$G = \varrho c_t^2, \qquad (2.33)$$

respectively, while the bulk modulus K depends on the longitudinal as well as on the transverse sound velocity, since after Eqs. 2.20 and 2.22 it becomes

$$K = M - 2G + \frac{2}{3}G = M - \frac{4}{3}G = \varrho\left(c_l^2 - \frac{4}{3}c_t^2\right). \qquad (2.34)$$

The longitudinal sound velocity is always larger than the transverse sound velocity. For $\sigma \leq 0.5$,

$$c_l > c_t\sqrt{2}. \qquad (2.35)$$

One should note that the transverse wave has two possible polarizations, which are orthogonal to each other. Furthermore, it is notable that longitudinal waves involve changes in the volume of the medium, i.e., dilatation or compression of a local volume element, while the transverse waves cause no volume change.

2.1.3 Spherical Waves

Because this thesis treats in many parts experiments on colloids acting as spherical scatterers, it is meaningful to introduce briefly the principle solution of the elastic wave equation for an isotropic medium. The equations presented here will be required again in the discussion of the vibrational eigenmodes of spherical particles.

In general, for a harmonic elastic wave of angular frequency ω, the displacement vector $\boldsymbol{u}$ can be written as

$$\boldsymbol{u}(\boldsymbol{r}, t) = \Re[\boldsymbol{u}(\boldsymbol{r})\exp(-i\omega t)]. \qquad (2.36)$$

Using that one can write the general equation of motion in the following time-independent form [3]:

$$(\lambda + 2\mu)\nabla(\nabla \cdot \boldsymbol{u}) - \mu\nabla \times \nabla \times \boldsymbol{u} + \varrho\omega^2\boldsymbol{u} = 0. \qquad (2.37)$$

In a spherical coordinate system, the displacement vector can be written as the sum of three vectors $\boldsymbol{u} = \boldsymbol{l} + \boldsymbol{m} + \boldsymbol{n}$ such that Eq. 2.37 can be broken into three independent vector Helmholtz equations [4]

$$(\nabla^2 + k_l^2)\boldsymbol{l} = 0, \quad (\nabla^2 + k_t^2)\boldsymbol{m} = 0, \quad (\nabla^2 + k_t^2)\boldsymbol{n} = 0, \tag{2.38}$$

where $\boldsymbol{l}$ represents the displacement associated with longitudinal wave and $\boldsymbol{n}$ and $\boldsymbol{m}$ represent the transverse displacements, which are orthogonal to each other. These three vectors can be related to scalar functions φ, ψ, and χ that are solutions of a scalar Helmholtz equation $(\nabla^2 + k^2)f = 0$:

$$\boldsymbol{l} = \frac{1}{k_l}\nabla\varphi, \tag{2.39}$$

$$\boldsymbol{m} = \nabla \times \boldsymbol{r}\psi, \tag{2.40}$$

$$\boldsymbol{n} = \frac{1}{k_t}\nabla \times \nabla \times \boldsymbol{r}\chi. \tag{2.41}$$

The transverse displacement vectors $\boldsymbol{m}$ and $\boldsymbol{n}$ are herein expressed as the product of the constant position vector $\boldsymbol{r}$ and the scalar functions mentioned above [4]. In polar coordinates the solution of the scalar Helmholtz equation is known. It is

$$f_{lm}(r, \theta, \phi) = R_l(kr)Y_{lm}(\theta, \phi). \tag{2.42}$$

$R_l(kr)$ are n-th order spherical Bessel functions, which represent the radial displacement. $Y_{lm}(\theta, \phi)$ are the n-th order spherical harmonics (Legendre functions) with $l = 0, 1, 2, 3, \ldots$ and m being an integer $-l \leq m \leq +l$. Knowing this, the vector solutions of Eq. 2.38 can be written as

$$\boldsymbol{l}_{lm}(R, k_l) = \frac{1}{k_l}\nabla[R_l(k_l r)Y_{lm}(\hat{r})]; \quad l = 0, 1, 2, 3, \ldots, \tag{2.43}$$

$$\boldsymbol{m}_{lm}(R, k_t) = \nabla \times [\boldsymbol{r}R_l(k_t r)Y_{lm}(\hat{r})]; \quad l = 1, 2, 3, \ldots, \tag{2.44}$$

$$\boldsymbol{n}_{lm}(R, k_t) = \frac{1}{k_t}\nabla \times \nabla \times [\boldsymbol{r}R_l(k_t r)Y_{lm}(\hat{r})]; \quad l = 1, 2, 3, \ldots \tag{2.45}$$

2.2 Light Scattering Basics

This section is a brief introduction into the basic principles of light scattering. While the derivation of scattering theory on the basis of quantum field theory is possible, herein the scattering medium as well as the light are treated classically, leading to practically the same results within the scope of this thesis. Of course there are light scattering effects, as for example the well-known Raman scattering technique, which deals with rotational and vibrational transitions of single atoms or molecules, i.e., effects in a quantum length scale, that must be treated (at least partially) quantum mechanically. However, this thesis deals with the investigation of phonons by Brillouin light scattering (Sect. 2.3) in condensed

matter. Thus the investigated phonons are classical waves with wavelengths in the order of some nanometer up to micrometer, it is fully justified to apply a classic theory.

The classical theory of light scattering in dense media developed by Einstein [5] and Smoluchowski considers the sample as divided into small volume elements large enough to contain many molecules (i.e., following classical physics), but of linear dimension small compared to the wavelength of light. An incident light wave induces a dipole moment in each volume element, which becomes the source of scattered radiation. Provided that the induced polarization is constant through the medium, the net scattered radiation in all directions but the forward will be zero due to destructive interference, because the wavelets scattered from each subregion differ only by a phase factor that depends on the relative position of the small volumes. Therefore, neglecting small surface effects, it is possible to pair each small volume with another small volume whose scattered field is identical in amplitude but opposite in phase, thus they cancel out [4, 6, 7].

However, in real media there will always be small random fluctuations in the local dielectric constant due to the thermal motion of the atoms and molecules in the sample. Because these fluctuations should be uncorrelated from one volume element to the next, these regions are optically different, and therefore also the amplitudes of the scattered light are uncorrelated. That means that now light is also scattered in other directions than forward due to only partial interference.

The local dielectric constant at a point at position r and time t, $\epsilon(r, t)$, is generally described by the dielectric constant fluctuation tensor $\delta\epsilon(r, t)$. It describes the relation between the local and the average dielectric constant ϵ_0,

$$\epsilon(r, t) = \epsilon_0 I + \delta\epsilon(r, t). \tag{2.46}$$

I is the second-rank unit tensor.

When the incident light is a plane wave with field amplitude E_0, angular frequency ω_i, and incident propagation vector k_i, the incident electric field can be written as

$$E_i(r, t) = n_i E_0 \exp i(k_i \cdot r - \omega_i t) \tag{2.47}$$

with n_i being the unit vector in the direction of the incident field.

At large distance R from the scattering volume, the scattered electric field $E_s(R, t)$ can be obtained from the fact that the Maxwell equations must hold for the total electric field, the incident electric field and as well for the scattered electric field, where the total field is just the sum of the two others:

$$E = E_i + E_s. \tag{2.48}$$

Indeed, the same should be valid for the electric displacement field D and the magnetizing field H. The solution of the Maxwell equations is lengthy and

performed elsewhere [7]. In the end it follows for the component of the scattered electric field $E_s(R, t)$ that

$$E_s(R,t) = \frac{E_0}{4\pi R\epsilon_0} \exp ik_s R \int_V d^3 r$$
$$\times \exp i(\mathbf{q} \cdot \mathbf{r} - \omega_i t [\mathbf{n}_s \cdot [\mathbf{k}_s \times (\mathbf{k}_s \times (\delta\epsilon(\mathbf{r}, t) \cdot \mathbf{n}_i)]], \tag{2.49}$$

where $\mathbf{n}_s$ is the polarization, $\mathbf{k}_s$ is the propagation vector and ω_s is the frequency of the scattered plane wave field that reaches the detector, while V indicates that the integral is over the whole scattering volume. The scattering wave vector $\mathbf{q}$ is defined as the difference between incident and scattered propagation vector,

$$\mathbf{q} = \mathbf{k}_i - \mathbf{k}_s. \tag{2.50}$$

The angle between $\mathbf{k}_i$ and $\mathbf{k}_s$ is called the scattering angle θ (see Fig. 2.2).

Figure 2.2b makes clear that the magnitude of the scattering wave vector q can be computed as

$$q^2 = |\mathbf{q}|^2 = k_i^2 + k_s^2 - 2\mathbf{k}_i \cdot \mathbf{k}_s. \tag{2.51}$$

When—like in most light scattering experiments—$k_i \approx k_s$, i.e., the scattering is quasi-elastic, the cosine rule becomes applicable and Eq. 2.51 becomes

$$q^2 = k_i^2 + k_s^2 - 2\mathbf{k}_i \cdot \mathbf{k}_s = 2k_i^2(1 - \cos\theta) = 4k_i^2 \sin^2\frac{\theta}{2}. \tag{2.52}$$

Or, with $k_s = k_i = 2\pi n/\lambda$, where the length of the incident wave vector is written as function of the refractive index $n (n = \sqrt{\epsilon_0})$ and the incident wave length λ:

$$q = 2k_i \sin\frac{\theta}{2} = \frac{4\pi n}{\lambda}\sin\frac{\theta}{2}. \tag{2.53}$$

This is the Bragg condition.
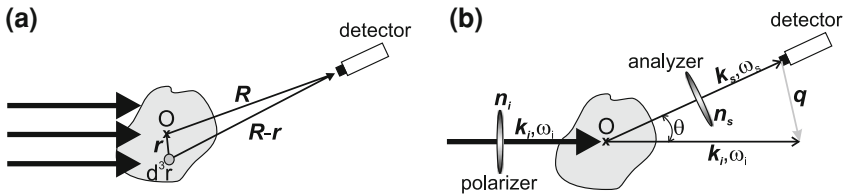
Fig. 2.2 a At the detector, the total radiated field is the sum of all fields radiated from any infinitesimal volume $d^3 r$ at position $\mathbf{r}$ from the center O of the illuminated volume. The detector is at position $\mathbf{R}$. **b** General light scattering setup: incident light of polarization $\mathbf{n}_i$, frequency ω_i, and wave vector $\mathbf{k}_i$ is scattered. Although it is scattered in all directions (not shown for clarity), the figure shows only the light with $\mathbf{n}_s$ and wave vector $\mathbf{k}_s$ that can reach the detector after passing an analyzer. The wave vector $\mathbf{q}$ is shown in gray as $\mathbf{k}_i - \mathbf{k}_s$ (according to [7])

Using the spatial Fourier transform of the dielectric fluctuation

$$\delta\epsilon(\boldsymbol{q}, t) = \int_V d^3 r \exp i\boldsymbol{q}\cdot\boldsymbol{r}\delta\epsilon(\boldsymbol{r}, t), \tag{2.54}$$

Eq. 2.49 can be rewritten as

$$E_s(R, t) = \frac{E_0}{4\pi R\epsilon_0} \exp i(k_s R - \omega_i t)[\boldsymbol{n_s}\cdot[\boldsymbol{k_s} \times \boldsymbol{k_s} \times (\delta\epsilon(\boldsymbol{q}, t)\cdot\boldsymbol{n_i})]]. \tag{2.55}$$

This can be simplified [7]:

$$E_s(R, t) = \frac{-k_s^2 E_0}{4\pi R\epsilon_0} \exp i(k_s R - \omega_i t)\delta\epsilon_{is}(\boldsymbol{q}, t), \tag{2.56}$$

where

$$\delta\epsilon_{is}(\boldsymbol{q}, t) \equiv \boldsymbol{n_s}\cdot\delta\epsilon(\boldsymbol{q}, t)\cdot\boldsymbol{n_i} \tag{2.57}$$

is the component of the dielectric constant fluctuation tensor along the initial and final polarization direction.

The time-correlated function of E_s can then be written as

$$\langle E_s^*(R, 0)E_s(R, t)\rangle = \frac{k_s^4 |E_0|^2}{16\pi^2 R^2 \epsilon_0^2} \langle\delta\epsilon_{is}(\boldsymbol{q}, t)\rangle \exp(-i\omega_i t). \tag{2.58}$$

Then, the spectral density

$$I_E(\omega) = \frac{1}{2\pi} \int_{-\infty}^{+\infty} d\tau\langle E^*(t)E(t + \tau)\rangle \exp(-i\omega\tau) \tag{2.59}$$

of light reaching the detector with $\boldsymbol{n_s}$, $\boldsymbol{k_s}$, and ω_s can be computed as

$$I_{is}(\boldsymbol{q}, \omega_s, R) = \left(\frac{I_0 k_s^4}{16\pi^2 R^2 \epsilon_0^2}\right) \frac{1}{2\pi} \int_{-\infty}^{+\infty} dt\langle\delta\epsilon_{is}(\boldsymbol{q}, 0)\delta\epsilon_{is}(\boldsymbol{q}, t)\rangle \exp(i(\omega)t) \tag{2.60}$$

with $I_0 \equiv |E_0|^2$ and

$$\omega \equiv \omega_i - \omega_s. \tag{2.61}$$

The latter means that the spectral density (the intensity measured by the detector) depends only on the difference between the incident and the scattered frequency. Furthermore from Eq. 2.60 one can learn that $I_{is} \propto k_s^4$ (i.e., $I_{is} \propto \lambda^{-4}$) and $I_{is} \propto R^{-2}$. The λ^{-4} dependence means that electromagnetic radiation with short wavelengths is scattered more than that with longer wavelength, as, e.g., apparent in the blue color of the sky. The R^{-2} dependence is expected, because it just expresses the attenuation of a spherical wave.

For a given experiment, the coefficient in Eq. 2.60 becomes a constant, and the scattering intensity is then only affected by the spectral density of the dielectric constant fluctuations, i.e., the integral

$$I_{is}(\boldsymbol{q}, \omega) \propto \int_{-\infty}^{+\infty} dt \big\langle \delta\epsilon_{is}^*(\boldsymbol{q}, 0)\delta\epsilon_{is}(\boldsymbol{q}, t) \big\rangle. \tag{2.62}$$

The integral of Eq. 2.62 over frequency, the integrated intensity at all frequencies, provides information about the $\boldsymbol{q}$-dependent mean-square fluctuations ϵ:

$$I_{is}(\boldsymbol{q}) = \Big\langle |\delta\epsilon_{is}(\boldsymbol{q})|^2 \Big\rangle. \tag{2.63}$$

Harking back on the definition of the scattering wave vector $\boldsymbol{q}$ (Eq. 2.50) and the frequency shift ω (Eq. 2.61), the scattering event can be considered in terms of energy and momentum conservation. Most generally, during a scattering process, the scattered photon sustains an energy change from $\hbar\omega_i$ to $\hbar\omega_s$ and a momentum change from $\hbar k_i$ to $\hbar k_s$. This must be related to the creation or annihilation of an excitation in the scattering medium. It is:

$$\hbar\omega = \hbar\omega_s - \hbar\omega_i \tag{2.64}$$

$$\hbar\boldsymbol{k} = \hbar\boldsymbol{k_s} - \hbar\boldsymbol{k_i}. \tag{2.65}$$

Note that in these equations the energy and momentum of the excitation can have both positive and negative sign.

2.3 Brillouin Light Scattering

Brillouin light scattering (BLS) is the inelastic scattering of monochromatic laser light by phonons in the GHz frequency range. The required high resolution is obtained by the use of multipass tandem Fabry–Pérot interferometers. In BLS spectroscopy of transparent samples, the desired dispersion relations are obtained by recording the phonon frequencies as a function of the scattering wave vector **q**, which varies with the scattering angle. However, in samples exhibiting strong multiple light scattering, as for the dry colloidal crystals (opals), **q** is ill-defined and hence **q**-dependent acoustic-like modes become inaccessible. Though, localized in space, i.e., **q**-independent modes can be recorded in the BLS spectrum as it was demonstrated for sub-micron colloidal silica [8] and polymer crystals [9]. These **q**-independent frequencies have been identified as the resonance modes of the individual colloidal particles, i.e., BLS can record numerous thermally excited elastic resonances in one measurement (Chap. 4). These eigenfrequencies are uniquely defined by the geometrical and elastic characteristics of the particles. Based on these data, the elastic properties of the materials can be calculated at the nanoscale. Thus the combination of **q**-independent BLS spectroscopy of multiply

light scattering (opaque) samples and the dispersion relations from the **q**-dependent BLS spectroscopy on transparent samples is a powerful methodology to investigate the elastic behavior of nanostructured materials.

This section will introduce the basic principles of BLS following a simple approach. Further important results obtained by thermodynamical considerations will be introduced very briefly. Then a description of the BLS setup with selective attention on the main principles of the tandem Fabry–Pérot interferometer is given.

2.3.1 BLS Basics

The main principle of BLS is the scattering of photons on sound waves and the constructive interference of the multiply reflected light beam as sketched in Fig. 2.3. A plane elastic wave creates a periodic change of density and hence of the local dielectric constant in a medium, symbolized by the black/white layers. The typical velocity of an acoustic wave is between 10^3 and $10^4 \, \mathrm{ms}^{-1}$, while the velocity of the probing light c is $\approx 3 \times 10^8 \, \mathrm{ms}^{-1}$. Because of this great discrepancy the dielectric inhomogeneities can be regarded as a quasi-static (i.e., 'frozen') lattice on which the photons of the probing light are scattered. Thus, it is justified to treat the medium as a periodic multilayer stack with periodicity Λ, the wavelength of the phonon, as shown in Fig. 2.3. The probing laser light is multiply reflected (under the scattering angle θ) on these layers and the reflected light interferes on the detector, whose distant to the sample R is much larger than the periodicity of the scattering planes ($R \gg \Lambda$). The reflected intensity reaches its maximum when the interference is constructive, i.e.,

$$2n\Lambda \sin\frac{\theta}{2} = \lambda \tag{2.66}$$

with refractive index n and wavelength of light λ.

Fig. 2.3 BLS scattering process: the probing light beam is multiply reflected on the planes of a quasi-static periodic multilayer stack of modulated local dielectric constant with periodicity Λ. Only reflected beams that interfere constructively account for the scattering intensity
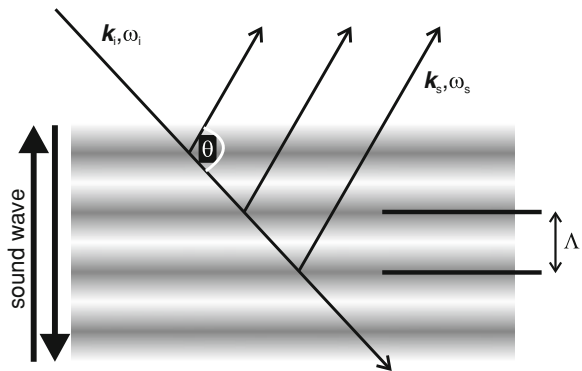
Insertion of Eq. 2.66 in the Bragg condition (Eq. 2.53) leads to

$$\frac{2\pi}{\Lambda} = \frac{4\pi n}{\lambda} \sin\frac{\theta}{2} \tag{2.67}$$

and

$$q = \frac{2\pi}{\Lambda}. \tag{2.68}$$

That is to say the scattering wave vector $\boldsymbol{q}$ is equivalent to the wave vector $\boldsymbol{k}$ of the sound wave ($k = 2\pi/\Lambda$), viz. by changing θ, $\boldsymbol{q}$ can be chosen, too, and at every q the corresponding sound waves are probed selectively. The identity $\boldsymbol{q} = \boldsymbol{k}$ shows that the momentum conservation (cf. Eq. 2.64) during the scattering process is realized by a momentum transfer between the sound wave and the photon. From this point of view it is clear that the scattered light changes its angular frequency from ω_i to ω_s by inelastic interaction, in which a phonon, the acoustic quantum, can be either created (Stokes process) or annihilated (anti-Stokes process), depending on the direction of motion of the acoustic wave. In terms of energy conservation considerations (Eq. 2.65) it is obvious that the exchanged energy $\hbar\omega$ comes from the angular frequency of the phonon, $\omega_{\mathrm{phonon}} = |\omega| = \omega_s - \omega_i$, which is related to the phonon wavelength and the velocity c of the acoustic wave by

$$\omega_{\mathrm{phonon}} = \omega = \frac{2\pi c}{\Lambda}. \tag{2.69}$$

Therefore the frequency $f = \dfrac{\omega}{2\pi}$ undergoes a Doppler shift:

$$f_s = f_i \pm \frac{cq}{2\pi} = f_i \pm \frac{c}{2\pi}\frac{4\pi n}{\lambda}\sin\frac{\theta}{2}, \tag{2.70}$$

using the definition of q given in Eq. 2.53. Here, the minus corresponds to a motion of the acoustic wave away from the detector leading to a frequency decrease (or phonon creation; Stokes), and the plus corresponds to a propagation direction of the acoustic waves towards the detector leading to an increasing photon frequency (or phonon annihilation; anti-Stokes). Obviously, it is

$$\omega = \omega_s - \omega_i = \pm cq. \tag{2.71}$$

Therefore the BLS spectrum consists of doublets centered at the elastic frequency with frequencies $f = \pm cq/2\pi$ (frequency shifts).

Equations 2.64 and 2.65 can now be rewritten for the Brillouin scattering process as follows:

$$\hbar\omega_s - \hbar\omega_i = \pm\hbar\omega \tag{2.72}$$

$$\hbar\boldsymbol{k}_s - \hbar\boldsymbol{k}_i = \pm\hbar\boldsymbol{q}. \tag{2.73}$$

Note that in these equations momentum and energy (frequency) of the acoustic wave are positively defined and plus- and minus-signs correspond again to anti-Stokes and Stokes process, respectively.

So far, this easy approach explains satisfactorily the appearance of the doublet as well as the position of the frequency shifts. However, when performing BLS experiments a central line always appears that is not explained by the above considerations. Also the intensity of the signals can not be predicted. To elucidate these features of a BLS spectra it is necessary to take some ideas from thermodynamics into account.

The total scattering intensity of a Brillouin spectrum was first derived by Einstein in 1910 [5, 6]. He started with considering ϵ as a function of density and temperature $\epsilon = \epsilon(\varrho, T)$. For ϱ and T are statistically independent, one can write the total differential

$$d\epsilon = \left(\frac{\partial \epsilon}{\partial \varrho}\right)_T d\varrho + \left(\frac{\partial \epsilon}{\partial T}\right)_\varrho dT. \tag{2.74}$$

Then

$$\left\langle (d\epsilon)^2 \right\rangle = \left(\frac{\partial \epsilon}{\partial \varrho}\right)_T^2 \left\langle (d\varrho)^2 \right\rangle + \left(\frac{\partial \epsilon}{\partial T}\right)_\varrho^2 \left\langle (dT)^2 \right\rangle. \tag{2.75}$$

Using the assumption

$$\left(\frac{\partial \epsilon}{\partial \varrho}\right)_T \gg \left(\frac{\partial \epsilon}{\partial T}\right)_\varrho \tag{2.76}$$

and

$$\frac{\left\langle (d\varrho)^2 \right\rangle}{\varrho^2} = \frac{k_B T \beta_T}{v} \tag{2.77}$$

for the mean-square fluctuation in density in the volume element v, where k_B is Boltzmann's constant and β_T is the isothermal compressibility, Eq. 2.75 becomes

$$\left\langle (d\epsilon)^2 \right\rangle \approx \left(\frac{\partial \epsilon}{\partial \varrho}\right)_T^2 \left\langle (d\varrho)^2 \right\rangle = \left(\varrho \frac{\partial \epsilon}{\partial \varrho}\right)_T^2 \frac{k_B T \beta_T}{v}. \tag{2.78}$$

Comparison with Eq. 2.63 shows the main result of these calculations,

$$I \propto \beta_T, \tag{2.79}$$

i.e., the total scattering intensity depends on the isothermal compressibility. Without going into details, the full vectorial expression for $I(\boldsymbol{q})$ is given by [7]

$$I_{is}(\boldsymbol{q}) = (\boldsymbol{n_i} \cdot \boldsymbol{n_s})^2 \left(\frac{\partial \epsilon}{\partial \varrho}\right)_T^2 V \varrho^2 k_B T \beta_T \tag{2.80}$$

with scattering volume V. If $V(\theta) \approx$ const, which may be valid depending on the experimental details, the total scattering intensity is also independent from the scattering angle.

Although Eq. 2.80 gives the total scattering intensity, experiments showed that only a part of the intensity belongs to the Brillouin doublets while the rest makes for a central line. These findings could be explained by Landau and Placzek regarding $\epsilon(S, p)$ as function of entropy S and pressure p [1]. In analogy to Eq. 2.75 one can write

$$\left\langle (d\epsilon)^2 \right\rangle = \left(\frac{\partial \epsilon}{\partial S} \right)_p^2 \left\langle (dS)^2 \right\rangle + \left(\frac{\partial \epsilon}{\partial p} \right)_S^2 \left\langle (dp)^2 \right\rangle \tag{2.81}$$

because fluctuations in S and p are independent, too.

The first term, also called the Rayleigh term, represents local entropy fluctuations, which do not propagate in normal liquids and are the source of the unshifted component of the scattered light with intensity I_C. The other term, the Brillouin term, represents the isoentropic pressure fluctuations, ergo, sound waves that contribute to the Brillouin doublet. With

$$\left\langle (dp)^2 \right\rangle = \frac{k_B T}{v \beta_S}, \tag{2.82}$$

where β_S is the adiabatic compressibility, and by writing

$$\left(\frac{\partial \epsilon}{\partial p} \right)_S = \left(\frac{\partial \epsilon}{\partial \varrho} \right)_S \left(\frac{\partial \varrho}{\partial p} \right)_S = \left(\frac{\partial \epsilon}{\partial \varrho} \right)_S \varrho \beta_S \tag{2.83}$$

the Brillouin term can be transformed into

$$\left(\frac{\partial \epsilon}{\partial p} \right)_S \left\langle (dp)^2 \right\rangle = \left(\frac{\partial \epsilon}{\partial \varrho} \right)_S^2 \varrho^2 \beta_S^2 \frac{k_B T}{v \beta_S} = \left(\varrho \frac{\partial \epsilon}{\partial \varrho} \right)_S^2 \frac{k_B T \beta_S}{v}. \tag{2.84}$$

It becomes clear that the intensity of the Brillouin doublet $2I_B$ depends on the adiabatic compressibility β_S.

After further simplifications it can be shown that the ratio between total scattering intensity $(I_C + 2I_B)$ and the intensity of the Brillouin doublet is simply given by the ratio of isothermal and adiabatic compressibility or of the specific heats at constant pressure or volume [1, 6, 7]:

$$\frac{I_C + 2I_B}{2I_B} = \frac{\beta_T}{\beta_S} = \frac{C_p}{C_V}. \tag{2.85}$$

In the form

$$\frac{I_C}{2I_B} = \frac{\beta_T - \beta_S}{\beta_S} = \frac{C_p - C_V}{C_V} = \gamma - 1 \tag{2.86}$$

it is known as the Landau–Placzek equation.

2.3.2 BLS Instrumentation

It was already pointed out that the relative shift of the photon frequency in BLS spectroscopy ($\sim 10^8$ to 10^{11} Hz) is quite subtle compared to the initial frequency of the probing light (10^{14} Hz) or to the resolution obtained by Raman spectroscopy, where frequency shifts in the order of 10^{13} Hz are measured frequently by diffraction grating spectrometers. In order to achieve such high resolution, Fabry–Pérot interferometers (FPs) are used in BLS. In combination with an highly monochromatic laser light source a single FP or, even better, a design composed of two FPs with multiple light pass can give excellent results. Here the FP principle is elucidated and the construction details of the used tandem FP as well as the general features of the whole BLS setup are illuminated.

In principle, a single FP is not much more than an etalon as it is used in laser resonant cavities. The FP consists of two plane mirrors with reflectivity R mounted accurately parallel to one another. The spacing between the mirrors is given by d and can be varied by moving one of the mirrors. When the laser light enters the etalon through the first mirror, which is usually a plane glass plate with a thin layer of metal on the inner side, it is reflected numerously between the two mirrors. However, the light with intensity I_I is already reflected when it enters the etalon, so that we have only the intensity $I_0 = I_I(1 - R)$ inside the FP before the first internal reflection. During the reflections within the FP, the intensity decreases after x reflections to

$$I_x = I_0 R^x = I_I(1 - R)R^x, \tag{2.87}$$

because every time a part of the light is also transmitted; a typical value for BLS experiments is $R \approx 0.93$. Note that Eq. 2.87 is not fully true as it does not take into account the dissipation of energy, which is usually considered by the absorptance A, i.e., $R + T + A = 1$, with transmittance T. Anyhow, it implies that with increasing reflectivity the number of reflections inside the FP increases rapidly, and this is important for the working principle of the system. When the light is reflected many times between the mirrors, the reflected beams interfere. Only light that fulfills the equation

$$m\lambda = 2n_{\text{FP}}d \cos \theta_{\text{FP}}, \tag{2.88}$$

with m being an integer and n_{FP} being the refractive index inside the FP, and θ_{FP} being the angle between the light in the FP and the normal to the mirrors, is transmitted losslessly due to constructive interference. Thus usually the interferometry is performed by moving one of the mirrors, there is just air between the mirrors. (The other possibility would be to vary n during a measurement.) With normal incidence ($\cos 0 = 1$) and $n = 1$ we can therefore simplify to

$$\lambda = \frac{2d}{m}. \tag{2.89}$$

That means that only light with wavelength $2d/m$ is transmitted, and the transmitted λ can be easily scanned when scanning different ds by moving a mirror,

e.g., by a piezo transducer. The separation between two adjacent transmission maxima for a given d is called the free spectral range (FSR$_\lambda = \Delta\lambda$). Differentiating Eq. 2.89 leads to

$$\frac{\Delta\lambda}{\lambda} = \frac{\Delta m}{m} \tag{2.90}$$

with initial wavelength λ. For $m \pm 1$ it follows in the described setup (normal incidence, $n_{FP} = 1$)

$$\text{FSR}_\lambda = \frac{\lambda^2}{2d}, \tag{2.91}$$

or in the frequency domain

$$\text{FSR} = \frac{v}{2d}, \tag{2.92}$$

with v being the velocity of light in vacuum.

The linewidth of the transmitted line depends strongly on R. As denoted above, the more often the beam is reflected before it transmits the second beam of the FP (or the first, but this light is uninteresting for the further analysis) the more often it can interfere with itself. Therefore the destructive interference will be enforced for wavelengths not satisfying Eq. 2.89 with increasing reflectivity and the function $I(\lambda)$ becomes more narrow.

Indeed, the phase difference δ_p between each succeeding reflection is

$$\delta_p = \frac{2\pi}{\lambda} 2d. \tag{2.93}$$

The transmission function of the etalon $T(\delta_p)$ is found to be (http://en.wikipedia.org/wiki/Fabry_Perot, April 2009)

$$T(\delta_p) = \frac{(1-R)^2}{1 + R^2 - 2R\cos\delta_p} = \frac{1}{1 + c_F \sin^2\frac{\delta_p}{2}}, \tag{2.94}$$

where c_F is the so-called coefficient of finesse F:

$$c_F \equiv \frac{4R}{(1-R)^2}. \tag{2.95}$$

F is defined as the ratio between FSR$_\lambda$ and the full width at half maximum (FWHM$_\lambda$) of a transmission peak in the $T(\lambda)$-function, i.e., F gives the relative separation between nearest transmission peaks (cf. Fig. 2.4) and is also the most important parameter for the practical resolution of a spectrometer. As it is approximately

Fig. 2.4 High and low
finesse, FWHM$_\lambda$ at
fixed FSR$_\lambda$
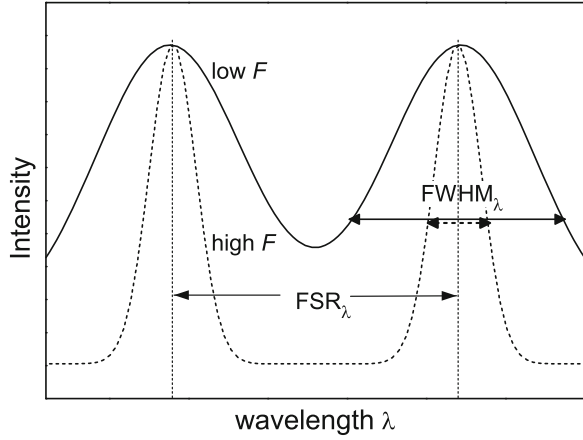
$$\text{FWHM}_\lambda \approx \frac{4}{\sqrt{c_F}}, \tag{2.96}$$

the finesse is found to be

$$F = \frac{\text{FSR}_\lambda}{\text{FWHM}_\lambda} \approx \frac{\pi\sqrt{c_F}}{2} = \frac{\pi\sqrt{R}}{1-R}. \tag{2.97}$$

However, in real experiments the 'practical finesse' depends not only on the reflectivity of the mirrors but also, e.g., on the mirror flatness. In general, a high F is intended, but by practical limitations it cannot be made much greater than about 100 [10].

Single-pass FPs have been used to realized the first measurements of traveling acoustic waves in solids and liquids. However, it turned out quite early that the contrast was too low to resolve weaker signals and also the interference between neighboring orders could create easily very complicated spectra. Both problems were solved by John Sandercock when he introduced his multi-pass tandem Fabry–Pérot interferometer (multi-pass modes are also possible in single FPs).

The idea behind is quite simple: two FPs with slightly different *FSR* are connected in series (tandem). An intelligent use of additional mirrors assures that the light passes each FP several times (multi-pass). In the tandem operation, both FPs must transmit the same wavelength simultaneously by an appropriate scanning technique. Due to the differing *FSR*s of both individual FPs, always one of the FPs blocks the neighboring interferences. Let us assume FP1 to have a free spectral range FSR$_{\lambda 1}$ and FP2 FSR$_{\lambda 2}$. Then only wavelengths are transmitted that simultaneously satisfy

$$\lambda_{\text{trans}} = 2pd_1 \text{ and } \lambda_{\text{trans}} = 2qd_2, \tag{2.98}$$

where d_1 and d_2 are the mirror distances in FP1 and FP2 and p and q are integers. The effect of the tandem operation is sketched in Fig. 2.5b. The next order of light
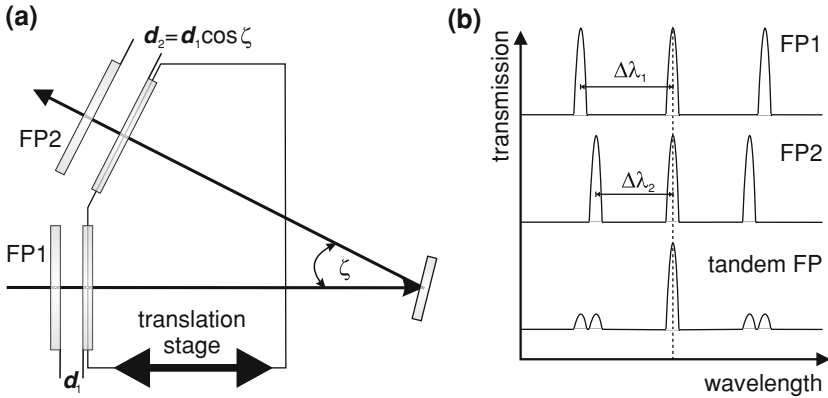
Fig. 2.5 **a** Basic mechanism of a Sandercock multipass tandem Fabry–Pérot interferometer. The light passes FP1 and then FP2. Two mirrors (one of FP1 and one of FP2) are moved simultaneously on a piezoelectric translation stage. The angle ζ of the light path between the two FPs is chosen in that way that the ratio between d_1 and d_2 is constant. **b** Effect of the multi-pass through two FPs: the neighboring orders (viewed from the harmonized central signals) that can pass each single FP are suppressed. Only the common multiples of $\Delta\lambda_1$ and $\Delta\lambda_2$ will be transmitted gainlessly

transmitted through FP1 (i.e., $\Delta p = 1$) is nearly completely suppressed by FP2 and vice versa, depending on the reflectivity of the mirrors. In our case the transmittance of wrong wavelengths is about 10^{-3}. According to that, the total *FSR* of the tandem interferometer is the distance between the common multiples of $\Delta\lambda_1$ and $\Delta\lambda_2$. Therefore, with tandem FPIs much higher finesses can be achieved.

Although the principle idea is not complicated at all, the technical realization was problematic. Both FPs have to be scanned synchronously, and from Eqs. 2.89 and 2.98 it is clear that the ratio between the mirror distances in both FPs must be constant. With other words

$$\frac{\Delta d_1}{\Delta d_2} = \frac{d_1}{d_2}. \tag{2.99}$$

Indeed, this condition was hard to satisfy as the total scanning distance is usually below 1 µm and the scan is repeated many times during one measurement, so that even very small asymmetries in the nanometer-range would disable the experiment.

This problem was solved in 1987 by a new, elegant design, presented in Fig. 2.5a [11]. The two FPs used in Sandercock's 'parallelogram geometry' consist of one fixed mirror and one movable mirror, each. The two movable mirrors are placed on a shared panel, the translation stage, which is the part of the setup moved during the scan. Thus, both FPs change the mirror distance always at the same time. The FPs are mounted that the two mirrors of each would touch at the same time if the translation stage would be moved to the very left. In order to satisfy Eq. 2.99 the relative orientation of the two FPs is chosen that way that the

angle ζ between FP1 and FP2 is fixed and the mirror distances have then to be adjusted in a way that

$$d_2 = d_1 \cos \zeta. \tag{2.100}$$

A movement of the translation stage to the right shifts the spacings between the mirrors simultaneously by Δd_1 and $\Delta d_1 \cos \zeta$, i.e., the ratio keeps constant.

In my experiments, a six-pass tandem Fabry–Pérot interferometer was used. The path of the light inside the FP as well as the other details of the applied BLS setup are sketched in Fig. 2.6. The sample is mounted in the center of a goniometer (Huber) in a custom-made sample holder with or without oven. A solid state pumped frequency-doubled Nd:YAG laser (coherence; 150 mW at 532 nm) is fixed on the goniometer and can be rotated so that scattering angles between 0° and $\sim 160°$ can be chosen either in transmission or reflection geometry. In difference to pure BLS backscattering techniques, i.e., $\theta = 180°$, this technique has the advantage that not only the components of q but the whole wave vector is changed according to Eq. 2.53.

Before the light reaches the sample, it passes a Glan polarizer (extinction ratio 10^{-5}) with vertical polarization (V), i.e., perpendicular to the scattering plane, to ensure fully polarized incident light. Behind the sample the light scattered in the direction of the detector is collected by an aperture and focused into the entrance pinhole of the tandem Fabry–Pérot interferometer (JRS Scientific Instruments) by some lenses. Before entering the FP, a Glan–Thompson analyzer (extinction ratio 10^{-8}) is passed that selects either vertically (V), i.e., perpendicular to the scattering plane, or horizontally, i.e., parallel to the scattering plane, polarized light (or, of course, everything in between). After passing the FP the transmitted light is detected by an avalanche photo diode (APD) and processed by an multi-channel analyzer with 1,024 channels. The further processing is performed by a computer software.

The stability of the alignment is greatly enhanced by the use of a reference beam. Therefore, a small amount of the laser light is diverted via the reflection

Fig. 2.6 BLS setup with six-pass tandem Fabry–Perot interferometer. Electronic stabilization over days to weeks is achieved by permanent compensation using a diverted part of the unscattered light as reference beam. The goniometer allows to record dispersion relations with continuous **q**-range. For the eigenmode spectra the scattering angle is not relevant [12]
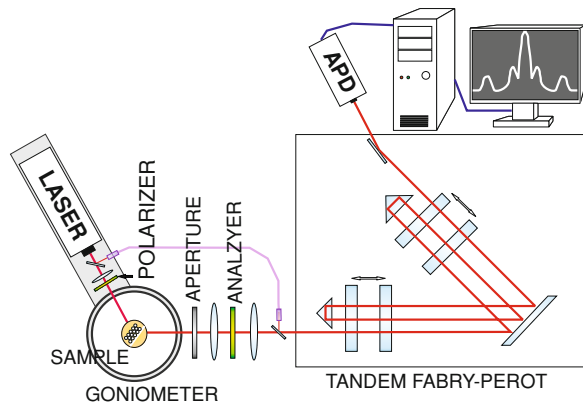
(5%) of a parallel plate on a beam splitter and an optical fiber from the incident laser beam and introduced as a reference beam that gives the central line via an optical fiber. Therefore, a mechanical shutter is used, which switches periodically the entrance to the FP between reference beam and scattered light and excludes the central elastic line. In order to avoid mechanical disruptions the whole setup is placed on an optical table with active vibration damping.

In some experiments dealing with temperature-dependent effects, e.g., glass transition experiments (Sect. 4.3.1 in Chap. 4) or measurements on kinetically stable organic glasses (Chap. 6), an oven is used in order to control the temperature of the sample in the range between ca. 10 and 200 °C. The oven is a metal cylinder with filament and coolant tubes in the wall [13]. A small slit at the hight of the laser and a cylindrical quartz glass insert in order to avoid heat transfer through the slit allow the light to reach the sample and the detector afterwards. The temperature is controlled electronically (built in-house) by two Pt-100 temperature sensors inside the wall and inside the heat chamber, close to the sample. The temperature can be stabilized within better than ± 0.2 K in the given range.

Most experiments in this thesis deal with samples on a plane substrate, i.e., 'films'. When performing the BLS experiment on such samples, there are in principle two different scattering geometries, the transmission and the reflection geometry. In transmission geometry the light scattered on the other side of the film than that of the incident laser beam is investigated, while in reflection geometry the light scattered on the side of the incident beam is regarded.

The two geometries are sketched in Fig. 2.7 and a full geometrical derivation is given in Appendix.

Fig. 2.7 Principle BLS scattering geometries for a film sample (view atop the scattering plane). **a** Transmission geometry, **b** reflection geometry. On the right side the vector decomposition for the wave vector **q** in its components perpendicular ($\mathbf{q}_{perp}$) and parallel to the film plane ($\mathbf{q}_{para}$)
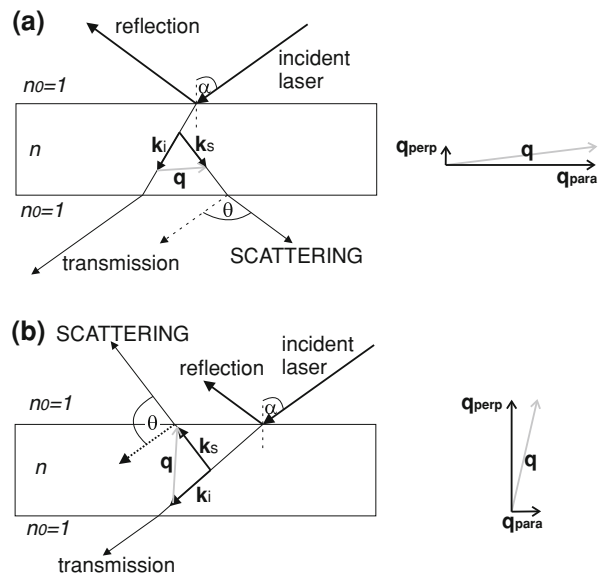
In the transmission case, it is found that the magnitude of the scattering wave vector becomes

$$q = \frac{4\pi n}{\lambda} \sin\left[\frac{1}{2}\left(\sin^{-1}\left(\frac{1}{n}\sin(\theta - \alpha)\right) + \sin^{-1}\left(\frac{1}{n}\sin\alpha\right)\right)\right] \qquad (2.101)$$

with the angles α and θ given in Fig. 2.7a. It is shown in the appendix that the length of the component of the scattering wave vector parallel to the film, q_{para}, is

$$q_{\text{para}} = \frac{2\pi}{\lambda}(\sin\alpha + \sin(\theta - \alpha)). \qquad (2.102)$$

Obviously, in this equation the refractive index n of the sample is eliminated.

A special transmission geometry in which $\boldsymbol{q} = \boldsymbol{q}_{\text{para}}$ exists for $\theta = 2\alpha$. In this case q is given simply by

$$q = q_{\text{para}} = \frac{4\pi}{\lambda}\sin\frac{\theta}{2} \quad (\text{for} \quad \theta = 2\alpha). \qquad (2.103)$$

To use this special geometry is advantageous in several ways, indeed nearly all the experiments in this thesis are performed using it. First of all, it facilitates the calculation of q, as the refractive index of the sample has not to be taken into account. Although n of most 'standard materials' (e.g., typical polymers like polystyrene) is well-known, the exact determination of n for unknown materials or, even more, for composite materials, as they are widely used in this thesis, may become complicated and time consuming. The second great benefit of this geometry is that in this case the direction of $\boldsymbol{q}$ is well defined parallel to the film. When discussing colloidal crystals [14] it is important to know which crystallographic direction is probed by the BLS experiment.

In the reflection geometry the general expression for q as a function of n, θ, and α becomes

$$q = \frac{4\pi n}{\lambda} \cos\left[\frac{1}{2}\left(\sin^{-1}\left(\frac{1}{n}\sin\alpha\right) + \sin^{-1}\left(\frac{1}{n}\sin(\theta + \alpha)\right)\right)\right]. \qquad (2.104)$$

Also for the reflection case there is a special scattering geometry. If $\alpha = \frac{180° - \theta}{2}$ the scattering wave vector is identical to its component perpendicular to the film, i.e., $\boldsymbol{q} = \boldsymbol{q}_{\text{perp}}$ in Fig. 2.7b.

In a cylindrical sample, e.g., a liquid in a NMR-tube, $\boldsymbol{q}$ has simply the magnitude

$$q_{\text{cylinder}} = \frac{4\pi n}{\lambda}\sin\frac{\theta}{2}. \qquad (2.105)$$

2.3.3 Vibrational Modes of Individual Particles

In the foregone section it was pointed out that the result of a BLS experiment is usually the plot of longitudinal or transverse [or mixed, especially in thin films, e.g., the so-called Lamb waves (http://en.wikipedia.org/wiki/Lamb_wave, May 2009)] sound waves as a function of the scattering wave vector q, while the frequencies $f(q)$ are given as a Doppler shift of the probing laser light around its elastic line. The phase sound velocities are given by the slope of the $f(q)$-diagram. Thus, in the case of a nonlinear function $f(q)$, i.e., if the acoustic mode is dispersive, the result of the BLS experiment is the dispersion relation in the investigated q-range.

However, the appearance of a dispersion relation is only meaningful if it is possible to determine q. If strong multiple scattering occurs in a sample, q becomes ill-defined. In such samples $f(q)$ is no longer accessible. Anyhow, now the inelastic scattering from localized modes, i.e., the vibrational resonance modes, can lead to incoherent BLS in analogy to the Raman scattering.

Indeed, in BLS experiments such samples show a spectrum where scattering at all possible qs between zero degree incident and backscattering case contributes to the final result, independent from the experimental scattering angle θ. Furthermore, also the polarization information is lost.

Nevertheless, the Brillouin spectrum of multiple scattering samples with well defined shape still gives useful information, which are not accessible by other techniques. In Chap. 4 of this thesis, several experiments are discussed dealing with the detection of vibrational resonance modes of spherical colloidal samples. BLS spectra of such samples deliver many useful information about the individual colloids and, in case of hybrid materials, about the mechanical properties of the components, too. This section will give a short introduction into the mathematical description of the vibrations in spheres, their theoretical calculation, and their detection by BLS.

Under stress-free boundary conditions, the vibrational modes are usually called eigenmodes. The eigenmodes for free homogeneous elastic spheres have been derived by Lamb in the nineteenth century [15]. The modes can be classified as torsional and spheroidal ones, both labeled by the indices n, l, and m, which describe the radial (n) and the angular (l, m) dependence of the displacement (cf. Sect. 2.1.3). The torsional modes are fully tangential, i.e., they involve only shear motions and do not cause changes in the sphere volume—they do not contribute to the BLS intensity. The spheroidal modes involve usually both shear and stretching motions, and they can be fully specified by two indices in analogy to the atomic orbitals as the n-th order radial solution ($n = 1, 2, 3,...$) for angular momentum 'quantum number' l ($l = 0, 1, 2,...$) [4, 12, 16]. Only spheroidal modes with $l = 0$ have purely radial displacement (breathing modes) [17].

By solving the wave equation for elastic and isotropic media (Eq. 2.37), Lamb found the frequencies of the eigenmodes (n, l) to be (in a very general expression):

$$f(n, l) = \left(x(n, l) \sqrt{\frac{R(c_l, c_t)}{\varrho}} \right) \Big/ d, \qquad (2.106)$$

with $x(n, l)$ being a constant for each individual mode, $R(c_l, c_t)$ being the rigidity, and d being the diameter of the sphere. The rigidity is a function of the longitudinal and transverse sound velocities and has the dimension of pressure, thus it is simply a modulus. Indeed, e.g., for the (1,2)-mode, R is identical with the shear modulus $\mu (= C_{44})$.

The experiments discussed in Chap. 4 are all related to the vibrational modes of colloidal spheres in air. Because of the large density (and elastic) mismatch between air and the colloids, the boundary-conditions are quasi that of a stress-free, undamped vibration, thus these modes are practically real eigenmodes and the values calculated by Lamb's theory are a good approximation. However, in the more general case of a elastic vibrator embedded in an elastic matrix, some coupling should occur between the eigenmodes and the propagating acoustic waves in the matrix. The amount of coupling depends on the elastic mismatch between spheres and matrix. While the limit case of large mismatch corresponds to the free eigenmodes, where the elastic energy is totally localized in the spheres, the other limit case is a zero-mismatch, which means that all energy is coupled between sphere and matrix and an elastic wave can travel the system like a homogeneous medium.

To calculate the distinct vibrational modes of elastic spheres with radius r_s and density ϱ_s in an elastic matrix with density ϱ_m, one has to introduce boundary conditions. At the surface of the sphere, the displacement $\boldsymbol{u}$ has to be the same inside and outside the sphere [4, 18]:

$$\boldsymbol{u}^i\big|_{r=r_s} = \boldsymbol{u}^m\big|_{r=r_s}. \qquad (2.107)$$

The same must be fulfilled for the surface traction $\tau (\tau = \sigma(\boldsymbol{r}) \cdot \hat{\boldsymbol{r}}$, with stress tensor σ and outgoing unit vector normal to the sphere surface $\hat{\boldsymbol{r}}$) :

$$\boldsymbol{\tau}^i\big|_{r=r_s} = \boldsymbol{\tau}^m\big|_{r=r_s}. \qquad (2.108)$$

The field can be written as a linear sum of spherical waves as discussed in Sect. 2.1.3. The field inside the spheres becomes

$$\boldsymbol{u}^i(\boldsymbol{r}) = \sum_{lm} a_{lm}^L \boldsymbol{l}_{lm}(R, k_l^i) + a_{lm}^M \boldsymbol{m}_{lm}(R, k_t^i) + a_{lm}^N \boldsymbol{n}_{lm}(R, k_t^i) \qquad (2.109)$$

with the coefficients a_{lm}^L, a_{lm}^M and a_{lm}^N. In the same way we can write for the field in the matrix

$$\boldsymbol{u}^m(\boldsymbol{r}) = \sum_{lm} b_{lm}^L \boldsymbol{l}_{lm}^m(R, k_l) + b_{lm}^M \boldsymbol{m}_{lm}(R, k_t^m) + b_{lm}^N \boldsymbol{n}_{lm}(R, k_t^m) \qquad (2.110)$$

with the coefficients b_{lm}^L, b_{lm}^M and b_{lm}^N. With Eqs. 2.43–2.45 one can write

$$\boldsymbol{u}(\boldsymbol{r}) = \sum_{lm} x_{lm}^L \frac{1}{k_l} \nabla [R_l(k_l r) Y_{lm}(\hat{\boldsymbol{r}})] + x_{lm}^M \nabla \times [\boldsymbol{r} R_l(k_t r) Y_{lm}(\hat{\boldsymbol{r}})]$$

$$+ x_{lm}^N \frac{1}{k_t} \nabla \times \nabla \times [\boldsymbol{r} R_l(k_t r) Y_{lm}(\hat{\boldsymbol{r}})], \tag{2.111}$$

where the x replace either the coefficients a inside or b outside the spheres and k_l and k_t are the longitudinal wavenumbers ($k = \omega/c$) inside (k^i) or outside (k^m) the sphere, respectively.

With Eq. 2.111 it becomes clear that Eqs. 2.107 and 2.108 are equivalent to three scalar equations, each, and the boundary conditions can be expressed as a system of six homogeneous equations with an infinite numbers of unknowns. Due to the orthonormality over the spherical surface of the Legendre functions Y_{lm}, it is possible to decompose each of these equations into l equations, but independent from m. That is also the coefficients a and b depend only on l, leading to a system of six equations with six unknowns for each l. It can be broken into two smaller systems, considering the orthogonality of $\boldsymbol{m}_{lm}$ to $\boldsymbol{n}_{lm}$ and $\boldsymbol{l}_{lm}$, which contain two equations involving the coefficients a_l^M and b_l^M and four equations containing the coefficients a_l^L, b_l^L, a_l^N, and b_l^N, respectively. Non-trivial solutions for both systems are only achieved if their determinants are zero, leading to a set of discrete modes with angular frequencies ω_l^n for each l and n-th order, corresponding to the expression given in Eq. 2.106.

The considerations presented in this section are the fundamental of theoretical methods dealing with the scattering of plane waves on single and multiple spheres presented in Sect. 3.4 in Chap. 3.

References

1. Landau LD, Lifshitz EM (1983) Elastizitätstheorie. Lehrbuch der theoretischen Physik. Akademie-Verlag, Berlin
2. Beltzer AI (1988) Acoustics of solids. Springer, Berlin
3. Liu ZY et al (2000) Phys Rev B 62:2446
4. Cheng W (2007) Hypersonic elastic excitations in soft mesoscopic structures. PhD thesis
5. Einstein A (1910) Ann Phys 338:1275
6. Cummins HZ, Gammon RW (1966) J Chem Phys 44:2785
7. Berne BJ, Pecora R (2000) Dynamic light scattering. Dover, Mineola
8. Kuok MH et al (2003) Phys Rev Lett 90:255502
9. Cheng W et al (2005) J Chem Phys 123:121104
10. Sandercock JR (2008)
11. Mock R, Hillebrands B, Sandercock JR (1987) J Phys E: Sci Instrum 20:656
12. Still T et al (2008) J Phys: Condens Matter 20:404203
13. Cheng W et al (2007) Macromolecules 40:7283
14. Cheng W et al (2006) Nat Mater 5:830
15. Lamb H (1882) Proc Lond Math Soc S1–13:189
16. Montagna M (2008) Phys Rev B 77:045418
17. Mazurenko DA et al (2007) Phys Rev B 75:161102
18. Psarobas IE, Stefanou N, Modinos A (2000) Phys Rev B 62:278

Chapter 3
Methods

3.1 Vertical Lifting Deposition and Colloidal Crystals

The assembly of colloids into well defined coherent structures commonly occurs under the influence of external fields, e.g., gravitational sedimentation [1], electrophoretic deposition [2], or vertical deposition either by evaporation [3] or lifting the substrate [4] (Fig. 3.1).

In the vertical lifting deposition method upon immersion of a hydrophilic substrate into a colloidal dispersion a meniscus at the substrate is formed. Evaporation takes place at the three phase contact lines (air, dispersion, and substrate), which causes a solvent flux towards the meniscus, as shown in Fig. 3.2. Thus, colloidal particles are constantly transported with the liquid to the crystallization front. An interplay of long-range attractive and short-range repulsive forces causes the self-assembly of the colloidal material into a face-centered cubic (*fcc*) or hexagonally close packed (*hcp*) crystal [5, 6]. In order to control the thickness of such a colloidal crystal—a critical parameter for further use in ensuing applications—the substrate is withdrawn from the dispersion at a certain speed at given environmental parameters such as temperature and humidity. Besides the fabrication of such 'simple' colloidal crystals also more complex systems like binary [7, 8] and ternary colloidal crystals [9] were demonstrated. The colloidal crystals that are topic of this article are produced using an enhanced vertical lifting apparatus by Retsch [10].

Alongside with this research, also the counterpart to the highly ordered crystals—colloidal glasses [11, 12]—comprising of two distinct, monodisperse latex particles have already been developed [13]. Doping of the colloidal crystal with removable moieties (sacrificial templates) opens a pathway to the designed introduction of defects, which are highly interesting with respect to their contribution to phononic properties. At the same time, colloidal crystals and glasses serve as templates for the fabrication of so-called inverse opals [16]. These materials exhibit an interconnected 3D network with high surface area, since the constituent spheres of the colloidal crystals have been removed. Inverse opals have attracted strong interest in photonic
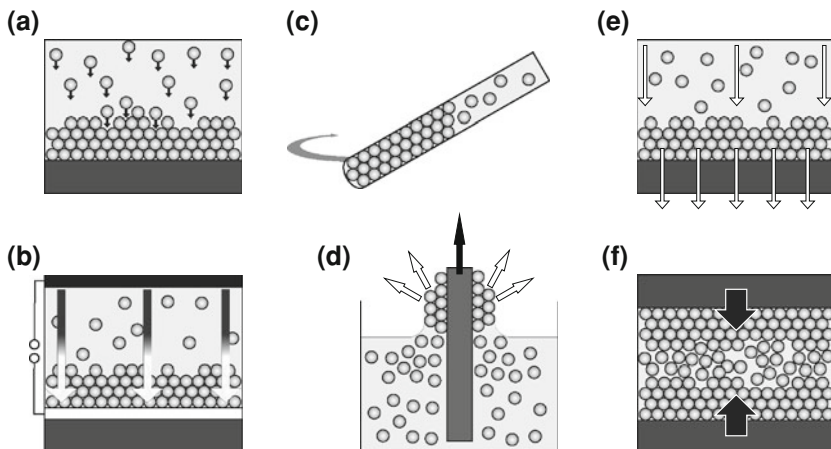
Fig. 3.1 Self assembly of colloidal crystals by **a** sedimentation, **b** electrodeposition, **c** centrifugation, **d** vertical deposition (cf. Fig. 3.2), **e** filtering, or **f** compression molding (according to [13])

Fig. 3.2 Schematic draw of the colloidal crystallization process in a vertical lifting deposition apparatus. The black arrow symbolizes the moving direction of the substrate by an adjustable stepper motor with small step size (not drawn). The surrounding climate chamber allows full control over air temperature and humidity, which are important parameter in the crystallization process (according to [13])
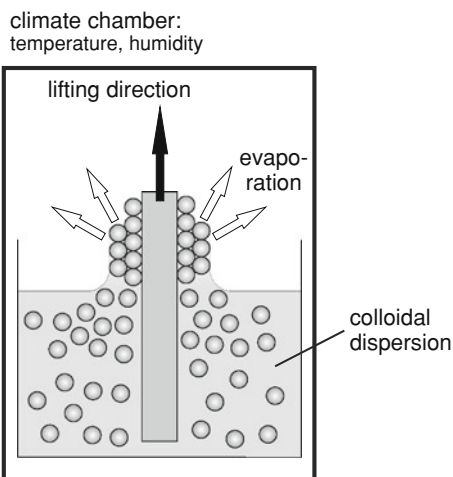
crystal research, due to their full photonic band gap [16, 17], and are also promising but unexplored materials for phononic experiments.

Complementary to the vertical deposition method a technique for the fabrication of large area colloidal monolayers has been recently established. This new method itself gives access to highly interesting new materials. Multiple stacks of colloids of various diameters as well as deposition on uneven or curved substrates have been demonstrated. Controlled etching of such a colloidal monolayer allows for the first time the fabrication of large areas of non-close-packed structures [18]. Finally, colloidal monolayers are well known and widely used for surface patterning. Vertical lifting deposition, colloidal monolayer fabrication and the

combination of both are powerful tools in order to rationally design new periodic functional materials with generic possibilities for defect tuning, creation of multi-layers, colloidal glasses, and inverse opals.

3.2 Melt Compression

Vertical lifting deposition is a method that delivers high quality colloidal crystals several tens of microns thick and with cm^2 areas. Although, in principle it would be possible to upscale the method, it would be unpractical and slow to produce much larger and thicker samples by that. A technique that is much better suited if fast and large scale hybrid material films of thickness up to the millimeter range is needed is the melt compression (or compression molding) technique that is schematically shown in Fig. 3.1f and in more detail in Fig. 3.3a.

   Melt compression can be utilized to prepare films out of hard core/soft shell core–shell particles, where the soft shell becomes the matrix and the hard cores form a crystalline (usually *fcc*) lattice, whose spacing depends on the initial volume ratio of core and shell materials. The preparation starts with the coagulation of the latex dispersion in a rubbery mass. When the soft shell is an elastomer with low T_g, e.g., poly(ethyl acrylate) (PEA), the shells form a continuous matrix in which the cores, e.g., harder polymers like polystyrene or oxides like silica, are dispersed. At DKI the mass is shaped into a cylindrical sample, which is uniaxially compressed at 170 °C in a Collin 300 press, with an initial pressure of 1 bar and a final pressure of 50 bar [19]. In the beginning of the pressing process, the first crystalline layers appear on the plates of the press. As shown in Fig. 3.3a, the pressure creates a horizontal flow perpendicular to the direction of compression. The order increases with pressure by the sequent formation of new crystalline layers above the already existing layers in order to achieve the densest packing. Finally, the whole film should be crystalline. It could be shown only recently that in such films the direction corresponding to the (111) plane of the *fcc* lattice is radial from the center of the round press cylinder, i.e., multi-domain ordering must be assumed, however, the crystallographic directions are well defined [20].
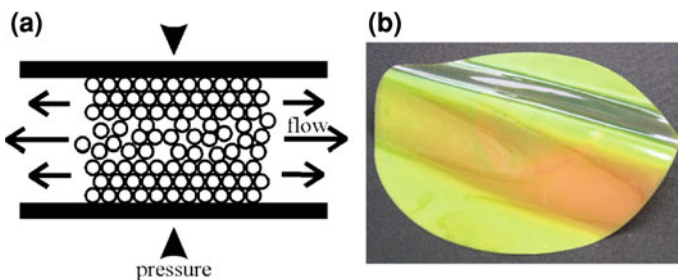
Fig. 3.3 **a** The flowing melt crystallizes along the plates of the press under uniaxial compression [19]. **b** Melt compressed polymer opal film with PS core and PEA shell [20]

Figure 3.3 shows a typical film prepared consisting of PS cores and PEA matrix. It is obvious that in this case the particle size is chosen that way the film acts as a photonic crystal, since against the dark background the film reflects the green light under Bragg conditions. Where it is bended, the angle to the light changes and it is reflected on another crystallographic plane, hence the color changes.

3.3 Polymer and Colloid Characterization Techniques

The aim of this section is to introduce very briefly the different auxiliary techniques applied in this thesis to characterize polymer and colloid samples, including spectroscopy, electron microscopy, calorimetry, density determination, and size exclusion methods.

3.3.1 Photon Correlation Spectroscopy

The photon correlation spectroscopy (PCS), also known as dynamic light scattering, is a light scattering technique that can be used to obtain the size distribution of small particles ($d < \lambda$) in diluted solution. When laser light hits small particles, Rayleigh scattering occurs in all directions. Because the small particles undergo Brownian motion in the liquid, the relative position of the scatterers within the scattering volume is constantly changing. This results in a time-dependent scattering intensity fluctuation, because the monochromatic and coherent laser light is scattered on the moving scatterers. The light scattered from the individual scatterers interferes with the light scattered on all the other particles. By using a correlator at a given scattering angle θ, i.e., at a given wave vector $\mathbf{q}$, one can record the time–correlation function

$$G(q, \tau) = \langle I(q, t)I(q, t + \tau) \rangle = \lim_{T \to \infty} \frac{1}{T} \int_0^\infty I(q, t)I(q, t + \tau)dt \qquad (3.1)$$

with $I(q, t)$ being the scattering intensity at time t and wave vector of magnitude q. Thus $I(q, t)$ is randomly fluctuating with time due to particle motion, $G(q, \tau)$ is decreasing exponentially from its initial value $G(q, 0)$ to zero for $\tau \to \infty$—or, to be exact, from $\langle I^2 \rangle$ to $\langle I \rangle^2$. The so-called normalized second order autocorrelation curve is generated from the intensity trace as follows:

$$g^2(q, \tau) = \frac{\langle I(t)I(t + \tau) \rangle}{\langle I(t) \rangle^2}. \qquad (3.2)$$

In the simplest case of monodisperse spheres, the autocorrelation function decays as a single exponential decay, which is directly related to the diffusion coefficient D.

When the viscosity η of the liquid is known, D gives the radius of the spherical particles r by the Stokes–Einstein relation

$$D = \frac{k_B T}{6\pi\eta r}.$$
(3.3)

All PCS experiments in this thesis were performed by myself on a setup built in-house at MPIP.

3.3.2 Electron Microscopy

The common characteristics of all types of electron microscopes is that electron (particle) beams are used to illuminate a sample and to create a magnified image. Fast electrons are generated by electron guns, consisting of an electron source (cathode), an accelerating anode, and electron lenses to collimate and focus the electron beam. The de Broglie wavelength of a particle with particle momentum p is

$$\lambda = \frac{h}{p} = \frac{h}{\gamma m_e v}$$
(3.4)

where h is Planck's constant and $\gamma = \sqrt{1 - v^2/v^2}$ the Lorentz factor for very high velocities v. For an electron with mass m_e, the wavelength of the electron particle beam depends on the velocity of the electrons, i.e., on the acceleration voltage (usually in the order of several kilovolts). Usual electron wavelengths are $\ll 1$ nm, which is much smaller than the wavelength of the light used in optical microscopes (200–1000 nm). Therefore the theoretical resolution limit is extremely low for electron microscopes, but in practical work resolution is limited by aberrations of the technical components; however, still orders of magnitudes better than in an normal optical microscope. By the use of electron lenses (either magnetic or electrostatic) with electronically adjustable foci, no movable objective system is needed in an electron microscope. Principally, there are two main types of electron microscopes, scanning electron microscopes (SEM) and transmission electron microscopes (TEM).

In the SEM a thin electron beam rasters the probed surface. In the same time electrons that are emitted or scattered from the probed object are detected and the registered intensity is correlated to the intensity value of the scanned pixel. Typically, in a SEM setup secondary electrons, back scattered electrons or, less often, cathode luminescence signals are detected. The most important strength of a SEM is the ability in displaying surfaces in high resolution with great depth of view.

On the other hand, the transmission electron microscope probes not only the surface but the whole gauge of a thin (some nanometer up to several micrometer) sample using a transmission geometry. Here, the beam is usually not scanning.

A broader beam is illuminating a part of the sample and the transmitted electron intensity is imaged onto a fluorescent viewing screen and recorded by a CCD camera for further computing.

Electron microscope pictures shown in this thesis are recorded by Markus Retsch, Gabrielle Schaefer, Gunnar Glasser, or Maren Mueller at different setups at MPIP.

3.3.3 Differential Scanning Calorimetry

The differential scanning calorimetry (DSC) is a variation of caloric thermo-analysis techniques, as there are also differential thermal analysis (DTA) or thermo gravimetry [21]. DSC is an isotherm technique. The sample and a reference substance are heated simultaneously in a way that both species have always the same temperature, i.e., $\Delta T = 0$ (heat compensation). Usually, the sample is heated (and cooled down) with a well defined temperature rate (mostly 1–20 K/min). Therefore, a different amount of heat ΔQ has to be added to the sample in comparison to the reference substance, which shows in ideal case a linear dQ/dT. The measurement records now the change of the sample with time $d(\Delta Q)/dt$ or with temperature $d(\Delta Q)/dT$, respectively. In the resulting thermogram exothermal phase transitions (e.g., crystallization) result in a peak with relative maximum, while endothermal transitions (e.g., melting) result in a peak with a relative minimum in the $d(\Delta Q)/dt$ or $d(\Delta Q)/dT$ curve. The integrals over the transition peaks give the transition heat exchanged in the respective transition.

DSC experiments in this thesis are performed by Raeder and Droege at MPIP and in the group of Prof. M. Ediger at University of Wisconsin, Madison, USA.

3.3.4 Density Gradient Column

In some cases the exact density of a sample is needed. While for polymers or colloids the direct measurement of volume and weight might be sophisticated, the use of a density gradient column is a popular method to measure a sample's mass density [21]. The column is a long vertically standing glass, which is filled with a liquid whose density is increasing gradually from top to bottom. This can, e.g., be realized by using a special double-flask setup in which two aqueous solutions of a salt with two different concentrations (and therefore different densities) are mixed to a solution with continuously changing concentration and density, which is carefully poured in the column [23, 24]. The density gradient is then calibrated using several floaters of well known density. Drawing the calibration curve of floater density against floating hight in the column, the density of other samples can be determined by flotation.

The density gradient column technique is often used to measure the crystallinity of a polymer. The degree of crystallization w_c is defined as

$$w_c = \frac{\varrho_c}{\varrho} \frac{\varrho - \varrho_a}{\varrho_c - \varrho_a} \tag{3.5}$$

with ϱ, ϱ_c, and ϱ_a being the density of the probed sample, the purely crystalline polymer, and the purely amorphous polymer, respectively. ϱ_c is accessible from the crystal structure, ϱ and ϱ_a can be obtained by flotation in the density gradient column. To obtain a completely amorphous sample, the polymer has to be molten and quenched to low temperatures with effectual celerity.

3.3.5 Wide Angle X-ray Scattering

Another method to determine the degree of crystallinity is the wide angle X-ray scattering technique. X-ray structure analysis is in general the most common method to measure crystal structures. When we took the atoms in the crystal as points in a real space lattice and transform the lattice into reciprocal space, the distance between two atoms in real space is now the distance it d between lattice planes. When a monodisperse, coherent X-ray beam is scattered on parallel lattice planes, the scattered beams interfere constructively when

$$2d \sin \phi = n\lambda \qquad (n = 1, 2, 3, \ldots). \tag{3.6}$$

ϕ is the glancing angle between the incident beam and the scattering plane and λ the wave length of the X-ray beam. Equation 3.6 is the Bragg condition for X-ray scattering. When scanning a range of scattering angles at some distinct angles, where the Bragg condition is fulfilled, the constructive interferences occur as sharp crystalline peaks in the scattering spectrum. In partially crystalline samples the X-ray spectrum at wide angles will consist of some distinct sharp peaks but also of an underlaying broad halo, which originates from the amorphous parts of the sample. Integrating these two areas in the spectrum gives access to the degree of crystallization, which is

$$w_c = \frac{A_c}{A_c + A_a}. \tag{3.7}$$

With A_c and A_a representing the areas under the curve of the crystalline signals and the amorphous halo. The discrimination of both parts is highly subjective, which makes the results less accurate [21].

3.3.6 UV/VIS Spectroscopy

Ultraviolet–visible spectroscopy (UV/VIS) is the spectroscopy of photons in the UV and visible region, usually the probing light has wavelengths between about

200 and 1000 nm. In this region of the electromagnetic spectrum, molecules undergo electronic transitions. The use of UV/VIS spectroscopy in polymer science lies mostly in the measurement of the concentration of a polymer in solution. If the solution is diluted, the Lambert–Beer law is valid:

$$A = \log(I_0/I) = \epsilon c L \tag{3.8}$$

A is the measured absorbance, I_0 is the intensity of the incident and I the intensity of the transmitted light. ϵ is the extinction coefficient, a material constant, L is the pathlength through the sample and c the concentration.

Most UV/VIS spectrometers work with two cuvettes, one with the sample, the other one as reference containing only the pure solvent, which are compared for every wavelength. All spectrometers consist of a light source, a dispersive element (lattice, prism, monochromator filters), the sample, and a detector. Mostly avalanche photo diodes are used. To obtain the spectrum the wavelength range of interest is scanned and absorbance (or transmittance) is plotted against wavelength.

For structures with periodic pattern of the dielectric constant, e.g., colloidal crystals, light is diffracted on these pattern with subsequent constructive and destructive interference. That is electromagnetic waves of distinct wavelengths cannot pass such structures in distinct crystallographic directions, dependent from the structure's periodicity length. This effect is referred to as photonic Bragg gap. The corresponding wavelength can be calculated as

$$\lambda_{\mathrm{Bragg}} = 2s n_{\mathrm{eff}} \sin \Theta, \tag{3.9}$$

where s is the periodicity in the regarded crystallographic direction, n_{eff} is the effective refractive index, and Θ is the angle between the incident light and the scattering plane of the crystal. For a *fcc* colloidal crystal with sphere diameter d, Eq. 3.9 becomes for the (111) plane of the crystal

$$\lambda_{\mathrm{Bragg}} = 1.63 d n_{\mathrm{eff}} \sin \Theta, \tag{3.10}$$

with

$$n_{\mathrm{eff}} = \sqrt{\phi_s n_s^2 + \phi_m n_m^2}, \tag{3.11}$$

where ϕ_s and n_s, or ϕ_m and n_m are the volume fraction and the refractive index of the spheres or the surrounding matrix, respectively [24].

In this thesis UV/VIS is used to characterize colloidal mixtures. The measurements have been performed by Retsch on the setup at MPIP.

3.3.7 Gel Permeation Chromatography

The gel permeation chromatography (GPC) is a size exclusion technique to determine the distribution of the molar mass in polymers. The principle idea is that

a diluted polymer solution travels a column containing a macroporous gel. If the single molecules are large they cannot penetrate the holes in the gel and therefore are not retarded, i.e., all molecules that are larger as a certain value, dependent from the nature of the gel, eluate together with the eluent. Smaller particles are retarded by entering the holes. With decreasing particle size the retardation time increases up to a certain point from which the eluation time is constant for all polymer chains, i.e., only polymers within a certain range of dimension are separated. Behind the column the amount of polymer in the eluted liquid as a function of time is recorded using different techniques as for example refractometry or UV/VIS spectroscopy. The intensity of the signal is proportional to the amount of eluted polymer. The easiest and most usual way to obtain quantitative data from the elution time versus intensity diagram is the comparison with monodisperse polymer standards, if available. In principle it is also possible to use an universal calibration for all polymers, because the size exclusion depends not really on the molecular weight but on the hydrodynamic radius R_h of the polymer molecule in solution. R_h correlates with the molecular weight M:

$$R_h = \Phi[\eta]M \tag{3.12}$$

with Φ being a constant and $[\eta]$ being the intrinsic viscosity given by the Mark–Houwink equation

$$[\eta] = K_\eta \left(\frac{M}{\text{g/mol}} \right)^{\alpha_\eta}, \tag{3.13}$$

where K_η and α_η are parameters depending on the polymer, its shape, and the solvent. The details of the sophisticated universal calibration is given in standard textbooks of macromolecular chemistry and physics [21].

3.4 Theoretical Calculations

The vibrations of individual spheres in different matrices as well as the phononic band diagram in mesostructured media is widely discussed in terms of experimental results mainly by BLS in this thesis. However, in order to come to valueble conclusions, the most powerful approach is to compare the experimental data with data calculated within the appropriate theories leading to either scattering cross sections when talking about the vibrations of individual particles or phononic band structures when talking about the phononic dispersion relation of the investigated systems. Taking well-known parameters for the calculations allows certainty about the nature of the experimentally observed effects, while on the other hand the use of theoretical important parameters as free fit parameters can be utilized to extract (e.g., nanomechanical) information from the measured spectra.

In this section I want to briefly describe the calculation methods used in this thesis. Starting from the considerations in Sect. 2.3.3 in Chap. 2, I will introduce the scattering cross section obtained from the scattering of a plane wave on a

single spherical scatterer. From that I will describe the related plane-wave method to calculate the band structure of periodic composites. Anyhow, the more powerful method to do the latter and more important for this thesis is the (layer) multiple-scattering approach, which will be presented concludingly. Finally, the finite element approach is discussed very briefly.

3.4.1 Single-sphere Scattering Cross-section Calculations

To calculate the scattering cross-section of a single sphere [25], one can calculate the scattering of an incident plane longitudinal wave of the form

$$u^{inc}(r) = \sum_{lm} \left(c_{lm}^L \frac{1}{q_l} \nabla [R_l(k_l r) Y_{lm}(\hat{r})] \right) \tag{3.14}$$

or of a transverse wave of the form

$$u^{inc}(r) = \sum_{lm} \left(c_{lm}^M R_l(k_t r) Y_{lm}(\hat{r}) + c_{lm}^N \frac{i}{q_t} \nabla \times R_l(k_t r) Y_{lm}(\hat{r}) \right) \tag{3.15}$$

in analogy to Eq. 2.111 after decomposition into longitudinal and transverse components. This plane wave is propagating in a homogeneous medium. When the wave is incident on a solid homogeneous sphere, it is scattered by it, and the wave field in the matrix u^m now consists of the incident and the scattered field, u^{inc} and u^{sc}. That is

$$u^m = u^{inc} + u^{sc}. \tag{3.16}$$

The boundary conditions at the surface of the sphere, given above in Eqs. 2.107 and 2.108, must still be fulfilled and can be written now as

$$u^i|_{r=r_s} = u^{inc}|_{r=r_s} + u^{sc}|_{r=r_s} \tag{3.17}$$

and

$$\tau^i|_{r=r_s} = \tau^{inc}|_{r=r_s} + \tau^{sc}|_{r=r_s}, \tag{3.18}$$

with

$$u^{sc}(r) = \sum_{lm} d_{lm}^L l_{lm}(R, k_l^i) + d_{lm}^M m_{lm}(R, k_t^i) + d_{lm}^N n_{lm}(R, k_t^i). \tag{3.19}$$

It is shown that the coefficients for the incident wave c_{lm}^x (with $x = L, M, N$) are known a priori [25]. As discussed in Sect. 2.3.3 in Chap. 2, it is possible to decompose this system into six scalar equations that can be separated into an infinite number of equations that are functions of lm. When the coefficients c_{lm}^x are known, there remain only the coefficients a_{lm}^x, given in Eq. 2.109, and d_{lm}^x, given in

Fig. 3.4 Total dimensionless
scattering cross-section for a
polystyrene sphere in liquid
PDMS matrix (cf. Fig. 5.11 in
Chap. 5, cf. Fig. 3 in Ref.
[14]) for longitudinal incident
wave. The peaks are labeled
as spherical harmonics with
$l = 2, 3, 4, 1, 5, n = 1$ for
all resonances. The elastic
values used for the calcula-
tion are given in Table 5.4
in Chap. 5
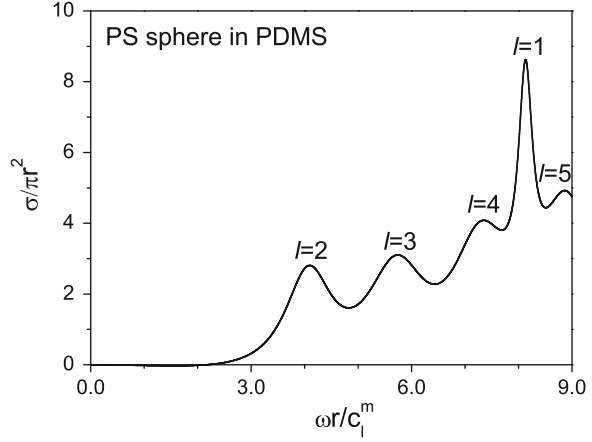
Eq. 3.19 for the field inside the spheres or the scattered field, respectively. Therefore exists for each *lm* a system of six equations with six unknowns that can be solved. The detailed algebraic analysis is done for example in Ref. [25].

The scattering cross-section σ is a measure for the likelihood of the physical interaction between an incident particle and another particle—in this case, the scattering of a wave by the single scatterer. It is defined as the ratio of the scattered energy flux to the incident energy flux per unit surface [26].

For the discussed case of an incident longitudinal wave (subscript *l*) the dimensionless scattering cross-section for a sphere with radius *r* is shown to become [27]:

$$\frac{\sigma_l}{\pi r^2} = \sum_{l=0}^{\infty} 4(2l+1) \left[\frac{|d_{lm}^L|^2}{|k_l^m r|^2} + l(l+1) \left(\frac{k_l^m r}{k_t^m r} \right) \frac{|d_{lm}^N|^2}{|k_t^m r|^2} \right]. \tag{3.20}$$

Figure 3.4 shows an example of a total dimensionless scattering cross-section, calculated for a polystyrene (PS) sphere in a poly(dimethyl siloxane) (PDMS) matrix. The normalization over the frequency is carried out by comparison with the longitudinal phase velocity in the matrix c_l^m.

3.4.2 The Plane Wave Method

As pointed out before (and more widely discussed in Chap. 5), in phononic systems consisting of many elastic scatterers in a matrix with different elastic properties, band gaps may occur in the band diagram, originating from either the periodicity of scattering layers (Bragg gap, BG) or from localized states in individual scatterers. The localized modes in the individual scatterers are given by the maxima in the scattering cross-section diagram discussed in Sect. 3.4.1, and it seems plausible to extend the method presented for the scattering cross-section to calculate the band diagram of phononic systems by assuming a plane wave

scattered now by many scatterers. In order to obtain analytical solutions, the plane wave (PW) method is restricted to periodic systems, i.e., phononic crystals [28].

The initial point of the PW approach is the general wave equation for a medium locally isotropic

$$\frac{\partial^2 u^i}{\partial t^2} = \frac{1}{\varrho}\left[\frac{\partial}{\partial x_i}\left(\lambda\frac{\partial u^l}{\partial x_l}\right) + \frac{\partial}{\partial x_l}\left\{\mu\left(\frac{\partial u^i}{\partial x_l}+\frac{\partial u^l}{\partial x_i}\right)\right\}\right] \quad i,l = 1,2,3. \qquad (3.21)$$

Here, $u^{i,l}$ and $x_{i,l}$ are the Cartesian components of the displacement vector $\boldsymbol{u}(\boldsymbol{r})$ and the position vector $\boldsymbol{r}$, respectively; $\lambda(\boldsymbol{r})$, $\mu(\boldsymbol{r})$, and $\varrho(\boldsymbol{r})$ are the Lamé coefficients and the local mass density, respectively, which are periodic functions of $\boldsymbol{r}$ with periodicity lattice vector $\boldsymbol{R}$:

$$f(\boldsymbol{r}+\boldsymbol{R}) = f(\boldsymbol{r}). \qquad (3.22)$$

As a result of the common periodicity of the three coefficients in Eq. 3.21, its solutions can be chosen to satisfy Bloch's relation

$$\boldsymbol{u}(\boldsymbol{r}) = e^{i k r}\boldsymbol{u}_k(\boldsymbol{r}), \qquad (3.23)$$

where $\boldsymbol{k}$ is a vector in the reciprocal lattice restricted within the first Brillouin zone (BZ) and $\boldsymbol{u}_k(\boldsymbol{r})$ is a periodic function. Hence, it is possible to expand $f(\boldsymbol{r})$ in a three-dimensional Fourier series:

$$f(\boldsymbol{r}) = \sum_{\boldsymbol{G}} f_G e^{i G r}, \qquad (3.24)$$

where the summation is over all reciprocal vectors $\boldsymbol{G}$, which can be written as sum with integer coefficients of the orthonormalized vectors that span the three-dimensional vector space in which $\boldsymbol{R}$ is the sum of the basis vectors.

With that one can rewrite Eq. 3.23 after expanding $\boldsymbol{u}_k$ in Fourier series as

$$\boldsymbol{u}(\boldsymbol{r}) = \sum_{\boldsymbol{G}} \boldsymbol{u}_k + G^{e^{i(k+G)r}}. \qquad (3.25)$$

The substitution of Eq. 3.24 (with $f = \lambda, \mu, \varrho^{-1}$) and Eq. 3.25 into Eq. 3.21 delivers finally the expression:

$$\begin{aligned}
\omega^2 c u^i_{k+G} = \sum_{G'}\Bigg[&\sum_{l,G}\varrho^{-1}_{G-G''}\big[\lambda_{G''-G'}(k+G')_l(k+G'')_i \\
&+\mu_{G''-G'}(k+G')_i(k+G'')_l\big]u^l_{k+G'} \\
&+\sum_{G''}\bigg(\varrho^{-1}_{G-G''}\times\mu_{G''-G'}\sum_{j}\big[(k+G')_j(k+G'')_j\big]\bigg)u^i_{k+G'}\Bigg].
\end{aligned} \qquad (3.26)$$

If the Fourier series in Eq. 3.25 is performed over M reciprocal vectors (i.e., for M scatterers in the periodic medium), Eq. 3.26 is reduced to a $3M \times 3M$ matrix

eigenvalue equation for the *3M* unknown coefficients $u^i_{k+G}(i = 1, 2, 3)$. Usually, $M > 400$ to achieve the desired convergence [28].

Note that for fluid systems, Eq. 3.26 can be simplified [27]. In liquids $\mu = 0$; by introducing the pressure $p = -\lambda \nabla u$, Eq. 3.21 can be written in the form

$$\lambda(r) \nabla \left[\varrho(r)^{-1} \nabla p(r) \right] + \omega^2 p(r) = 0. \tag{3.27}$$

Following the same considerations as for the (general) solid case one obtains for *M* terms in the Fourier sum a $M \times M$ system.

PW is a fast and easy-to-apply method to calculate the band diagram in fluid/ fluid or solid/solid systems, i.e., fluid or solid scatterers in matrices of the same aggregate state. However, it fails when dealing with solid/fluid systems, which are mostly discussed in this thesis.

When a solid scatterer is embedded in a liquid host, transverse waves cannot propagate in the matrix and Eq. 3.27 becomes the appropriate elastic wave equation. In that case the *M* eigenmodes for *M* scatterers correspond to purely longitudinal waves. However, it is known that even for a longitudinal incident wave, the field inside the scatterer will be both longitudinal and transverse, i.e., there are localized transverse modes inside the scatterer that cannot propagate [27, 29].

The approach that uses the full (including $\mu \neq 0$) wave equation (Eq. 3.21) fails because of the non-propagating character of these modes and leads to no convergence at all. Using Eq. 3.27 would ignore completely the transverse component of the wave within the scatterer as it would de facto replace the solid scatterer by the fluid scatterers of the same λ and μ. Although it leads to mathematically reasonable results, it was shown that these results are not suited to describe the reality [27].

Another limitation of the PW method is that it can be only applied on infinite periodic samples. This also means that it is unable to calculate the transmission properties. An approach to overcome these limitation is the multiple-scattering method that will be discussed in the next section.

3.4.3 The Multiple Scattering Method

The main idea behind the multiple scattering method is described schematically in Fig. 3.5. A plane wave in a homogeneous medium impinges on a system of N non-overlapping scatterers ($n = 1, 2, N$). The wave that impinges on each scatterer consists of N contributions, the incident wave and the outgoing waves from any of the N − 1 other scatterers.

With the coefficient notation used in the sections above, for a single scatterer the coefficients for the scattered wave field, d^x_{lm}, are related to the given coefficients (i.e., amplitudes) of the incident plane wave, c^x_{lm}:
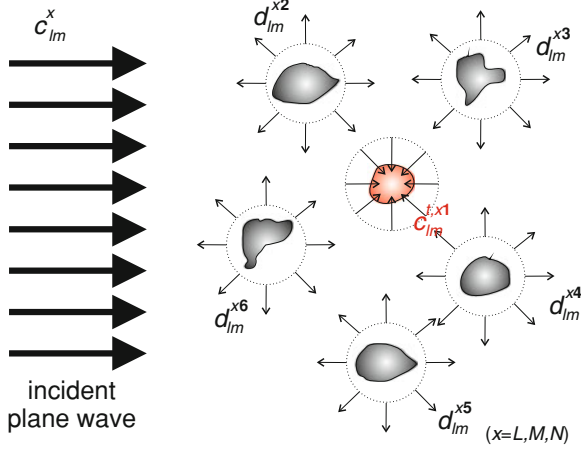
Fig. 3.5 Schematic draw of the multiple scattering mechanism. A plane incident wave (with coefficients c_{lm}^x) is impinging an ensemble of scatterers, which can have arbitrary shape. The total wave field acting on the n-th individual scatterer (with coefficients $c_{lm}^{t,xn}$), e.g., the scatterer 1 in the middle, is a summation over the impinging plane wave and the scattered waves from the other scatterers (with coefficients d_{lm}^{xn}; in our example for $n \neq 1$)

$$d_{lm}^x = \sum_{x',l'm'} T_{xlm;x'l'm'} c_{lm}^x. \tag{3.28}$$

The T-matrix is a 3×3-Tensor that can principally be calculated for scatterers of every arbitrary shape with no need of homogeneity. The calculation for homogeneous spheres can be found in literature [25] as well as the solutions for inhomogeneous core–shell particles [30].

Coming back to our system with N scatterers, the total wave field incident on the n-th scatterer is the sum of the incident plane wave and the wave field scattered from all scatterers $n' \neq n$.

$$u^{inc,n}(r - r_n) = u^{inc}(r - r_n) + \sum_{n' \neq n} u^{sc}(r_n - r_{n'}). \tag{3.29}$$

That is

$$
\begin{aligned}
u^{inc,n}(r - r_n) &= \sum_{lm} c_{lm}^{t,Ln} l_{lm}(R, k_l) + c_{lm}^{t,Mn} m_{lm}(R, k_t) + c_{lm}^{t,Nn} n_{lm}(R, k_t) \\
&= \sum_{lm} c_{lm}^L l_{lm}(R, k_l) + c_{lm}^M m_{lm}(R, k_t) + c_{lm}^N n_{lm}(R, k_t) \\
&\quad + \sum_{n' \neq n, lm} d_{lm}^{L,n'} l_{lm}(R, k_l) + d_{lm}^{M,n'} m_{lm}(R, k_t) + d_{lm}^{N,n'} n_{lm}(R, k_t)
\end{aligned} \tag{3.30}
$$

or

$$
\begin{aligned}
\boldsymbol{u}^{inc,n}(\boldsymbol{r} - \boldsymbol{r}_n) = \sum_{lm} \Bigg(&c_{lm}^L \frac{1}{k_l} \nabla [R_l(k_l r) Y_{lm}(\boldsymbol{r} - \boldsymbol{r}_n)] \\
&+ c_{lm}^M \nabla \times [(\boldsymbol{r} - \boldsymbol{r}_n) R_l(k_t r) Y_{lm}(\boldsymbol{r} - \boldsymbol{r}_n)] \\
&+ c_{lm}^N \frac{1}{k_t} \nabla \times \nabla \times [(\boldsymbol{r} - \boldsymbol{r}_n) R_l(k_t r) Y_{lm}(\boldsymbol{r} - \boldsymbol{r}_n)] \Bigg) \\
&+ \sum_{lm,n'} \Bigg(d_{lm}^{L,n'} \frac{1}{k_l} \nabla [R_l(k_l r) Y_{lm}(\boldsymbol{r}_n - \boldsymbol{r}_{n'})] \\
&+ d_{lm}^{M,n'} \nabla \times [(\boldsymbol{r}_n - \boldsymbol{r}_{n'}) R_l(k_t r) Y_{lm}(\boldsymbol{r}_n - \boldsymbol{r}_{n'})] \\
&+ d_{lm}^{N,n'} \frac{1}{k_t} \nabla \times \nabla \times [(\boldsymbol{r}_n - \boldsymbol{r}_{n'}) R_l(k_t r) Y_{lm}(\boldsymbol{r}_n - \boldsymbol{r}_{n'})] \Bigg).
\end{aligned}
\tag{3.31}
$$

In the last two equations the two sums on the right side belong to the incident plane wave (with coefficients c_{lm}^x, $x = L, M, N$) and to the scattered waves from the other scatterers (with coefficients $d_{lm}^{x,n'}$).

For the resulting total incident field the coefficients $c_{lm}^{t,xn}$ are introduced in Eq. 3.30. They are related to the scattering coefficients of the n-th scatterer $d_{lm}^{x,n}$ by the T-matrix (Eq. 3.28).

Doing so for all N scatterers, one obtains a system of $N\left[\sum_{l=0}^{l_{max}}(2l+1) + 2\sum_{l=1}^{l_{max}}(2l+1)\right]$ algebraic equations, in which the only known amplitudes are those for of the incident plane wave. With the assumption that terms with $l > l_{max}$ do not contribute significantly to the spherical wave expansion, this system can be solved numerically to determine all $d_{lm}^{x,n}$.

So far, the method is not restricted to an equal shape of all scatterers (however, for different shapes the T-matrix of all individual scatterers would have to be known) or to any periodicity, as the relative position of each pair of scatterers is considered in Eq. 3.31.

However, as the aim is to calculate the band structure in phononic crystals as function of the reduced wave vector $\boldsymbol{k}$ in the first Brillouin zone, the introduction of the crystal periodicity is needed. It was shown that in this case the phononic band structure can be calculated in analogy to the theory of Korringa [31], Kohn and Rostoker [32] (KKR theory) developed to solve the Schrödinger equation for electromagnetic waves in periodic lattices [33].

After introducing the pressure field

$$
p(\boldsymbol{r}) = \lambda \nabla \cdot \boldsymbol{u}(\boldsymbol{r}),
\tag{3.32}
$$

it is possible to write the wave equation for a periodic medium of solid scatterers in a fluid matrix as follows [33]:

$$
\nabla^2 p(\boldsymbol{r}) + \frac{\omega^2}{c_m} p(\boldsymbol{r}) + \omega^2 \left[\frac{1}{c^2(\boldsymbol{r})} \frac{1}{c_m^2}\right] p(\boldsymbol{r}) + \varrho(\boldsymbol{r}) \times \left[\nabla \frac{1}{\varrho(\boldsymbol{r})}\right] \nabla p(\boldsymbol{r}) = 0.
\tag{3.33}
$$

This can be written in analogy to the Schrödinger equation in the form

$$H_m(\boldsymbol{r})p(\boldsymbol{r}) + U(\boldsymbol{r})p(\boldsymbol{r}) = 0, \tag{3.34}$$

where $H_m(\boldsymbol{r})p(\boldsymbol{r}) = 0$ represents the wave equation for the matrix without scatterer ($H_m(\boldsymbol{r}) = \nabla^2 + \omega^2/c_m^2$). In a periodic system a Green's function approach can be chosen to reformulate Eq. 3.33.

$$p(\boldsymbol{r}) = \int_V G(\boldsymbol{r} - \boldsymbol{r}')V\boldsymbol{r}'p\boldsymbol{r}'d\boldsymbol{r}' \tag{3.35}$$

with Green's functions

$$G(\boldsymbol{r} - \boldsymbol{r}') = \sum_n e^{i\boldsymbol{k}\cdot\boldsymbol{R}_n} G_0(\boldsymbol{r} - \boldsymbol{r}' - \boldsymbol{R}_n) \tag{3.36}$$

and

$$G_0(\boldsymbol{r} - \boldsymbol{r}') = -\frac{1}{4\pi} \frac{e^{i|\boldsymbol{r}-\boldsymbol{r}'|\omega/c_m}}{|\boldsymbol{r} - \boldsymbol{r}'|}. \tag{3.37}$$

$\boldsymbol{R}_n$ is a Bloch's vector, so that

$$p(\boldsymbol{r} + \boldsymbol{R}_n) = e^{i\boldsymbol{k}\cdot\boldsymbol{R}_n}p(\boldsymbol{r}), \tag{3.38}$$

and the relation between the amplitudes of the scattered field at different lattice sites n and n' becomes [26]

$$d_{lm}^{x,n} = e^{i\boldsymbol{k}\cdot\boldsymbol{R}_n} d_{lm}^{x,n'}. \tag{3.39}$$

The next step is the expansion of $G(\boldsymbol{r} - \boldsymbol{r}')$ and $p(\boldsymbol{r}')$ into spherical functions of $\boldsymbol{r}$ and $\boldsymbol{r}'$. These calculations are performed in detail in Ref. [33]. In the end the final multiple-scattering equation appears to be

$$\sum_{l'm'} = \left(A_{lml'm'} - \frac{\omega}{c_m}\Im(d_{l'}^{-1})\delta_{ll'}\delta_{mm'}\right)a_{l'm'} = 0. \tag{3.40}$$

The coefficients $A_{lml'm'}$ are the so-called structure constants as they depend on $\boldsymbol{k}$, ω, and the periodic lattice structure, the coefficients $d_{l'}$ relate the incident to the scattered field.

Equation 3.40 represents a linear homogeneous algebraic system. Its nontrivial solutions give the eigenfrequencies of the periodic system and hence the dispersion relation.

An enhanced variant of the multiple-scattering method calculates the dispersion relation for samples consisting of different composites with two-dimensional periodicity and is called layer-multiple-scattering approach (LMS) [31, 35, 36]. For a slab parallel to a distinct crystallographic plane, the reduced vector parallel to this plane, $\boldsymbol{k}_\parallel$, is usually a conserved quantity. Therefore, LMS searches in each

individual slab propagating Bloch waves for given ω and $\boldsymbol{k}_{\parallel}$, which are the eigenmodes of the elastic field in that slab. It is an on-shell method since it operates at a given frequency. It was shown that LMS is a powerful method to determine the dispersion relation as well as the transmittance of three dimensionally structured systems. Example 3D phononic crystals can be regarded as a succession of planes of scatterers parallel to a chosen crystallographic plane. As already mentioned for the general MS approach, the LMS technique takes the full vector nature of the acoustic field into account and is therefore not limited to certain fluid/solid combinations, as for example PW is.

Note that nearly all calculations in this thesis using the single-sphere scattering cross-section and the multiple scattering algorithms have been performed by my co-worker Revekka Sainidou (University of Le Havre).

3.4.4 The Finite Element Method

The finite element method (FEM) is a numerical method to approximately solve partial differential equations. It is widely used in engineering and many other fields to simulate a wide range of different physical problems.

The main principle of the technique is that the treated body is initially discretized into a finite number of elements of finite size, which can be described by a finite number of parameters. Within these *finite elements*, basis functions are defined. Substitution of the linear combination of all utilized basis functions into the differential equation to solve for each individual element (e.g., for mechanical problems the equation of motion) in combination with the boundary conditions leads to a quadratic matrix, whose dimension is given as the product of the number of elements and the number of basis functions. This dimension is also the number of degrees of freedom of the system. The boundary conditions at the knots of neighbouring elements are often evident, e.g., in the case of a mechanical deformation, the displacement (and even the first derivative of the displacement) must be continuous at the boundary between two elements. Finally, a system of ordinary differential equations is obtained that can be solved directly, e.g., using Gaussian elemination. It is obvious that the quality of the approximation increases with the number of elements, as well as the effort for the calculation does.

In this thesis, FEM is utilized only marginally to display some eigenvibrations. These simulations have been performed by myself using the COMSOL Multiphysics software package.

References

1. Davis KE, Russel WB, Glantschnig WJ (1989) Science 245:507
2. Trau M, Saville DA, Aksay IA (1996) Science 272:706

3. Jiang P, Bertone JF, Hwang KS, Colvin VL (1999) Chem Mater 11:2132
4. Gu ZZ, Fujishima A, Sato O (2002) Chem Mater 14:760
5. Fustin CA, Glasser G, Spiess HW, Jonas U (2004) Langmuir 20:9114
6. Denkov N et al (1992) Langmuir 8:3183
7. Wang L, Baowen L (2008) Phys World 21:27
8. Tommaseo G et al (2007) J Chem Phys 126:014707
9. Wang J, Li Q, Knoll W, Jonas U (2006) J Am Chem Soc 128:15606
10. Fustin C-A, Glasser G, Spiess HW, Jonas U (2003) Adv Mater 15:1025
11. Pusey PN, van Megen W (1987) Phys Rev Lett 59:2083
12. García P, Sapienza R, Blanco A, López C (2007) Adv Mater 19:2597
13. Li Q et al (2008) Porous networks through colloidal templates topics in current chemistry. Springer, Heidelberg
14. Still T et al (2008) Phys Rev Lett 100:194301
15. Zakhidov AA et al (1998) Science 282:897
16. Li Z-Y, Zhang Z-Q (2000) Phys Rev B 62:1516
17. Li ZY, Zhang ZQ (2001) Adv Mater 13:433
18. Haginoya C, Ishibashi M, Koike K (1997) Appl Phys Lett 71:2934
19. Ruhl T, Spahn P, Hellmann GP (2003) Polymer 44:7625
20. Spahn P (2008) PhD thesis
21. Pursiainen OLJ et al (2008) Adv Mater 20:1484
22. Lechner MD, Gehrke K, Nordmeier EH (2003) Makromolekulare Chemie, 3rd edn. Birkhäuser, Basel
23. Linderstrom-Lang K (1937) Nature 139:713
24. Toth H, Fehlauer H (2004) Phys Unserer Zeit 35:76
25. Gaillot DP, Graugnard E, King JS, Summers CJ (2007) J Opt Soc Am B 24:990
26. Psarobas IE, Stefanou N, Modinos A (2000) Phys Rev B 62:278
27. Cheng W (2007) Hypersonic elastic excitations in soft mesoscopic structures. PhD thesis
28. Kafesaki M, Economou EN (1995) Phys Rev B 52:13317
29. Economou EN, Sigalas M (1994) J Acoust Soc Am 95:1734
30. Einspruch N, Truell R (1960) J Appl Phys 31:806
31. Sainidou R, Stefanou N, Psarobas IE, Modinos A (2005) Comp Phys Commun 166:197
32. Korringa J (1947) Physica 13:392
33. Kohn W, Rostoker N (1954) Phys Rev 94:1111
34. Kafesaki M, Economou EN (1999) Phys Rev B 60:11993
35. Liu ZY et al (2000) Phys Rev B 62:2446
36. Sainidou R, Stefanou N, Psarobas IE, Modinos A (2005) Z Kristallogr 220:848

Chapter 4
The Vibrations of Individual Colloids

4.1 Introduction

Nowadays, colloidal nano- and mesoscale particles with dimensions from few nanometers up to 1 μm are used in a growing number of applications, e.g., as fillers in polymer thin films to enhance thermo-mechanical properties [1], to improve coatings performance and as components in nanocomposites operating as photonic [2], plasmonic [3], and phononic structures [4]. For a wide range of such applications, information on the mechanical properties and the stability of these colloidal composite materials are of paramount importance. Conventional rheological measurements on the macroscopic system are often not sufficient to elucidate the specific contributions of the nanostructured components. At the nanoscale, forces negligible in macroscopic systems, such as depletion, interfacial, and confinement effects often become significant, and the behavior of the same materials in nanoscopic systems can considerably deviate from the bulk. A fundamental understanding of transport and thermomechanical properties of nanostructured materials is a precondition to address a specific need by structural engineering. In the case of colloidal composite materials, the vibrational modes confined to the individual particles result from the elastic motion at the nanoscale and should sensitively depend on the geometrical, architectural, interfacial, and mechanical characteristics of the particles. However, there is a paucity of nondestructive experimental techniques to probe this 'music' of particle vibrations since both high frequency resolution and sensitivity are required to detect the numerous eigenmodes. Raman scattering [5, 6] has been utilized to measure few eigenfrequencies of nanoparticles with dimension below 10 nm, whereas Brillouin light scattering (BLS) [7–9] and optical pulse-probe techniques [10–12] can probe, respectively, the spontaneous and stimulated vibrations confined in sub-micrometer particles. In the latter technique, the excited acoustic oscillations are observed in the form of modulations of the transient reflectivity of the probe laser, and hence the particles must possess good reflectance, e.g., by introduction of gold shells. In BLS, light is scattered inelastically by the density fluctuations (phonons)

associated with these particle localized modes at thermal equilibrium and there are no further stringent conditions.

Self-assembly of colloidal particles in periodic structures [13, 14] (cf. Sect. 3.1 in Chap. 3) has received special attention as the resulting photonic and phononic crystals have revealed the potential of manipulating the propagation of electro-magnetic and elastic waves. Their propagation is forbidden at 'Bragg' frequencies or wavelengths commensurate with the lattice constant, which for sub-micrometer particles is comparable with the wavelength of the visible light. Synthetic opals from these particles can exhibit dual, i.e., hypersonic phononic and photonic [14, 15] band gaps allowing for acousto-optical interactions [16]. Moreover, the design of sub-micron particles that can act as strong localized resonant elements in an appropriate matrix provides the possibility for additional gaps well below the Bragg frequency, termed hybridization gaps (cf. Chap. 5) [17, 18]. The opening of band gaps perturbs the phononic density of states which impacts physical quantities such as group velocity, heat capacity and heat conductivity in dielectrics being potentially useful for thermoelectric devices [19, 20]. One of the pivotal concerns for these systems is the phonon dispersion, which is essentially defined by the elastic parameters of the constituent components and the spatial architecture of the composite system. Colloid science can create novel materials that possess spatial variation of density and elastic constants at the nanoscale but their mechanical characterization remains difficult.

If vibrations are excited in a finite elastic body, it can act as an elastic resonator. The elastic standing waves in stress-free boundary are referred to vibration eigenmodes. In the case of elastic spheres, the analytical solutions were first derived by Lamb [21]. The eigenmodes of spheres can be classified as torsional and spheroidal modes, both labeled by three indices (nlm), which describe the angular (lm) and radial (n) dependence of the displacement. Spheroidal resonance modes are fully characterized by the angular momentum l, imposed by the spherical symmetry of the particle, and n, where n denotes the n-th order solution for a given l (cf. Sect. 2.3.3 in Chap. 2) [21, 22]. The use of inelastic light scattering to measure vibration eigenmodes of small spherical particles was first performed experimentally by low-frequency Raman scattering (RS) [22]. Due to selection rules only two distinct vibration eigenmodes contribute to the RS of spherical particles with diameter (d) much smaller than the wavelength of the probing light ($d \ll \lambda$) [23]. For bigger spheres with $d \sim \lambda$, Brillouin light scattering (BLS) in the GHz-range becomes the technique of choice [7, 8, 24]. Due to the consideration of higher-order terms in the electric multipole expansion and of retardation effects [25, 26], BLS can resolve a multitude of eigenmodes.

For homogeneous transparent systems, BLS measures the spectrum of light inelastically scattered by the acoustic phonons with a selected polarization [longitudinal (l) or transverse (t)] and wave vector $\mathbf{q}$, leading to spectra consisting of doublets at $\omega_B = \pm cq$ around the central elastic Rayleigh line. Since c in soft materials like polymers is of the order of 10^3 ms^{-1} and q is in the range $1-30 \text{ μm}^{-1}$, the frequencies $f = \omega_B/2\pi$ fall into the GHz range. This yields the

two elastic constants $C_{11} = \varrho c_l^2$ and $C_{44} = \varrho c_t^2$ with c_l and c_t being the two phase sound velocities and ϱ being the mass density. For inhomogeneous turbid systems, e.g., powder of mesoscopic ($d \sim \lambda$) particles, $\mathbf{q}$ is ill-defined in the BLS experiment due to strong multiple scattering. BLS can measure only localized in space (and hence q-independent) vibrational modes. Each resonance mode appearing at frequency $f(n, l)$ is characterized by the angular momentum l of the n-th order. The frequencies of the individual vibrational modes depend on their rigidity, mass density, and size dimensions of the particles. For the case of homogeneous spherical particles the frequencies are given by Lamb in Eq. 2.106.

The frequencies can be theoretically obtained from the calculated density of states (DOS) spectra of a single sphere as a function of the two elastic constants and the inverse diameter. For polystyrene spheres, e.g., the constant in Eq. 2.106 becomes $x(1, 2) \approx 0.85$ and $R(c_l, c_t) = C_{44}$ with no adjustable parameter [8].

In this chapter the state-of-the-art for BLS measurements on homogeneous mesoscopic spherical particles is briefly summarized. Novel studies dealing with mixtures ('hybrids') of different kind of spheres are presented as well as a study on spheres prepared as copolymers with different compositions to elucidate the influence of the next neighbors and of the rigidity on the mechanic vibrations in the mesoscale. The second part of the chapter extends the scope on nanostructured colloids. Hybrid material spherical core–shell particles are investigated as model systems. Therein, especially the influence of heat on polymer cores contained in a hard silica-shell and the influence of the composition in the vice versa case of silica–PMMA core–shell particles with different ratio of core size to total diameter on the vibrational eigenmodes is of interest.

Due to some theoretical support, these studies give an unprecedentedly comprehensive picture of the elastic properties of individual colloids, although still numerous questions have to stay open—e.g., when dealing with structures going beyond the investigated 'easy' spherical model systems.

4.2 Elastic Vibrations in Homogeneous Polymer Colloids

4.2.1 The 'music' of the spheres

As pointed out in Sect. 2.3.3 in Chap. 2 and in the Introduction of this chapter, BLS can be utilized to measure the resonance modes of dry non-transparent colloidal crystals. Due to the strong elastic form factor of the individual spheres and the large elastical contrast with the surrounding air, the opals show strong multiple scattering. In such samples the inelastic scattering from localized modes leads to incoherent BLS in analogy to the Raman scattering.

Thus BLS can be utilized to analyze the particle eigenfrequencies, describing the spheroidal (n, l)-modes, with n as the n-th mode of the l-th spherical harmonic. The first demonstration of the feasibility of the BLS experiment was shown by Penciu et al. in the case of dilute suspensions of giant core–shell micelles [9]. Few

years later Kuok et al. have extended this application to closely packed mono-disperse silica nanospheres in air [7, 27]. Up to six localized particle eigenmodes have been resolved out of the numerous possible modes, probably due to the weak scattering of moderately compressible silica. In a subsequent study, artificial soft colloidal crystals, composed of monodisperse submicrometer polystyrene (PS) spheres with diameter d between 170 and 856 nm have been investigated [8]. Up to 21 **q**-independent eigenmodes have been resolved.

Figure 4.1 shows exemplary three BLS spectra taken from colloidal PS opals with diameters 180, 360 and 550 nm [24]. The resonance frequencies scale with $1/d$ (Fig. 4.2), which is in perfect agreement with Lamb's theory [21] and the theoretical predictions based on single-phonon scattering cross-section calculations (cf. Sect. 3.4.1 in Chap. 3) [28, 29]. In the computations, a plane sound wave propagating in air and impinging upon a single PS sphere was considered and after subtracting the scattering amplitude for a rigid sphere of equal size, the sphere eigenmodes appear as resonance peaks in the plot of scattering cross-section versus frequency. Thereby the resonance frequencies $f(n, l)$ can be identified as mode with angular momentum quantum number l of n-th order.

Using the experimental values for the longitudinal sound velocity $c_l = 2350 \text{ ms}^{-1}$, the transverse sound velocity $c_t = 1210 \text{ ms}^{-1}$ and mass density $\varrho = 1050 \text{ kg m}^{-3}$ of bulk PS, all resolved frequencies are quantitatively captured within 3% with no adjustable parameter. The product of frequency and diameter is
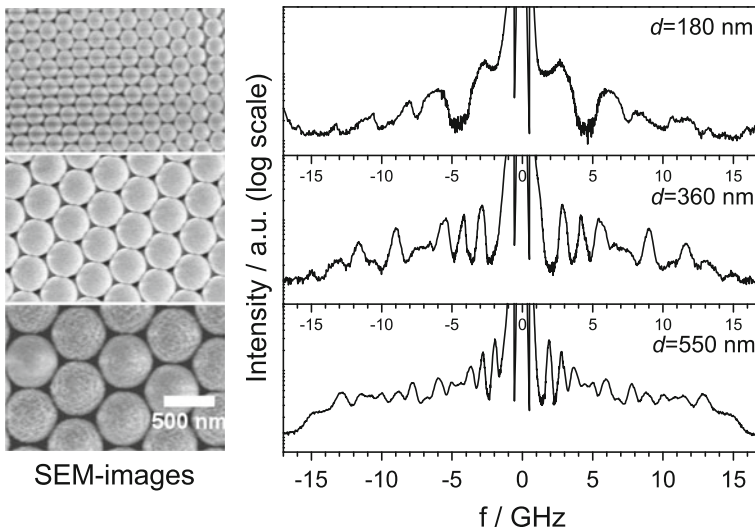
Fig. 4.1 *Left* SEM—images of colloidal PS crystals with $d = 180$, 360 and 550 nm (*top* to *bottom*); *right* corresponding **q**-independent BLS eigenmode spectra of the PS opals. To capture all possible vibrations, two spectra recorded at two different free spectral ranges are superimposed. Spectra are recorded at 20° ($q = 0.0041 \text{ nm}^{-1}$). For the thickest particles ($d = 550$ nm, *bottom*) there is a clear cut-off bump around 15 GHz, which is the frequency of the acoustic phonon in PS at backscattering geometry [24]

Fig. 4.2 Experimental resonance frequencies of the PS opals from Fig. 4.16 (solid symbols) versus the reciprocal particle diameter. The solid lines denote the computed resonance frequencies [8, 24]. The open squares denote the frequencies for the first seven modes simulated by the finite element methode for PS spheres with $d = 540$ nm
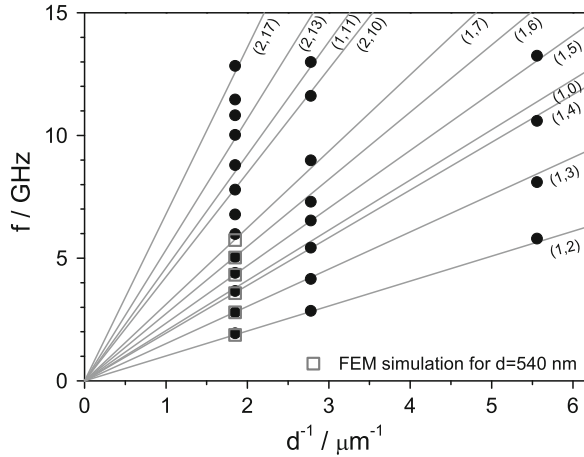
obtained to be a constant for every mode, as is indicated by the solid lines in Fig. 4.2, which represent the computed modes (n, l). It is shown that the first modes are the same for all samples with the $(1, 2)$-mode being the lowest and most intense one.

From the longitudinal and transversal sound velocities the elastic constants are directly accessible. These are the Poisson ratio σ, the Young modulus E, and the shear modulus G (Sect. 2.1.1 in Chap. 2) [30]. Additionally to the elastic constants, even more information can be extracted from these spectra. The peculiar line shape can be regarded as a sensitive index of the particle size distribution. An application with technological relevance was the determination of the mechanical properties of spherical glassy $CaCO_3$-particles [30]. The particles with mono-modal size distribution and diameters in the range between 400 and 1500 nm were made from amorphous $CaCO_3$, with unknown elastic properties as yet. Eigenmode acoustic spectra of the spheres were recorded and six or seven resonance modes could be resolved. By calculating c_l from the cut-off frequencies and taking c_t and the density ϱ as floating fit parameters, all signals could be assigned to the vibrational eigenmodes and a very good agreement between theory and experiment was achieved. From the obtained values for c_l, c_t and ϱ the Poisson ratio σ, Young modulus E and shear modulus G were then reported. In conformity with the analysis of the SEM-pictures all investigated colloidal samples in this thesis are found to be quite monodisperse.

For the largest particle size in Fig. 4.1 (or Fig. 2 in [8]) there is clearly a kind of cut-off frequency at about 14–15 GHz after which the scattering intensity decreases rapidly towards zero. Because of strong multiple scattering, $\mathbf{q}$ is not defined. The highest frequency contribution corresponds to the acoustic phonon in bulk PS under backscattering conditions, i.e., $q_{BS} = 4\pi n/\lambda_0$. Using $n = 1.59$ for the refractive index of PS and for the laser wavelength $\lambda_0 = 532$ nm, $q_{BS} = 0.0376$ nm^{-1}, and hence a cut-off frequency for the longitudinal acoustic phonon ($c_l = 2350$ ms^{-1}) is indeed expected at 14.05 GHz.

A more detailed theoretical treatment of the Brillouin and Raman scattering from the acoustic vibrations of spherical particles with diameters in the order of magnitude of the wavelength of light was presented very recently by Montagna [25]. While for very small particles ($qR \ll 1$, with $R = d/2$) only the 'Raman-term' that originates either from local field changes due to dipole induced dipoles or from electronic polarizability changes with the change of the atomic distances is important, for particles with diameters $d \sim \lambda_0$ also the 'Brillouin-term' becomes important. The latter comes from the polarization fluctuations caused by spacial displacement of scatterers by acoustic vibrations. Detailed calculations are performed, which show that for a given l the intensity of a resonance mode with a certain n strongly depends on qR, hence on the particle size. However, a direct comparison with the experiment is not straightforward due to the ill-defined **q**. Nevertheless, it is pointed out that for larger particle sizes the range of qR also increases ($0 \le qR \le q_{BS}R$). In a given range of qR only the modes resonance frequencies that are close to that of the acoustic phonon in the bulk, i.e., $\omega \approx qc_l$, contribute considerably to the Brillouin scattering. The total number of modes with higher n and l that have their intensity maximum in the larger qR-range also increases. This rationalizes the observation of the highest number of modes for the better-formed cut-off for the largest particles in Fig. 4.1. It should be noted that when calling the resonance modes 'q-independent', in principle the frequency of the mode is indeed q-independent but the intensity is theoretically not. The reason why in the BLS measurements in this section the spectra are found to be independent from the angle is that obviously all qs $0 \le q \le q_{BS}$ contribute equally to the multiple scattering. In Sect. 4.2.4, an experiment is presented that shows the q-dependence of the scattering intensity of individual modes.

However, it was not settled whether selection rules apply for the BLS from particles with diameters comparable to the wavelength of the incident laser light ($qd \approx 1$). While Li et al. [26], based on group theory considerations, claim that only particle resonances with even ls contribute to BLS eigenmode spectra, according to Montagna [25] resonances with even and odd ls should have comparable activities. In fact, the latter is supported by a BLS study [8] of model PS spheres revealing up to 21 resonance modes theoretically captured with no adjustable parameter.

Moreover, utilizing a finite element method (FEM, cf. Sect. 3.4.4 in Chap. 3), I could validate the assignment for the first six modes with $n = 1$ and $l = 2$–7, which are shown as open squares in Fig. 4.2 in perfect agreement with the scattering cross-section calculations and the experimental frequencies. Figure 4.3 shows the FEM result for the lowest (1,2)-eigenmode of a PS sphere with $d = 540$ nm. Using the same parameters as in the cross-section calculations ($c_l = 2350$ ms^{-1}, $c_l = 1200$ ms^{-1}, $\varrho = 1050$ kg m^3) [8], the (1,2)-mode is found at 1.87 GHz, while the experimental mode was measured at 1.94 GHz. Figure 4.3a shows the deformed surface of the sphere, while subfigures b–d show the deformed intersecting planes in the planes of a Cartesian coordinate system. The color scale corresponds to the total local displacement. In the
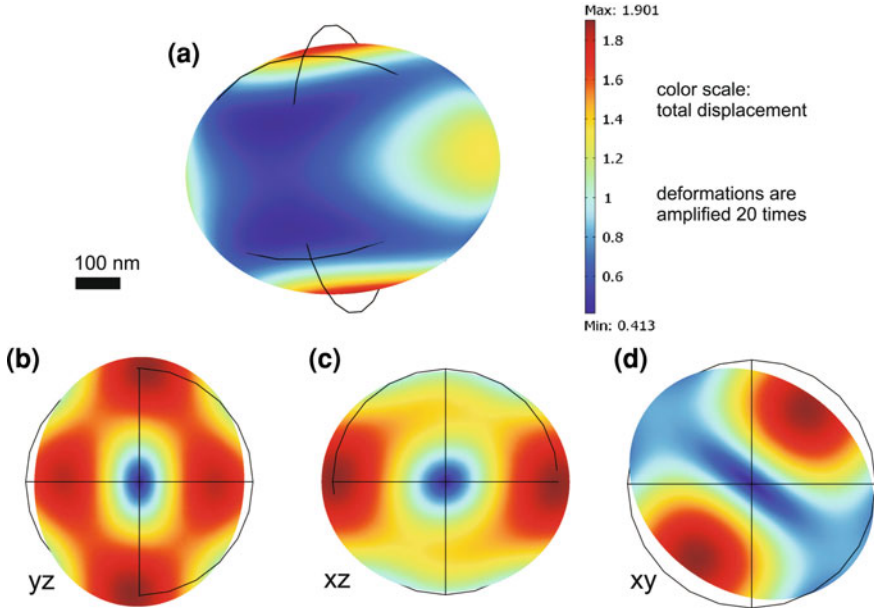
Fig. 4.3 FEM simultation for the (1,2)-eigenmode of a PS sphere with $d = 540$ nm at 1.87 GHz; **a** total displacement (color scale) and deformation of the surface, **b–d** displacement and deformation of intersecting planes in the three planes of a Cartesian coordinate system. Deformations are amplified by a factor of 20

intersecting planes, a displacement symmetric to the center of the spheres is visible, which is also the only knot of the displacement function, i.e., $n = 1$. The shape of the deformation, which is amplified by a factor of 20 in order to clarify the direction of the deformation, assigns the angular momentum quantum-number l; in each intersecting plane the deformated sphere has two maxima and two minima, i.e., $l = 2$. (Note: The thin black lines denote the undeformed sphere.) Analog to the identification of the (1,2)-mode, also the modes with higher l can be found from the FEM simulation. It is noteworthy that there are a higher number of modes calculated following the FEM approach than seen in the BLS experiment. However, most of these modes are torsional modes, i.e., the displacement is fully tangential. Such modes do not cause inelastic light scattering, only spheroidal modes, where the displacement is also (or fully) radial, contribute to the light scattering spectrum [23, 25, 26]. By choosing only the spheroidal modes out of the simulated eigenmodes, those with higher l are easily obtained from the FEM results. Checking the displacement and the deformation in the intersecting planes as in Fig. 4.3 allows the correct deter-mination of n and l. The shape of the surface for the modes with $n = 1$ and $l = 3$–7 is shown in Fig. 4.4 together with the intersecting planes for $l = 3$; for the higher l the intersecting planes look analog to those for $l = 2$ and $l = 3$ with l deformation maxima in each plane. Of course even higher order modes can be
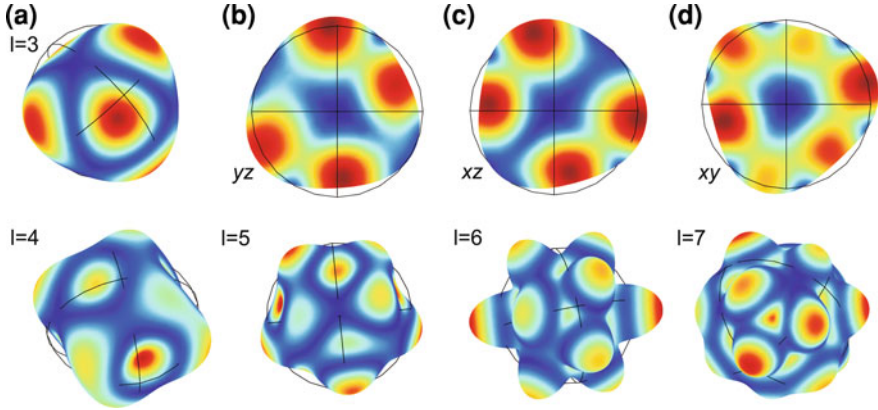
Fig. 4.4 FEM simulation for the higher l eigenmodes ($n = 1$). Deformations are amplified by a factor of 20. *Top* total displacement (color scale) and deformation of **a** the surface and **b–d** the intersecting planes of the (1,3) spheroidal mode. *Bottom* displacement and deformation of the surface for modes with $l = 4$–7. For a PS sphere with $d = 540$ nm the frequencies are found to be 2.79 (1,3), 3.58 (1,4), 4.32 (1,5), 5.03 (1,6), and 5.74 GHz (1,7) in good agreement with the experimental data (Fig. 4.2)

found by FEM, however, with increasing order the assignment becomes more and more complicated, since in the calculation mostly asymmetric mixed modes appear. Theoretically, with much finer mesh, all modes can be assigned clearly. Anyhow, even the six modes shown here (in perfect accordance with another calculation method) proof that there is no limitation on even ls as claimed by Li et al. [26], since the assignment of the (1,3) and the (1,5)-mode with no fitting parameter is clear and without any alternative. On the other hand, the FEM simulation of the eigenvibrations of silica spheres with $d = 360$ nm, whose eigenmode spectrum is shown in Ref. [26], allows other assignments for the first four modes than that chosen by the authors, who restricted themselves on even ls, utilizing the elastic parameters given by the same authors experimentally ($c_t = 2520$ ms^{-1}, $c_l = 3960$ ms^{-1}, $\varrho = 1960$ kg m^{-3}) [31]. The mode at 8.76 GHz [assigned as (1,0)] could be the (1,3)-mode (8.60 GHz by FEM), the mode claimed to be the (1,6)-mode at 14.4 GHz could be a double signal containing the modes (1,5) and (1,6), found by FEM to appear at 13.14 and 15.29 GHz, respectively. For higher orders, the assignment is more difficult, however, the mode at 17.65 GHz [claimed to be (2,4) or (3,2)] could be identified as the (1,7)-mode, calculated to appear at 17.4 GHz.

It should be noted that deviating from Ref. [24] in Fig. 4.2 also the breathing mode (1,0) is shown as a theoretical fit based on FEM calculations, again in perfect agreement with the scattering cross-section method [32]. It is found that for the case of PS spheres the (1,0)-mode is not far away from the (1,4). In fact, the third signal (from low to high frequency) for the PS spheres in Fig. 4.1 seems slightly broadened, which might be related to a weaker signal from the (1,0)-mode.

4.2.2 The Influence of the Neighbors: Mixtures

The assignment of the two phononic gaps is also corroborated by their sensitivity on the disorder. In this context, non-crystalline colloidal films were prepared by vertical lifting deposition of 'hybrids', binary mixtures consisting of an equal number of two PS spheres with different diameter ($d = 300$ and 360 nm). The size polydispersity is then artificially increased and no crystallization takes place, which is affirmed by SEM-pictures. The eigenmode acoustic spectra of these dry hybrid films and the dispersion relations in their infiltrated counterparts were measured by BLS. The eigenmode spectrum of the 1:1 300:360 nm hybrid is shown in Fig. 4.5 along with the eigenmode spectra of the individual one component opals. Interestingly, the spectrum of the hybrid is a superposition of the individual opals as is indicated by the vertical lines denoting some exemplary resonance frequencies either from the small or the big spheres. Moreover, hybrids of different relative ratios of the constituent spheres were prepared. The intensity of the signals originating from a particular particle size relates to its composition in the mixture. In Fig. 4.5, this linear composition dependence is demonstrated by superimposing the spectrum of the 1:1 300:360 nm hybrid with the spectrum of a 3:1 300:360 nm hybrid, normalized to the peak intensity in the 360 nm spheres. For clarity a baseline correction was introduced into the Stokes-side of the hybrids (inset to Fig. 4.5).
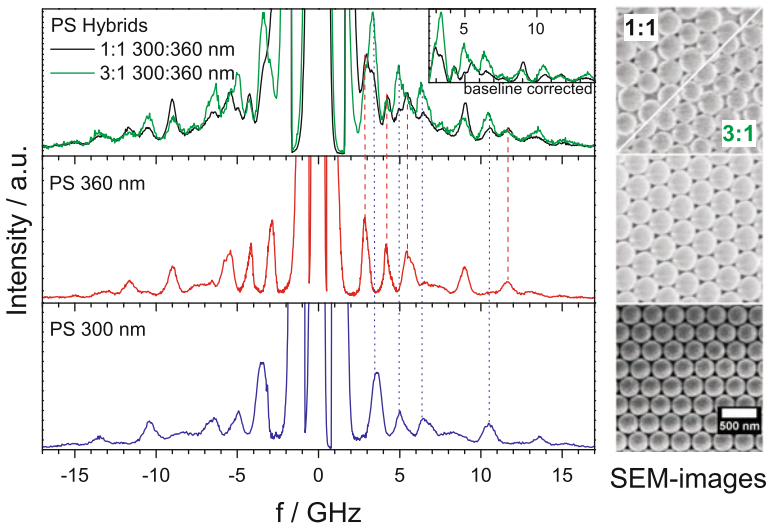
Fig. 4.5 *Left* eigenmode acoustic spectra of the PS opals with $d = 300$ nm (blue), $d = 360$ nm (red) and the symmetric PS hybrids 1:1/3:1 300:360 nm (*black/green*)(*bottom* to *top*). The vertical lines (dotted for $d = 300$ nm, dashed for $d = 360$ nm) denote some exemplary eigenmodes appearing in the opals and in the hybrids. In the *top right* corner the Stokes-sides of the hybrids' spectra are compared after baseline correction to better visualize the influence of the composition on the relative intensity of the individual signals. *Right* corresponding SEM-images of opals and hybrids shown on the left side [24]

Apparently, but somewhat counterintuitive, the contact between the spheres does not influence their eigenmodes—at least for non-infiltrated dry films. We also examined only partially ordered samples of monodisperse nanospheres prepared by dropping a few drops of the suspension of the spheres onto a glass substrate. In spite of the lack of any order, the eigenmode spectra of these samples are indistinguishable from those of the colloidal crystals. To undermine the contact argument, the consistency of the spectra's features would be based upon the small differences between the opals and the hybrids for 300 and 360 nm PS spheres, also very asymmetric hybrids with a nine to one number ratio of 180 and 550 nm PS beads were investigated. While for every dense packing of spheres, the number of neighboring spheres and hence the contact points as indicated by the SEM-images is 12, this mean number is different for the random packed hybrids depending on their size disparity and their number ratio. For example, in the SEM image for a 9:1 180:550 nm hybrid in Fig. 4.6, the number of next neighbors of the large spheres is increased dramatically by small beads that accumulated around the bigger spheres. However, even in this extreme case, the resonances from the 550 nm spheres are virtually unaltered as demonstrated in the spectra of Fig. 4.6. A careful inspection, however, of the two lowest frequencies reveals a very small shift of the hybrid resonance modes towards higher frequencies as is shown in the inset of Fig. 4.6 for the Stokes-sides of the spectra. Though the observed effect is subtle ($\sim 4\%$ frequency shift) but significant. In this context it is noteworthy to mention that in Fig. 4.3 of Ref. [33], Li et al. compare the BLS spectra from a 320 nm silica artificial opal and from a single sphere of the same kind, measured by a micro-Brillouin light scattering setup. In this figure it seems as if there is a shift between single spheres and opal. Interestingly, the authors describe only the broadening in the opal due to the polydispersity.
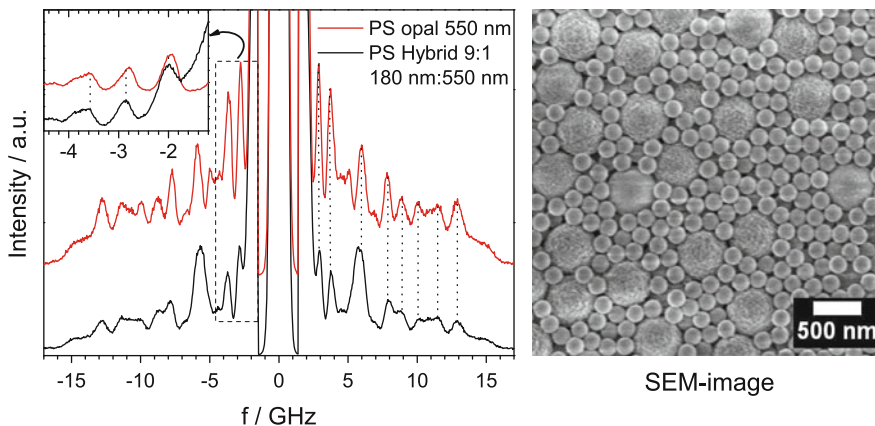
Fig. 4.6 *Left* comparison between the eigenmode acoustic spectra of the 550 nm PS single opal and the highly asymmetric 9:1 180:550 nm PS hybrid. *Right* SEM-image of the 9:1 180:550 nm PS hybrid [24]

In summary, the number of next neighbors does not influence significantly the eigenvibrations of the individual spheres. The effect of the disorder on the dispersion relation of our PS hybrids after infiltration is discussed in Sect. 5.1.3 (in Chap. 5).

4.2.3 The Influence of the Rigidity: Copolymers

While there are several BLS studies dealing with the size-dependence of the eigenmodes of homogeneous spheres from different materials (Sect. 4.2.1) [7, 8, 24], where the elastic properties are calculated from the experimental results, as well as two more elaborate studies on core–shell particles, presented also in this thesis (Sect. 4.3) [34, 35], a systematic experimental investigation of the influence of the particle rigidity on the eigenvibrations of mesoscopic copolymers is still missing. After Lamb (Eq. 2.106)

$$f(n, l) = \left(x(n, l)\sqrt{\frac{R(c_l, c_t)}{\varrho}} \right) \Big/ d,$$

with $x(n, l)$ being a temperature-independent constant for each individual mode and $R(c_l, c_t)$ being the rigidity, which is a function of longitudinal and transverse sound velocity c_l and c_t [21]. The frequencies can be theoretically obtained by single-phonon scattering cross section calculations (Sect. 3.4.1 in Chap. 3) or finite element modeling (Sect. 3.4.4 in Chap. 3). Here, BLS is utilized in a set of nearly uniformly sized ($d \approx 200$ nm) polymeric colloids consisting of poly(methyl methacrylate) (PMMA) copolymerized with poly(n-butyl acrylate) (PnBA) in different compositions in order to investigate the development of the elastic constants as a function of the copolymer composition. Therefore, bulk and individual colloidal properties are measured by BLS and consulted in combination to obtain insight into the effect of copolymerization on the mechanical characteristics in such small spheres. Due to the clearly differing rigidity of the homopolymers at room temperature, which is confirmed by the large difference in the glass transition temperature T_g [T_g(PMMA) ≈ 110 °C, T_g(PnBA) ≈ -43 °C], the softness of the copolymer increases rapidly with the amount of n-butyl acrylate used in the synthesis.

Copolymerization of two distinct monomers permits the combination of their individual properties and, hence, allows control over various physical quantities, such as T_g. Random radical copolymerizations of MMA and nBA was conducted by my colleague Retsch in order to tune the T_g of the resulting colloid. The composition of nBA in the copolymer was targeted to 10, 20, and 30 wt% through selection of the weight ratio of the two monomers in the initial emulsion. A random copolymerization is indicated by the Q and e values of both monomers in terms of the Q-e-schema of Alfrey and Price (nBA: $Q = 0.38$, $e = 0.85$; MMA: $Q = 0.78$, $e = 0.40$) [36, 37]. A homogeneous copolymerization is indicated by the

Fig. 4.7 DSC data for the four compositions at the second heating run, i.e., bulk properties. T_gs are denoted by vertical lines. The inset shows T_g as a function of the composition together with a Fox–Flory fit and a Gordon–Taylor fit from Ref. [38]
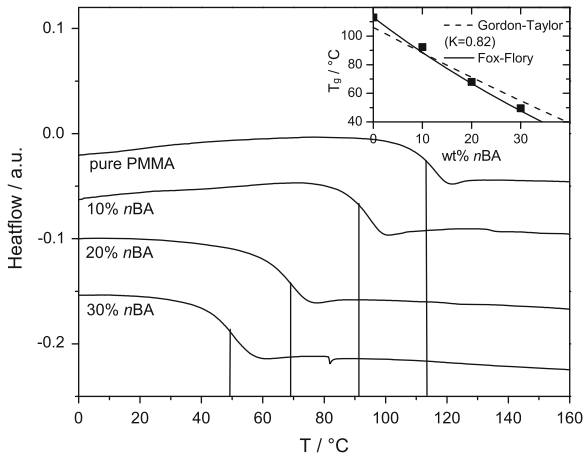
very similar r values (nBA: $r = 0.94$; MMA: $r = 0.91$) not very different from $r = 1$.

Differential scanning calorimetry (DSC) was used to determine the glass transition temperature T_g. The results of the heating period of the second run, i.e., after heating initially to 200 °C (and therefore bulk properties), are shown in Fig. 4.7. T_g decreases rapidly with increasing amount of nBA. Using the value measured for pure PMMA and the literature value for nBA (-43 °C) [38], allows an excellent representation of the glass transition temperature as a function of the composition by the Fox–Flory equation [39]

$$\frac{1}{T_g} = \frac{\phi_{\text{PMMA}}}{T_{g,\text{PMMA}}} + \frac{\phi_{\text{P}n\text{BA}}}{T_{g,\text{P}n\text{BA}}} \tag{4.1}$$

with no fit parameter (inset). The Gordon–Taylor fit also shown in the inset is borrowed from Ref. [38], including the empirical parameter K = 0.82, however, the small deviations originate partially in different values measured for pure PMMA. Our T_gs could be perfectly represented with T_g(PMMA) = 113 °C and K = 0.65. In addition to the single T_g, dielectric spectroscopy has been performed by my colleague Mpoukouvalas, which showed a single α-relaxation for each sample, i.e., both kind of segments feel the same energy landscape.

The density ϱ of the copolymers was determined by a density gradient column using aqueous calcium nitrate solutions [40]. The experimental results shown in Fig. 4.8 conform to a weight average density, using for the density of the homopolymers $\varrho_{\text{P}n\text{BA}} = 1.035 \, \text{g cm}^{-3}$ and $\varrho_{\text{PMMA}} = 1.195 \, \text{g cm}^{-3}$.

The size of the spheres is ascertained by scanning electron microscopy (SEM). The average molecular weight M_n and the polydispersity index PDI of the polymers were measured relative to PMMA standards by gel permeation chromatography (GPC). Crystallinity was excluded by small angle X-ray scattering measurements. The particle properties are itemized in Table 4.1.

Fig. 4.8 Determination of mass density as a function of the composition by a density gradient column for the two lightest samples. The squares are well-known calibration standards. The inset shows a fit for all four compositions
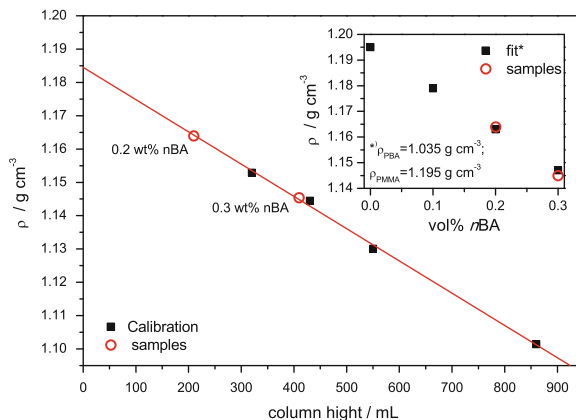
Table 4.1 Particle and material properties of the investigated spheres obtained by SEM (d), GPC (M_n, PDI), DSC (T_g) and density gradient column(ϱ)

nBA (wt%)	d (nm)	M_n (g mol^{-1})	PDI	T_g (°C)	ϱ (g cm^{-3})
0	232	92,500	4.2	113	1.195
10	214	89,500	4.2	92	1.179
20	200	84,200	3.2	68	1.163
30	204	110,000	3.5	50	1.147

By vertical lifting deposition [41] non-transparent films of the colloids with thickness of about 30–50 μm were prepared by Retsch. The BLS eigenmode spectra were recorded in transmission geometry at (non-arbitrative, due to strong multiple scattering) scattering angle of 50°. Figure 4.9 shows the experimental spectra. Because of the slightly differing particle diameters given in Table 4.1 and the d^{-1}-dependence of the modes given in Eq. 2.106 the frequency axis is normalized to the product of frequency and diameter. The eigenmodes correspond to the maxima of the spectra, all four spectra can be represented by five Lorentzian signals, denoted by the dotted vertical lines on the anti-Stokes side of the spectra. However, the fourth spectral line is much broader than the others.

Obviously, with increasing amount of nBA (bottom to top) the modes are shifted towards lower frequencies. This correlates with the decreasing rigidity in Eq. 2.106 caused by the softening in the copolymer. Notably, the change in the density alone (ca. 4%) would lead to a frequency shift in the opposite direction.

According to Eq. 2.106, the frequencies of the eigenmodes are functions of three parameters: c_l, c_t, and ϱ or, alternatively, Young's modulus E, Poisson's ratio σ, and ϱ. Since the mass density is experimentally known, the adjustable parameters are the two sound velocities.

For the bulk copolymers, BLS can, in principle, deliver c_l and c_t by recording the dispersion relations for polarized and depolarized light scattering, respectively. Transparent samples were prepared by heating some of the vertical lifted opals by a heat gun ($T \approx$ 100–200 °C) for a few seconds, which results in a melting of the

Fig. 4.9 Experimental BLS eigenmode spectra with frequency *f* normalized with the particle diameter *d*. The dotted vertical lines on the anti-Stokes side denote the positions of the five resolved maxima for the pure PMMA spheres [42]
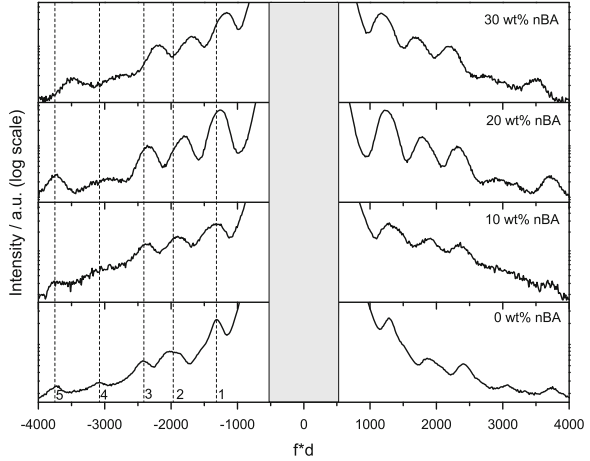
mesospheres. The polarized spectra delivered c_l, but the intensity of the theoretically accessible c_t in the depolarized spectra was not strong enough to determine a single signal. The measured c_ls are presented in Table 4.2, together with the value of a bulk PnBA sample.

Previous studies on homogeneous mesoscopic polymer and silica beads show that there should be no significant change in the longitudinal sound velocity that has to be taken into account in the colloids compared to that in the bulk material [8, 24, 31]. Since the rigidity R for the lower frequency eigenmodes is found to be a much stronger function of c_t, i.e., shear modulus $G = \varrho c_t^2$, than of c_l, i.e., longitudinal modulus $M = \varrho c_l^2$ (cf. Sect. 2.1.2 in Chap. 2), it is meaningful to take the bulk longitudinal sound velocities also as given in the description of the vibrational modes.

Table 4.2 shows the decrease of c_l, i.e., softening, in the copolymers with increasing amount of nBA. However, this decrease is small compared to the experimental value of c_l in the two homopolymers. In Sects. 5.1.2 and 5.2 in Chap. 5 of this thesis, several approaches to describe the sound propagation in an effective medium composed of (at least) two mechanically different materials are discussed. It turns out that the simple expression

Table 4.2 Experimental and theoretical bulk c_l for homopolymers and copolymers at room temperature

nBA (wt%)	c_l(BLS) (ms^{-1})	c_l(Wood) (ms^{-1})	c_l(Wood) (ms^{-1}) $c_{l,\mathrm{P}n\mathrm{BA}} = 2200$ ms^{-1}
0	2,755	2,755	2,755
10	2,678	2,569	2,663
20	2,615	2,421	2,584
30	2,498	2,300	2,515
100	1,835	1,835	2,200

$$\frac{1}{M_{\text{eff}}} = \frac{\phi_1}{M_1} + \frac{1 - \phi_1}{M_2}, \tag{4.2}$$

which is known as Wood's law [43], is in many cases a good approximation to give an effective modulus M_{eff} as a function of the components individual moduli and the composition. If one assumes Wood's law to be, in principle, a good approximation also for copolymers, the theoretically expected values for c_l can be easily calculated, as shown in the second column of Table 4.2. Obviously, the presented approximation strongly overestimates the softening due to the nBA in the copolymers, leading to a deviation of up to 8% for 30 wt% nBA. It will be shown in Sect. 4.3.1 that the mechanical moduli are temperature dependent, strongly decreasing at temperatures above T_g. At room temperature, all sound velocities except for bulk PnBA are measured in the glassy state, i.e., for purely elastic response. In contrast, bulk PnBA at room temperature is in the rubbery regime, i.e., it behaves viscoelastically and hence its c_l is lower than for a glassy PnBA. In other words, the nBA segments in the three glassy PMMA–r-PnBA copolymers assume a dense packing and therefore should display elastic response due to the very slow (essentially frozen) dynamics. The success of Eq. 4.2 in representing the experimental c_l values of the copolymers is optimized if a fictive $c_l = 2200 \text{ ms}^{-1}$ is used for the bulk PnBA, i.e., by introducing an 'effective glassy longitudinal sound velocity'. The third column in Table 4.2 shows the good representation by Wood's law, using this artificially increased value.

Returning to the eigenmode spectra in Fig. 4.9, the fixation of d, ϱ, and c_l to their experimental values reduces the number of adjustable parameters in the single phonon scattering calculations (Sect. 3.4.1 in Chap. 3) or FEM (Sect. 3.4.4 in Chap. 3) into one (c_t).

Scattering cross-section calculations were performed by my coworker Sainidou [29, 44]. Utilizing reasonable values for c_t, the first three modes could be clearly assigned as the (1,2), (1,3), and (1,4)-mode, in analogy to the results found in polystyrene and silica samples in Sect. 4.2.1. However, the fourth signal, which is much broader than the others, cannot be assigned to the expected (1,5)-mode, since it appears at higher frequencies. Indeed, its frequency is found between those of the (1,5) and the (1,6)-mode, indicating that the signal is a superposition of both modes. This explains also the broad appearance of the signal, although a fit with two Lorentzians does not converge. Therefore, instead of pretending a meaningful fit of two individual modes, one must be content to show the signal in between these two modes. The 'fifth' mode, on the other hand, can be assigned as the (1,7)-mode with acceptable accuracy, by choosing c_t given by the mean square fit of only the first three modes. In fact, for this last mode, the deviation from the theory decreases with increasing amount of nBA in the copolymer.

All experimental modes are shown in Fig. 4.10 together with the fitted values for fd, using c_t as the only floating parameter. The linear fits have no theoretical meaning, however, they follow the trend of most signals quite well, although the change between 0 and 10 wt% does not follow the linear trend for the first two modes. For the (1,7)-mode ('mode 5'), however, the change between 20 and

Fig. 4.10 *fd* against the amount of *n*BA in the copolymer individually for all four samples for each of the five observed signals and in the *bottom right* panel together for all signals together. The number of the mode corresponds to the number given in Fig. 4.9 next to the dotted vertical lines. The open blue circles belong to the theoretically obtained frequencies for the (1,*l*)-modes with *l* = 2–7 [full circles for the (1,6)-mode], denoted in the *top right* corners of each panel. The linear fits in red are guides for the eyes. Error bars are 2% [42]
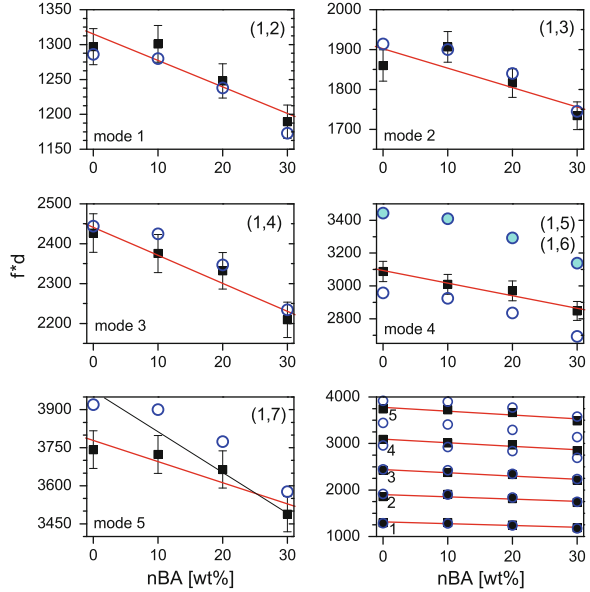
30 wt% is quite large regarding the virtually unaltered *fd*-values between pure PMMA and 20 wt% *n*BA. Correspondingly, the relative deviation between experiment and theory is largest (≈4%) for the (1,7)-mode and pure PMMA. On the other hand, a linear fit through only the 20 and 30 wt% points captures the calculated points with a deviation <2%.

From the experimentally obtained material parameters, in combination with the fitted values for c_t, it is possible to calculate the elastic moduli of the mesospheres and by that to quantify their softening due to the addition of *n*BA. The calculated values for the elastic moduli as well as for Poisson's ratio can be found in Table 4.3.

As expected, all moduli go down with increasing amount of *n*BA, indicating the strong softening effect (by ≈20% between pure PMMA and the softest copolymer). The more striking feature is the constance of Poisson's ratio σ. In a copolymer with increasing amount of a rubber-forming monomer (and consequently strongly decreasing T_g), one could expect a more rubber-like behavior of the copolymer, i.e., an increasing σ. At room temperature, i.e., about 30 °C below the lowest T_g, however, this is not the case. This finding means that the compressibility

Table 4.3 Fitted c_t, elastic moduli (Young's, longitudinal, and shear modulus), and Poisson's ratio

nBA (wt%)	c_t (ms^{-1})	E (GPa)	M (GPa)	G (GPa)	σ
0	1,530	7.14	9.07	2.80	0.277
10	1,520	6.88	8.46	2.72	0.262
20	1,466	6.35	7.95	2.50	0.271
30	1,394	5.68	7.15	2.23	0.274

characteristics at room temperature are virtually unaffected by the softening, there is no shift towards rubber-like behavior below T_g. In turn, this result corroborates the 'trick' applied in the beginning of this section, when introducing the effective glassy sound velocity for PnBA at room temperature to fit Wood's law.

In summary, this section contains a systematic study on the softening of mesoscopic PMMA spheres by copolymerization with nBA with the help of BLS bulk and eigenmode measurements. The elastic moduli are quantified. The Poisson effect is virtually unaffected by the softening. This is described by an 'effective glassy sound velocity' of the homopolymer PnBA at a temperature at which pure PnBA is a rubber.

4.2.4 The Influence of the Wave Vector: Suspensions

In Sect. 4.2.1, I pointed out that, theoretically, the scattering intensity of the individual modes should be strongly q-dependent, however, due to the strong multiple scattering all qs corresponding to values between zero and backscattering contribute equally to the spectrum and hence the intensity distribution is the same independent from the scattering angle θ. Based on symmetry arguments, Montagna showed that for a given n the BLS intensity of modes with increasing l are only active for increasing values of qd [25]. In fact, for a given system, the intensity maximum of each mode (n, l) should appear at a different q, i.e., for a transparent system that allows the observation of eigenmodes at different scattering angles θ, while the angle of maximum intensity θ_{max} increases with l.

It was shown first in 2003 by Penciu that BLS can be used to measure the eigenmodes of silica colloids suspensions in a refractive index matching liquid (cyclohexane/decalin) [29, 45]. By measuring the suspension in an NMR-tube the sample can be regarded as quite thick, which allows to see also eigenmodes that are not resolved anymore in the systems presented in Chap. 5. It is shown that the appearance of the eigenmodes depends on the filling fraction of the silica spheres in the suspension. In fact, quite high filling fraction are needed to resolve the eigenmodes at all. Those have been achieved by centrifugation of the suspension at the bottom of the NMR-tube. The graphs in Fig. 7 of Ref. [29] show the resolved modes as a function of qd for two different silica particles with diameter $d = 328$ nm and 250 nm, respectively, at three different filling fractions ($\phi = 0.3$, 0.62, and 0.67). For all systems, an effective medium acoustic branch is observed that will not be further regarded in this section. Besides that, there are up to four modes that appear at the same frequency for each qd, resonance modes of the silica spheres. While at $\phi = 0.3$ only one such mode is found, in the polycrystalline or glassy samples with significantly higher ϕ more modes can be distinguished.

Although in Ref. [29] some exemplary spectra at different qd give evidence that the q-dependence of the BLS intensity can be shown by these samples, a systematic investigation is still missing. Therefore, in this section the results of BLS measurements on silica particles with $d = 375$ nm in an index matching matrix of

liquid ethoxy-ethoxyethyl acrylate (SR256) are presented in order to bridge this
gap of knowledge. The sample was synthesized by my coworker Kiefer at DKI,
Darmstadt, with an initial filling fraction $\phi = 0.35$. The dispersion relation for this
filling fraction is presented in Sect. 5.4.1 (in Chap. 5). Here, I will focus on the
polycrystalline sample that was obtained from the dispersion by centrifugation for
90 min at 4000 rpm ($\phi \approx 0.70$–0.74).

Figure 4.11 shows BLS spectra taken from the polycrystalline sample at seven
different angles ($3.3 \leq qd \leq 11.6$) for two different free spectral ranges. The
eigenmodes are marked by vertical lines, the dispersion relation is shown in
Fig. 4.12. While for the two lowest eigenmodes the deviation from the mean varies
by about ± 1 GHz, the distribution of frequencies for the other resonance modes is
very narrow.

Fig. 4.11 Exemplary BLS spectra of polycrystalline silica colloids ($d = 375$ nm) in SR256 for seven different scattering angles, corresponding to $3.3 \leq qd \leq 11.6$, at two different free spectral ranges (**a** 40 GHz, **b** 15 GHz). The vertical lines denote the approximate frequencies of the eigenmodes
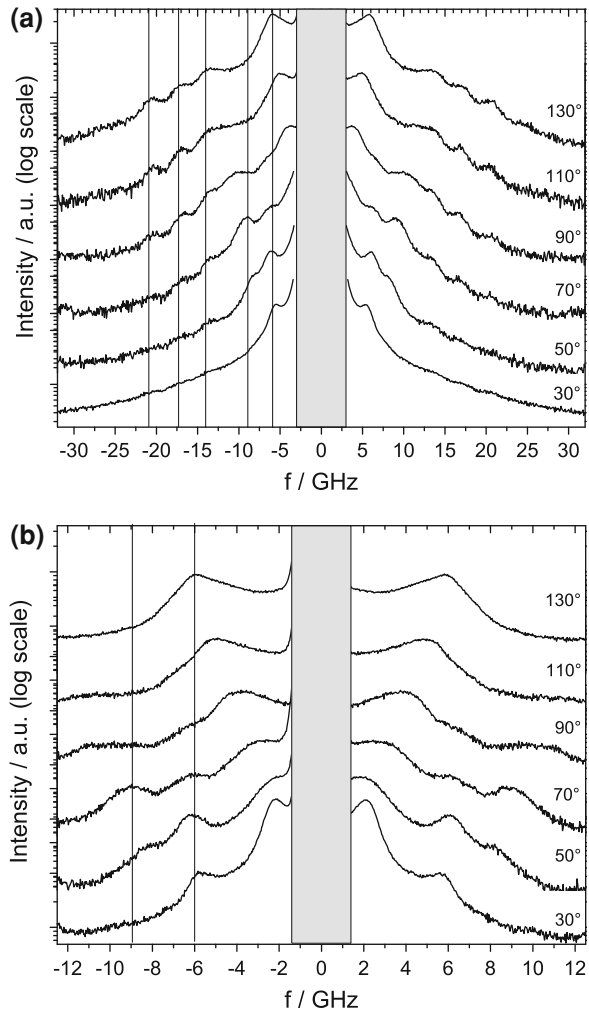
Fig. 4.12 Eigenmode frequencies as a function of qd extracted from the spectra in Fig. 4.11. The dashed lines represent the mean frequency for each eigenmode. The solid line shows a linear fit of the longitudinal acoustic branch (open circles) (cf. Sect. 5.4.1 in Chap. 5)
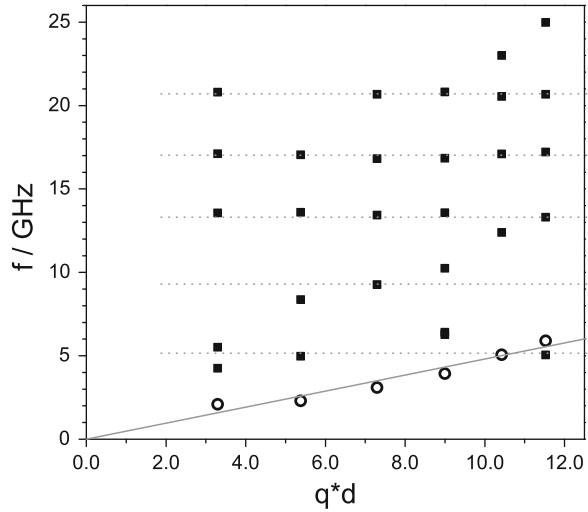
Though, when carrying out a more detailed investigation of the spectra in Fig. 4.11, it becomes clear that the relative intensities of the individual resonances vary systematically with the scattering angle θ. While the lowest frequency eigenmode around 5 GHz is strongest at low θ, the highest frequency modes appear strongest at high angles, qualitatively conforming the theoretical predictions [25]. The lowest mode is strong at $\theta = 30°$ ($qd = 3.3$), weak at $90°$ ($qd = 9.0$) and nearly disappears at $110°$ ($qd = 10.4$). The second mode around 9 GHz only appears between $50°$ and $90°$, while it is invisible at lower and higher qd. Also the higher frequency modes could be only foreboded in the spectrum at $30°$. At $50°$ and $70°$ the third and fourth mode start to appear weakly, the fifth mode quite feeblish at $70°$. Especially for the fourth and fifth mode, intensity increases clearly up to $110°$, while the difference between $110°$ and $130°$ is only small.

Although a full theoretical description of the q-dependence is missing for the present system, the qualitative agreement of the experiment with the predictions is a striking hint of their correctness.

4.3 Elastic Vibrations in Nanostructured Colloids

4.3.1 The Influence of the Temperature: PS–SiO$_2$ Core–Shell Particles

Core–shell particles exhibit properties that may be substantially different from those of the templated core. These include their density, mechanical stability, and optical characteristics. Proper design of core and shell material provides the

possibility to optimize the properties of core–shell particles according to their applications, thus making them attractive from both a scientific and a technological point of view. Silica shells are desirable because of excellent biocompatibility and easily tunable surface functionality [46, 47]. Furthermore, silica shells are much stiffer compared to most organic shells [48, 49]. Here the rigidity of thin glassy silica shells is utilized for the realization of shape persistent polymer cores at temperatures well above the polymer glass transition temperature T_g.

In this section BLS is employed to investigate the shape-persistence of spherical core–shell colloids consisting of a soft polystyrene (PS) core with $d = 400 \pm 12$ nm and a hard silica (SiO_2) nanoshell with thickness $L = 37 \pm 3$ nm against heating; this size was determined by scanning electron microscopy, averaging over about 100 spheres. The synthesis of the core–shell particles by soap-free emulsion polymerization of the PS core (slightly copolymerized with divinylbenzene) and subsequent coating by silica is described elsewhere [49]. Here, it is shown that a relatively thin SiO_2 shell acts as a 'nano-armor' of the polymer core even in the molten state above its glass transition temperature while the particles retaining remarkably high mechanical strength.

Herein, the strong localization of the vibration modes in core–shell particles with high elastic contrast is utilized to demonstrate the shape robustness of polymer based colloidal particles upon heating well within the fluid phase of the core. Both sound velocities (c_l, c_t) are sensitive index of T_g [50–53], due to the rapid increase of compressibility (C_{11}^{-1}) and decrease of shear rigidity (C_{44}). Hence, tracking the frequency of a distinct vibration mode (Eq. 2.106) with increasing temperature senses the decrease of the mechanical strength and marks the glass transition in the $f-T$ diagram if the particle shape is preserved. Thus, BLS measures single sphere mechanical properties.

For the BLS experiment, an opaque dry film of randomly packed PS–SiO_2 with a total thickness of several tens of microns was used [24]. Figure 4.13 shows high resolution BLS eigenmode spectra of the PS–SiO_2 and the parent plain PS spheres ($d = 400$ nm) recorded at room temperature. Both spectra exhibit several clearly distinguishable modes, with the lowest frequency mode being the strongest spectral line. The comparison of the line shapes of the two spectra shows that the spectrum of the core–shell particle is very akin to that of the bare PS spheres. The low frequency eigenmodes are therefore core-like, i.e., the signals are related to vibrations localized in the PS core. In the inverted case of core–shell particle with hard silica core and soft polymer shell only shell-like modes were identified [34]. Both cases can be explained by the fact that the BLS signal increases with the compressibility of the medium in which the elastic energy of the mode is localized, i.e., the scattering from a hybrid particle structure is dominated by the contribution of the soft component.

To verify that the softening of the core is monitored while the shape of the particle remains unaltered, I followed the T-dependent eigenmode spectra, focusing on the first (and strongest) signal of the core–shell particles (arrow in Fig. 4.13). This is assigned to the (1,2)-mode by comparison with the resonance modes of the computed DOS spectra as reported for soft (PS, PMMA) and hard

Fig. 4.13 Eigenmode spectra of the uncoated $d = 400$ nm PS spheres (*black*, *top*) and of the PS–SiO$_2$ core–shell particles (*grey*, *bottom*) at room temperature. The (1,2)-mode (arrow) is the strongest [35]
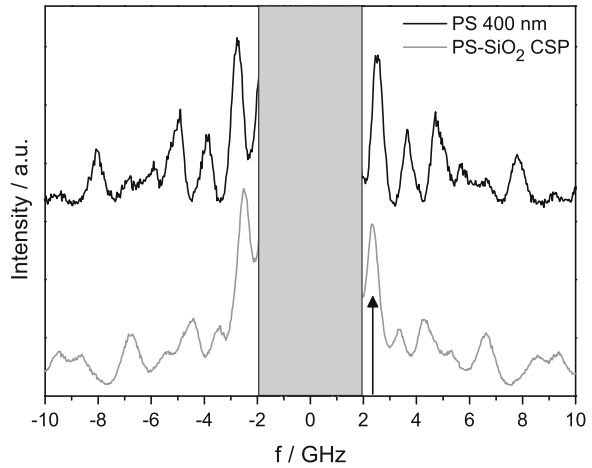
(silica) spheres [7, 8, 24]. Due to the small expansion coefficient of fused silica (5.5×10^{-7} K^{-1}), the diameter d in Eq. 2.106 is virtually temperature independent.

The heating experiment was performed at a non-arbitrative scattering angle of $50°$ while the sample was encased in a glass windowed oven (cf. Fig. 2(b) in Ref. [51]). The sample was heated from room temperature to 165 °C in steps between 30 (low T) and 10 K (high T) within a few minutes for each step. After equilibrating the sample for 15 min at each temperature, the eigenmode spectrum was recorded for about 15 min probing always the same spot (~ 50 μm). This ensures that even the intensities of the main modes can be traced as a function of temperature. Figure 4.14a shows eigenmode spectra at different temperatures upon heating and after cooling over a narrower frequency range than in Fig. 4.13, in order to further boost the resolution. All recorded spectra have been represented in the range of the (1,2)-signal by a Lorentzian using its frequency, line width, and amplitude as adjustable parameters. The (1,2)-mode is red shifted by ≈ 0.2 GHz at 165 °C relative to its frequency at room temperature either before (bottom) or after (top) heating, indicating a small decrease of shear modulus (C_{44}). Note that the same mode undergoes a much smaller shift at 70 °C.

The experimental frequencies $f(1,2)$ shown as a function of temperature in Fig. 4.15 are well represented by two distinct straight lines, expectedly both lines with negative slopes due to decreasing rigidity. The characteristic kink in the $f-T$ diagram signifying the transformation of a glassy into a rubbery state occurs at 107 ± 3 °C, which is slightly higher than the T$_g$ of bulk amorphous PS (100 °C) due to the crosslinking of the PS core with divinylbenzene (DVB) [54]. The presence of a single T$_g$ in Fig. 4.15 indicates a homogeneous, over few hundreds nanometers, core environment and hence this value of T$_g$ is further confirmed by differential scanning calorimetry (DSC) measurements on the bare PS cores and the PS–SiO$_2$ particles. In both systems T$_g$ was found to amount to 107.5 ± 3 °C, whereas in the absence of crosslinking T$_g$ lowers to ≈ 100 °C (see Fig. 4.15b), in
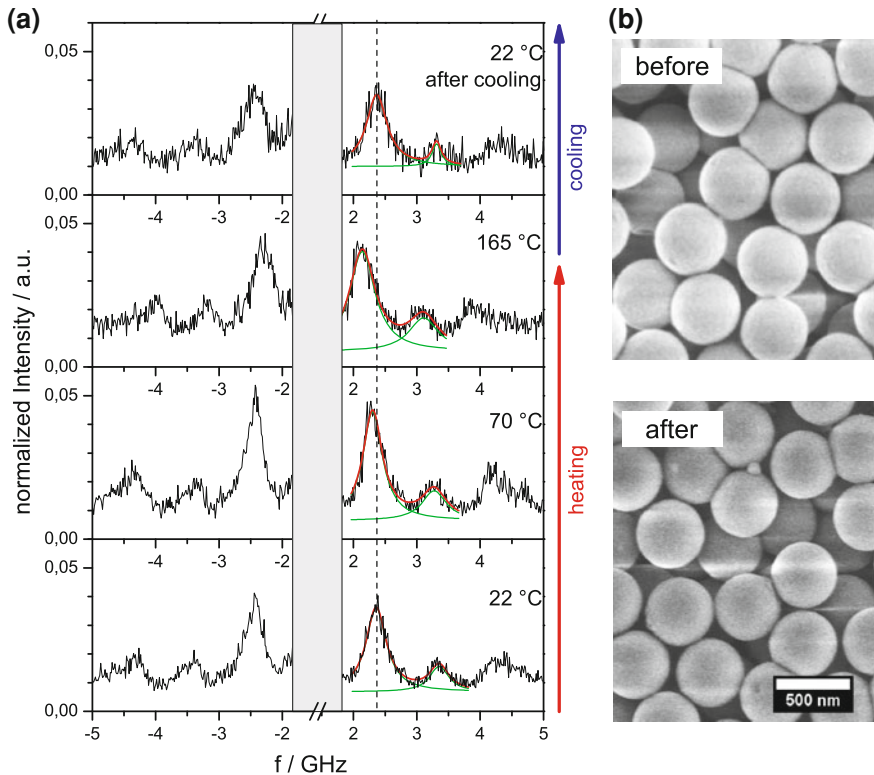
Fig. 4.14 a Exemplary eigenmode spectra during heating and after cooling (side arrows). The solid lines in the Stokes side of the spectra indicate the representation of the two low frequency modes by Lorentzian spectral lines (individual modes and sum). The dashed line indicates the position of the (1,2)-mode at room temperature. **b** SEM pictures of the core–shell particles before and after heating to 165 °C and cooling back to room temperature [35]

agreement with DSC. The clear detection of the glass transition affirms the validity of the obtained findings.

The relative drop of $f(1,2)$ between room temperature and T_g is less than 2% in the PS–SiO$_2$ particles and more than 6% in the bare PS cores (cf. Fig. 4.16). In the rubbery state of the core, $f(1,2)$ at the highest examined temperature (165 °C) is decreased relatively to its value at T_g only by about 6%. Assuming a constant density, this $f(1,2)$ value corresponds to a shear modulus $c_{44} \approx 1.45$ GPa in the confined polymer melt at about $T_g + 60$ K. For comparison, a corresponding decrease in the transverse sound velocity of PS films is about 40% (i.e., $c_{44} < 1$ GPa) [51]. This remarkable small temperature effect on the rigidity of the present three-dimensionally confined PS–SiO$_2$ particles as a result of the increased pressure in the core is unprecedented.

Even at temperatures far above T_g, the spectra (Fig. 4.14a at 165 °C) still possess the typical shape for $T < T_g$ with minor changes in the intensity. This
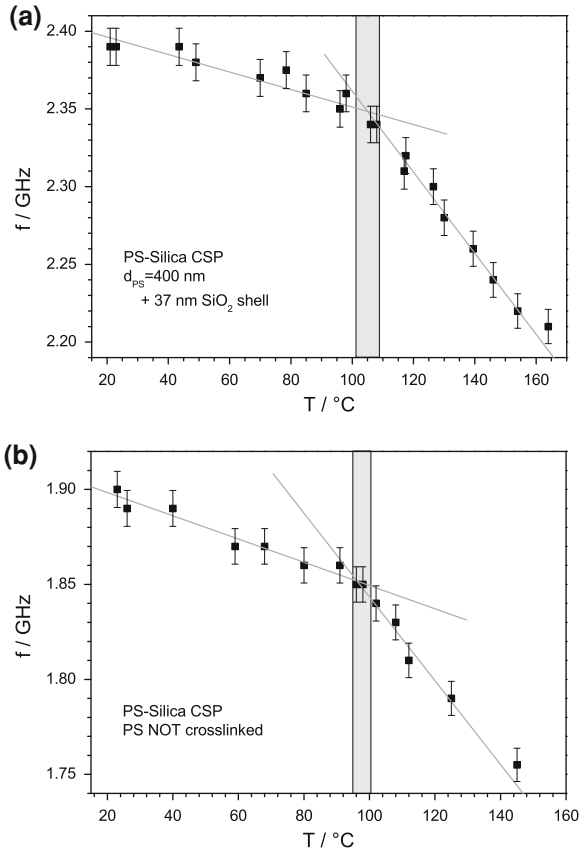
proofs that even in the rubbery regime the PS core keeps its spherical shape. The thermal expansion of the PS core is expected to increase by more than a factor two above T_g and hence the pressure on the silica shell [55]. Especially at temperatures well above T_g, it is this pressure that could, in principle, break the shell. However, when heating up to 165 °C, the intensity of the observed mode changes only very little within the experimental error. After cooling back to room temperature, not only the frequency (dashed line in Fig. 4.14) but also the intensity and the line-width (≈ 0.39 GHz full width half maximum) assume their initial values before heating. Thus the thin silica shell can stand the higher pressure under these conditions and prevents the PS core to change its shape. This notion is corroborated by the scanning electron microscope (SEM) photographs of the core–shell particles before and after the heating cycle to 165 °C shown in Fig. 4.14b. The lack of visible defects after the heating procedure confirms the results obtained by the BLS. Actually, the silica shell acts as an armor for the PS core.

In Fig. 4.16, the corresponding BLS experiment on bare PS particles is presented. These eigenmode spectra are very sensitive to the particle shape. For the bare PS particles $f(1,2)$ displays stronger decrease with temperature than for the

Fig. 4.16 Eight exemplary spectra for BLS eigenmode measurements on the bare $d = 400$ nm PS particles as a function of temperature: the two lowest resonances are fitted by Lorentzians. The dotted line denotes the center of the lowest eigenmode at room temperature. Measurements above 105 °C are performed with a new sample (ns) rapidly heated to these temperatures. The *inset* in the *top left* shows the f–T diagram for $T \leq T_g$ in analogy to Fig. 4.15 [35]
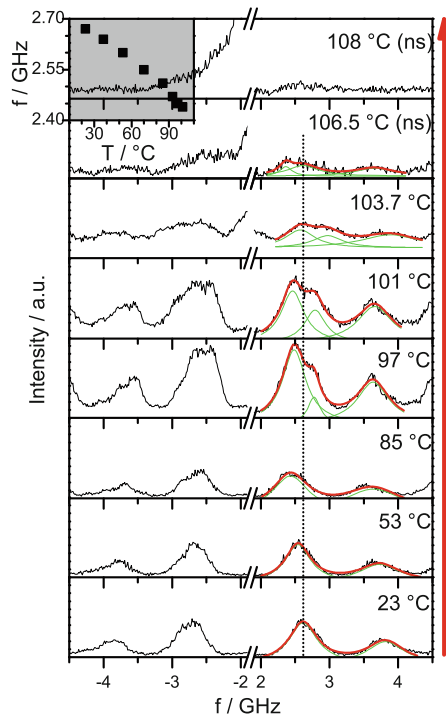
PS–SiO$_2$ core–shell particles (inset to Fig. 4.16) due to the absence of the confinementand partially to the now unsuppressed expansion of the PS spheres, i.e., decrease of c_{44} and increase of d in Eq. 2.106. Already below T_g the line shape of the (1,2)-mode changes and above T_g the signal vanishes completely within a few minutes. Starting at room temperature, for increasing temperature a shift to lower frequencies and a broadening/splitting of the signal is observed. The spectral shape of the (1,2)-mode (around 2.5 GHz) in the BLS spectra of the bare PS core in Fig. 4.16 severely changes as the temperature increases towards T_g. At temperatures above 85 °C, the single Lorentzian shape initially splits into two through the appearance of a second peak at the high frequency side. Finally, above 103 °C the intensity decreases rapidly and eventually vanishes at 108 °C within a few minutes. Apparently, shape alterations start already below T_g because of surface melting and breaking the particles spherical symmetry. With the onward and patchy destruction of the spherical shape, the resonance modes of the unarmed PS particles finally disappear, and the destruction of the spheres is, of course, irreversible. SEM pictures show only an undefined surface. Probing the shape of the PS mesospheres on the average during the melting process is another interesting but demanding task. In the context of the present study, it would require finite element modelling of all eigenfrequencies supported by a temperature dependent SEM or atomic force microscopy.

In summary, the morphological and thermo-mechanical response to heating of PS–SiO$_2$ core–shell particles at submicrometer length scales is probed by BLS that delivers quasi *in situ* insight into the individual colloids. By monitoring the eigenmode spectra, it was shown that silica shells of a few tens of nanometers protect a polymer core from changing its spherical shape even at temperatures well above T$_g$, which can be determined from the same experiment. The shape persistence of these hybrid systems is accompanied by a remarkable enhanced rigidity of the confined core above its T$_g$. The inevitable change of the amorphous packing inside the rigid nanocontainers will likely prove useful for fundamental studies.

4.3.2 The Influence of the Components: SiO$_2$–PMMA Core–Shell Particles

Colloid science can create novel materials that possess spatial variation of density and elastic constants at the nanoscale but their mechanical characterization remains difficult. Similarly, the influence of the particle architecture (core–shell spheres or hollow capsules), size, and shape on the eigenfrequencies, and the localization of elastic energy in specific regions of an individual particle is not known. In addition to the characterization on the nanomechanical properties, tailored acoustic confinement will be important for precise phonon management by structural engineering.

In this section, BLS is employed for the first measurement of the resonant modes (the 'music') in sub-micron core–shell spheres [silica-poly(methyl methacrylate)—SiO$_2$–PMMA] having constant core radius and varying shell thickness and in the corresponding spherical PMMA hollow nanoshells after dissolving the silica core. We observed up to nine particle vibrational frequencies with increasing size of the core–shell spheres and revealed the strong impact of the empty core of the hollow capsules on the size dependence of the resonance frequencies. The observed vibration eigenfrequencies are identified by detailed and thorough numerical calculations as the resonance eigenmodes of the individual spheres. The good overall agreement with the experiment allowed to determine the core density and the two elastic constants of both constituents in the hybrid particles. We found a significant deviation of these material properties in the nanostructured hybrid spheres from their values in the macroscopic bulk systems, which underlines the importance of such measurements at the nanoscale. The simulation of the displacement fields of the different elastic modes allowed to visualize their localization in different regions of the hybrid particles and provides a deeper insight into their origin. These first findings illustrate qualitatively general features of the localization of the elastic energy in nanostructured colloids beyond core–shell particles.

The SiO$_2$–PMMA particles with rigid silica cores and softer PMMA shells were prepared by my coworker Dr. Spahn (DKI, Darmstad) in a two-step process starting with the Stöber synthesis of the core followed by emulsion polymerization

of the shell [56]. The silica core, with a diameter of 181 ± 3 nm, was coated with PMMA spherical shells of three different thicknesses (in average 25, 57, and 112 nm), leading to core–shell particles of final (outer) diameter ranging from $d = 232$–405 nm. All samples were characterized by scanning electron microscopy (SEM), using a 1530 Gemini SEM by LEO with acceleration voltages setup between 0.2 and 1.0 kV. Figure 4.17a shows exemplary details for the uncoated silica cores and the three core–shell particles. Although there is some degeneration of the PMMA by the electron beam at 1 kV or some blurring using lower voltage (200 V), the particles' diameters d can be determined by averaging the software-aided gauged diameters over about 100 spheres for each sample. The size polydispersity is about 5%, which is confirmed by the formation of crystalline films (Fig. 4.17a) after vertical lifting deposition from the particle suspensions (cf. Sect. 3.1 in Chap. 3) [57]. Figure 4.17b shows SEM images of the spherical hollow capsules with $d = 232$ and 294 nm. After dissolution of the silica core with aqueous hydrofluoric acid, the diameters are found to be unchanged within the experimental error. For the smaller hollow capsules (bottom left) a considerable fraction (approximately 50%) of the particles possess holes, while the 294 (top right) and the 405 nm (not shown) hollow shells are nearly defect free due to their thicker shells. Notably these defects in the 232 nm hollow capsules lead to a broadening of the spectral lines, but do not significantly change their peak positions in the BLS spectra (see Fig. 4.20a below). The sizes obtained from the SEM were confirmed by the hydrodynamic radii, R_h, of the core–shell particles in dilute suspension measured by photon correlation spectroscopy (Sect. 3.3.1 in Chap. 3). Within 3%, R_h amounts to 214 nm for bare silica and 262, 352 and 504 nm, respectively, for the three core–shell particles. These values are expectedly higher than the geometric radii R measured by SEM since for homogeneous spheres the ratio R/R_h assumes the value of 0.78 [58]. Experimentally, R/R_h is found to be slightly higher, varying between 0.80 and 0.85. For the BLS experiment, films of all seven particles were prepared on a thin glass substrate using the vertical lifting technique [4].
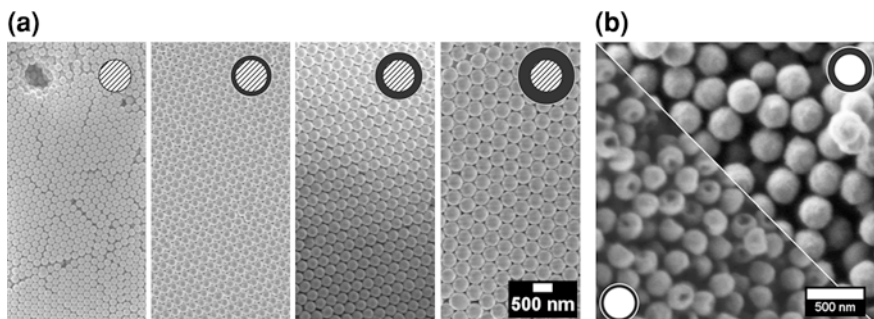
Fig. 4.17 SEM-images of **a** the bare silica (*left*, $d = 181$ nm) and silica–PMMA core–shell particles (from right: $d = 405$, 294 and 232 nm), and **b** the hollow PMMA capsules (*bottom left*: $d = 232$ nm, *top right*: $d = 294$ nm). For the smaller particles in **b**, holes in the spheres are observed, whereas there are nearly no defects in the thicker shells [34]

In analogy to the experiments in the previous sections, Fig. 4.18a shows the **q**-independent BLS spectra of the bare silica particles and the three core–shell particles. The spectra can be well represented by up to nine Lorentzian line shapes as shown by the solid lines on the Stokes side of the BLS spectra. The peak position of the spectral lines yields the resonance frequencies of the eigenmodes indicated by solid circles in Fig. 4.18b–e for the four particles. Advantageously, BLS can, in principle, record all thermally excited modes within one measurement, which is not possible, e.g., in the pump-probe technique. For the bare silica spheres, only two resonance frequencies at about 13 and 19 GHz can be resolved. However, with increasing the PMMA-shell thickness of the core–shell particles ($d = 232$, 294 and 405 nm), the BLS spectra become richer as it was observed for pure polystyrene colloidal particles [8]. For the particle with the thinnest shell a third weak peak is discernible in the spectrum in the inset of Fig. 4.18c, whereas five modes are observed in medium-thickness shell (Fig. 4.18d), and even nine modes are resolved in the BLS spectrum of the thickest shell (Fig. 4.18e). The increased number of the resolved modes in the BLS with increasing particle size relates to the intensity of the resonance signals which depends on qd. In the present case of strong multiple scattering $q \leq 2k_i$ (the backscattering vector),
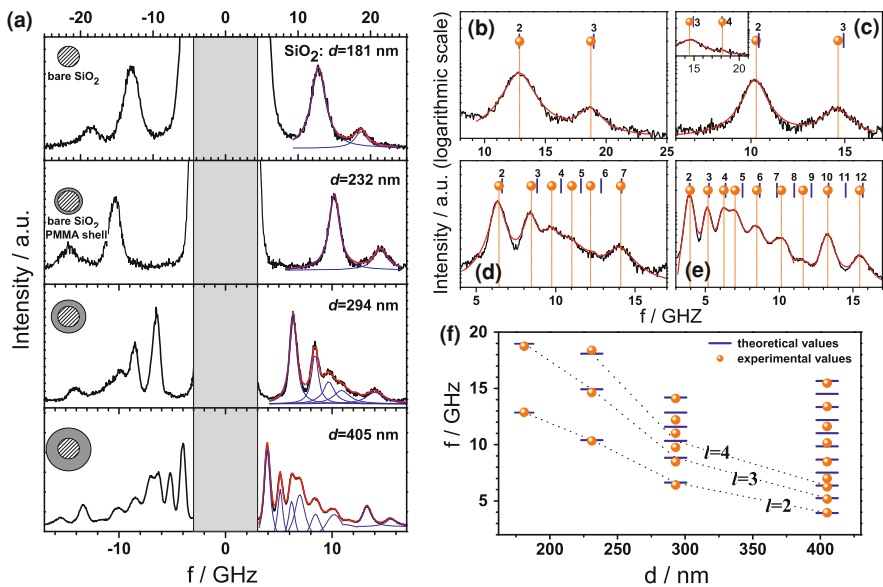
Fig. 4.18 a BLS eigenmode spectra of bare silica (*top*) and the three core–shell particle films. The representation of the BLS spectra with up to nine Lorentzians (*solid lines*) is shown on the Stokes-side. (Note the different frequency scale for the spectrum in the *top*.) **b–e** Enlarged Stokes-sides of the spectra from **a** (**b** pure silica, **c–e** core–shell). The experimental frequencies are accented by orange spheres, the small vertical lines denote the corresponding calculated resonance frequencies, each of them characterized by its angular momentum, *l*, shown at the top of the lines. All experimental and theoretical (*solid bars*) values are summarized in **f**, with the dotted lines connecting modes of the same angular momentum *l*; $n = 1$ for all observed modes [34]

and the number of resolved modes increases with the $2k_i d$ as discussed in Sect. 4.2.1 [25].

The elastic parameters (longitudinal and transverse velocities, c_l and c_t) of the two constituents (core- and shell-materials) are not a priori known for such nanostructured systems. An access to these material properties at these length scales and high frequencies is important since they can considerably differ from their values in macroscopic systems. The elastic constants are frequency dependent, and BLS specifically yields their limiting high frequency values, which relate to local packing and interactions, as well as, the glass transition temperature [51]. The detection of more than two particle elastic excitations in the experimental (BLS) spectra of Fig. 4.18 allows for an unambiguous determination of the elastic moduli, shear modulus $G = \varrho c_t^2$ and Young modulus $E = \varrho c_l^2 (1 + \sigma)(1 - 2\sigma)/(1 - \sigma)$, with $\sigma = (c_l^2 - 2c_t^2)/[2(c_l^2 - c_t^2)]$ being the Poisson ratio and ϱ being the mass density. The experimental values of the resonance frequencies are compared with the resonance frequencies obtained from the calculated density of states (DOS) spectra of a single constituent sphere of the experimental systems. The theoretical computations were performed by Dr. Sainidou (University of le Havre) using a formalism, appropriately developed for this case and presented elsewhere [28, 59]. Each resonance mode appearing at frequency $f(n, l)$ in these DOS spectra is characterized by the angular momentum l, imposed by the spherical symmetry of the particle, where n denotes the n-th order solution for a given l. All the shell-localized modes reported in this section have $n = 1$. The materials elastic parameters (c_l, c_t) and densities are used as adjustable parameters in order to achieve the least deviation between theoretical and experimental eigenfrequencies. Obviously, in the theoretical calculations the constituent spheres are considered as homogeneous and isotropic, and their elastic coefficients are frequency-independent.

First, the bare silica particles are considered (Fig. 4.18b). The two sound velocities treated as adjustable parameters are obtained from representation of the two experimental frequencies (solid circles) by the calculated resonance frequencies (small vertical lines in Fig. 4.18b). The obtained sound velocities for the bare-silica particles, $c_l = 4420$ ms^{-1} and $c_t = 2780$ ms^{-1}, are significantly lower ($\approx 25\%$) than the values of dense bulk amorphous silica ($c_l = 5970$ ms^{-1}, $c_t = 3760$ ms^{-1}, $\varrho = 2200$ kg m^{-3}), indicating the presence of porosity in these particles [31]. It also underlines the necessity of the BLS experiment to determine these values avoiding erroneous assumptions. The mass density does not sensitively affect the DOS spectra, due to the huge impedance difference between silica and air. Nevertheless, these porous silica spheres should be less dense than bulk silica (see below).

Next, the PMMA coated silica particles consisting of same silica cores are considered. For a first description of the DOS spectra, representing the experimental frequencies seen in the BLS spectra of Fig. 4.18c–e (solid circles), the elastic constants measured for the bare silica particles were used and the values for the sound velocity and density of the PMMA shell were fixed on the values for bulk PMMA ($c_l = 2800$ ms^{-1}, $c_t = 1400$ ms^{-1}, $\varrho = 1190$ kg m^{-3}) [17]. However, this choice for the set of the elastic parameters of both the silica core and the

PMMA does not quantitatively represent the experimental resonances in the BLS spectra of Fig. 4.18c–e.

A systematic theoretical analysis based on the DOS spectra of the three core–shell spheres has shown that changes in the elastic parameters of *both* materials of the hybrid particles are required. Notably, it turned out that for the silica core one must assume sound velocities, which are about 3% higher than in the bare silica particle, i.e., $c_{l,c} = 4540$ ms^{-1} and $c_{t,c} = 2860$ ms^{-1}. This hardening of the silica core is probably due to a partial infiltration of methyl methacrylate in the pores and subsequent polymerization to PMMA during the formation of the shell. Due to the reduced impedance contrast between the silica core and the PMMA shell relative to the bare silica spheres vs. air, the core mass density ϱ_c has now a substantial influence on the DOS calculations. For a given density $\varrho_c = 1900$ kg m^{-3}, the sound velocities in the PMMA shell are $c_{l,s} = 3080$ ms^{-1} and $c_{t,s} = 1540$ ms^{-1}, i.e., about 10% higher than in bulk PMMA; the PMMA mass density was kept at the bulk value. Therewith, nearly all measured signals can be identified as spherical eigenmodes with angular momentum l and can be captured quantitatively by the theory within about 3%. The calculated resonance frequencies are shown by small vertical lines in Fig. 4.18c–e and summarized in Fig. 4.18f along with the corresponding experimental values. The Young modulus E and the shear modulus G are directly accessible for both the core and the shell components.

In order to obtain an insight into the nature of the experimentally observed modes (Fig. 4.18f), the elastic field at the resonance frequencies in the region of the sphere was calculated, assuming a longitudinal acoustic plane wave of the same frequency, impinging on the sphere (cf. Sect. 3.4.2 in Chap. 3). An example of elastic-field intensity plots is given in Fig. 4.19 for the case of the thickest PMMA shell sample ($d = 405$ nm). Their topology is that of a field-intensity having $2l$ maxima on the internal interface of the outer circumference of the core–shell particle: the two of them are strong (global) maxima along the direction of the incident field, while the rest $2(l - 1)$ are weaker and distributed equidistantly along the circumference. The vibration of the observed modes is radial at the maxima changing alternatively direction (outwards or inwards) from maximum to maximum. In the regions of minima the field is directed tangentially. Based on Fig. 4.19, the experimentally observed modes (Fig. 2f) are shell-localized with $l = 2$–4. Core-localized modes either do not exist within the considered frequency range (films with $d = 232$ and 294 nm), or they are not observable in the experimental BLS spectra (thickest-shell case, Fig. 4.18e), probably due to the very strong localization (virtually delta-functions in the DOS spectra). It is worth mentioning, however, that the elastic parameters affect the frequencies of both core- and shell-like eigenmodes.

Figure 4.20a shows the BLS spectra of two hollow capsules ($d = 232$ and 294 nm), akin to those of double-shelled hollow carbon microspheres published recently [60]. By comparison of the two spectra, it is apparent that the thicker hollow capsules display significantly sharper peaks than the thinner hollow capsules. For solid spheres, the line width of the spectra is associated with the size
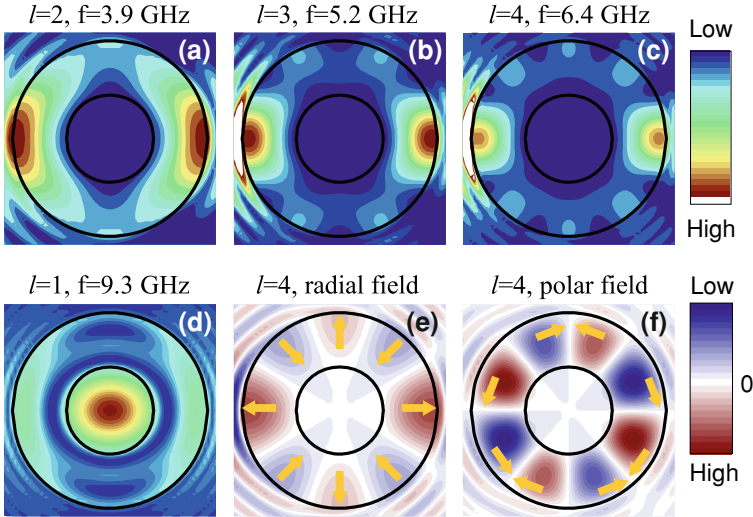
Fig. 4.19 a–c Elastic-field distribution for the first three resonances ($n = 1$) of the 405 nm core–shell particle (Fig. 4.18e) in a cross section through the center of the sphere. Plane wave incidence is assumed along the horizontal axis, from the left. **d** An example of core-localized mode with $l = 1$ ($n = 2$) at 9.3 GHz, which is not observed experimentally. Plots **e** and **f** give, respectively, the real part of the radial and polar component of the elastic field for the case shown in **c**, with the arrows visualizing the vibrational mode of the shell [34]

polydispersity [8]. For the thin hollow spheres ($d = 232$ nm), however, an additional source for the line broadening is the significant fraction of particles with holes as seen in Fig. 4.17b. These defects are neither uniform in size nor in shape and hence cause a distribution of the elastic properties that further broadens the experimental spectra (Fig. 4.20a). In order to identify the nature of the experimental eigenmodes in the two hollow capsules, the resonance frequencies of shell-localized modes were computed, adopting for the PMMA shell the values of the elastic moduli obtained from the representation of the eigenfrequencies of the core–shell particles (Fig. 4.18f). Figure 4.20b shows the calculated (solid lines) eigenfrequencies for the modes characterized by the angular momentum $l = 2$–4 for hollow PMMA nanoshells with constant inner diameter (181 nm) as a function of the (outer) particle diameter d. The comparison with the experimental frequencies (orange spheres) identifies the observed frequencies in the three hollow PMMA spheres with the two lowest modes with $l = 2$ and $l = 3$. Interestingly, the frequencies of these two modes vary very little with d due to two competing effects. At a constant particle diameter, the resonance frequencies of hollow particles increase with shell thickness [61], whereas the resonance frequencies of filled spheres decrease with d since $f(n, l) \sim 1/d$ [7–9]. Since in our case both shell thickness and total diameter increase simultaneously, the net effect is essentially the apparent insensitivity of the eigenfrequencies to the d variation of the branches with $l = 2$ and 3 seen in Fig. 4.20b. Notably, the elastic parameters of the PMMA were not affected by the core etching.

Fig. 4.20 **a** BLS eigenmode spectra of spherical hollow PMMA capsules with $d = 232$ and 294 nm. **b** Comparison between calculated (*solid lines*) and experimental (*spheres*) resonance frequencies for the hollow capsules ($n = 1$) [34]
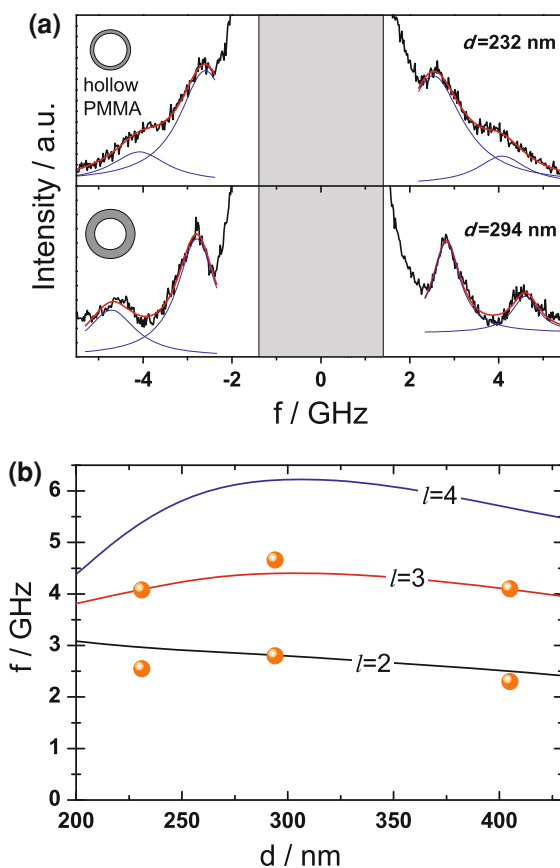
In summary, this section reports the first study of localized vibrational excitations in silica-PMMA core–shell particles and PMMA hollow capsules using the powerful optical technique of BLS, which is applicable for turbid films. The BLS spectra show up to nine eigenfrequencies of the core–shell particles, which sensitively depend on the particle architecture and the mechanical moduli of the constituent parts. The values of the Young moduli E and shear moduli G of the constituent components are computed from the elastic parameters c_l and c_t and densities, obtained for each component from the identification of the experimental modes with the resonance modes appearing at $f(n, l)$ for the n-th order of the l-th harmonic in the calculated density of states (DOS) spectra. The anticipated reduction of the moduli of the neat core compared to the bulk material due to its porosity and subsequent subtle increase above the bulk values upon grafting with PMMA chains are revealed. The anchoring and confinement of the PMMA nanoscopic layer impact both types of moduli which were found to exceed the bulk PMMA values. The observed eigenfrequencies in the hollow capsules exhibit a peculiar but apparent insensitivity to the variation of the diameter as a result of antagonistic trends inferred by the DOS calculations, while the PMMA elastic

constants are not affected by removal of the silica core. In addition to the fundamental understanding of localized elastic modes in hybrid particles and the concurrent determination of the mechanical moduli, the findings of this study will contribute to a rational design of nanostructured colloids with strong resonances that can be selectively excited [10].

4.4 Materials

4.4.1 Homogeneous Polymer Colloids

Homogeneous polystyrene, poly(methyl methacrylate), and poly(methyl methacrylate–co–n-butyl acrylate) colloids have been prepared by my coworker Dr. Retsch at MPIP by emulsifier-free emulsion polymerization [62], adapting recipes from the literature [63–66]. A general recipe for the used particles is given by the following [62]:

> The polymerization reactions were carried out either in a 300 ml reactor with a thermostat jacket or a 500 ml three necked flask. At first water was heated to the reaction temperature. Then all additives, monomers, and comonomers were added; solid chemicals were dissolved in water prior to addition. Strong magnet stirring was used and the chemicals were allowed to equilibrate for 5 min. Finally, the initiator was added as aqueous solution. The reactor was flushed with N_2 or Ar during charging with the chemicals and a slight inert gas flow was maintained throughout the reaction. Reaction times were typically between 12 and 20 h. […] Latex and silica nanoparticles were either purified by several cycles of centrifugation and redispersion, by ultrafiltration, or dialysis. In all cases the purification protocol was adjusted to the particles size and composition by means of centrifugation speed and duration, or filtration and dialysis membrane molecular weight cut-off.

PS Styrene (>99%, Aldrich) was washed three times with a 10% KOH solution and three times with MilliQ water and then distilled under reduced pressure. Acrylic acid (AA, 99%, Aldrich) was distilled without washing with KOH. Sodium 4-vinylbenzenesulfonic acid (NaPSS, 90%, Aldrich) and potassium persulfate (KPS, 99%, Acros) were used as received. By playing around with monomer, comonomer (KPS, AA), and initiator concentration, M. Retsch could prepare monodisperse PS spheres with diameter between 180 nm and 1 μm. All reactions were carried out with 0.1–0.2 g KPS, 0.005–0.06 g NaPSS, and 0–0.3 ml AA in 250 ml H_2O at 70 or 80 °C.

PMMA Methyl methacrylate (MMA, 99%, Acros) was washed three times with a 10% KOH solution and three times with MilliQ water and then distilled under reduced pressure. Sodium 4-vinylbenzenesulfonic acid (NaPSS, 90%, Aldrich), potassium persulfate (KPS, 99%, Acros), and 2,2′-azobis(2-methyl propionamidine) dihydrochloride (ABA, 97%, Aldrich) were used as received.

Cationic initiator (ABA) as well as an anionic system (KPS, NaPSS) have been used. The particle diameter is found to depend mainly on the initial MMA concentration.

PMMA-*n*BA Copolymers Methyl methacrylate (MMA, 99%, Acros) was washed three times with a 10% KOH solution and three times with MilliQ water and then distilled under reduced pressure. *n*-Butyl acrylate (*n*BA, >99%, Aldrich) was run over a basic alumina column. Sodium 4-vinylbenzenesulfonic acid (NaPSS, 90%, Aldrich) and potassium persulfate (KPS, 99%, Acros) were used as received. All reactions were carried out with 0.2 g KPS and 0.02 g NaPSS in 250 ml H_2O at 780 °C.

4.4.2 Homogeneous Silica Colloids

There are principally two synthetic strategies to obtain monodisperse silica colloids: a one-step batch process, which is also termed 'Stöber' process [67, 68], and a seeded growth process that can be performed step-by-step or continuously [69–71]. While the Stöber process is the simplest and fastest method, the monodispersity obtained by that is less good then that achieved using the seeded growth processes.

All processes avail themselves of the hydrolysis of tetraethyl orthosilicate (TEOS) to orthosilicic acid and subsequent condensation of the silicic acid to poly(silicon dioxide) (silica) under alcalic catalysis [ammoniac, NH_3(aq)] and strong magnetic stirring. As solvent a water/ethanol mixture is utilized due to the poor solubility of TEOS in water. The temperature is chosen between room temperature and 60 °C.

In order to control the particle size over a wide range and achieve high monodispersity by the same time, the typical approach is to start with a sample of monodisperse particles from the Stöber process (smaller diameter than the wished size) and then TEOS in EtOH and NH_3(aq) either in steps or in a continuous flow over several hours to days. It is found that the diameter increases monotonically with the amount of added monomer following a cubic root dependency and that the polydispersity decreases with increasing amount of added monomer, i.e., with the size. Both, step-by-step and continuous process, deliver high quality particles with comparable monodispersity [62]. The silica particles used in this thesis have been synthesized by my coworkers Retsch at MPIP and Kiefer at DKI, Darmstadt.

4.4.3 PS–SiO₂ Core–Shell Particles

PS–SiO_2 core–shell particles have been provided by my coworkers D'Acunzi and Schäfer at MPIP. Therefore they started with the soap-free emulsion polymerization of the polymer core and used them as templates for the synthesis of the silica shell employing the Stöber method [49, 72]. As the details are clearly and completely given in the mentioned literature, here I just want to introduce the main principles of the synthesis.

The synthesis of the PS core by soap-free emulsion polymerization was carried out using ammonium persulfate as initiator. Divinylbenzene (DVB) and acrylic acid were facultatively added as crosslinking (DVB) comonomers. Monomers and comonomers were dropwise added to a stirred aqueous solution of the initiator ammonium persulfate. The cores were cleaned by centrifugation.

To ease the coating with silica, the PS spheres were treated with polyelectrolytes [poly(allylamine hydrochloride)] and then functionalized with poly(vinyl-pyrrolidone) (PVP). The functionalized PS beads were transferred into ethanol. To form the silica shell, ammonia and tetraetoxysilane (TES) were added under stirring. The completed core–shell particles were washed three times in ethanol.

4.4.4 SiO₂–PMMA Core–Shell Particles

The SiO_2–PMMA particles with rigid silica cores and softer PMMA shells were prepared by my coworker Spahn at DKI Darmstadt in a two-step process starting with the Stöber synthesis of the core followed by emulsion polymerization of the shell [56]. The silica core, with a diameter of 181 ± 3 nm, was coated with PMMA spherical shells of three different thicknesses (in average 25, 57, and 112 nm), leading to core–shell particles of final (outer) diameter ranging from $d = 232$ to 405 nm.

References

1. Liff SM, Kumar N, McKinley GH (2007) Nat Mater 6:76
2. Joannopoulos JD, Johnson SG, Winn JN, Meade RD (2008) Photonic crystals: molding the flow of light. 2nd edition, Princeton University Press
3. Ozbay E (2006) Science 311:189
4. Cheng W et al (2006) Nat Mater 5:830
5. Duval E, Boukenter A, Champagnon B (1986) Phys Rev Lett 56:2052
6. Courty A et al (2005) Nat Mater 4:395
7. Kuok MH et al (2003) Phys Rev Lett 90:255502
8. Cheng W et al (2005) J Chem Phys 123:121104
9. Penciu RS et al (2000) Phys Rev Lett 85:4622
10. Mazurenko DA et al (2007) Phys Rev B 75:161102
11. Akimov AV et al (2008) Phys Rev Lett 101:033902
12. Hodak JH, Henglein A, Hartland GVJ (1999) Chem Phys 111:8613
13. Ruhl T, Spahn P, Hellmann GP (2003) Polymer 44:7625
14. Xia YN, Gates B, Yin YD, Lu Y (2000) Adv Mater 12:693
15. Hynninen A-P et al (2007) Nat Mater 6:202
16. Maldovan M, Thomas EL (2006) Appl Phys Lett 88:251907
17. Still T et al (2008) Phys Rev Lett 100:194301
18. Liu ZY et al (2000) Science 289:1734
19. Wang L, Baowen L (2008) Phys World 21:27
20. Gorishnyy T et al (2005) Phys Rev Lett 94

21. Lamb H (1882) Proc Lond Math Soc s1−13:189
22. Duval E, Boukenter A, Champagnon B (1986) Phys Rev Lett 56:2052
23. Duval E (1992) Phys Rev B 46:5795
24. Still T et al (2008) J Phys: Condens Matter 20:404203
25. Montagna M (2008) Phys Rev B 77:045418
26. Li Y et al (2008) Chem Phys Lett 461:111
27. Kuok MH et al (2003) Phys Rev Lett 91:149901
28. Sainidou R, Stefanou N, Psarobas IE, Modinos A (2005) Comp Phys Commun 166:197
29. Penciu RS et al (2003) J Chem Phys 118:5224
30. Faatz M et al (2005) Langmuir 21:6666
31. Lim HS, Kuok MH, Ng SC, Wang ZK (2004) Appl Phys Lett 84:4182
32. Sainidou R (personal communication)
33. Li Y et al (2006) Appl Phys Lett 88:023112
34. Still T et al (2008) Nano Lett 8:3194
35. Still T, D'Acunzi M, Vollmer D, Fytas G (2009) J Coll Int Sci 340:42
36. Alfrey T, Price CCJ (1947) Polym Sci 2:101
37. Greenley RZ (1999) Polymer handbook, vol. 1, 4th edition. Wiley, Hoboken
38. Penzel E, Rieger J, Schneider H (1997) A Polym 38:325
39. Strobl G (1997) The physics of polymers, 2nd edition. Springer, Berlin
40. Linderstrom-Lang K (1937) Nature 139:713
41. Fustin CA, Glasser G, Spiess HW, Jonas U (2004) Langmuir 20:9114
42. Still T et al (2010) Macromolecules 43:3422
43. Wood AB (1941) Textbook of sound. Macmillan, New York
44. Kafesaki M, Economou EN (1995) Phys Rev B 52:13317
45. Tommaseo G et al (2007) J Chem Phys 126:014707
46. Gill I, Ballesteros A (1998) J Am Chem Soc 120:8587
47. Van Helden AK, Jansen JW, Vrij A (1981) J Coll Int Sci 81:354
48. Donath E et al (1998) Angew Chem Int Ed 37:2201
49. Zhang L et al (2009) Langmuir 25:2711
50. Cheng W et al (2008) Nano Lett 8:1423
51. Cheng W et al (2007) Macromolecules 40:7283
52. Forrest JA, Dalnoki-Veress K, Stevens JR, Dutcher JR (1996) Phys Rev Lett 77:2002
53. Keddie JL, Jones RAL, Cory RA (1994) Faraday Discuss 98:219
54. Fox TG, Loshaek SJ (1955) Polym Sci 15:371
55. Mark JE (1999). Polymer data handbook. Oxford University Press, Oxford
56. Spahn P (2008) Phd thesis
57. Vlasov YA, Bo X-Z, Sturm JC, Norris DJ (2001) Nature 414:289
58. Pecora R (1985) Dynamic light scattering: applications of photon correlation spectroscopy. Plenum Press, New York
59. Sainidou R, Stefanou N, Modinos A (2004) Phys Rev B 69:064301
60. Li Y, Lim HS, Ng SC, Kuok MH (2007) Chem Phys Lett 440:321
61. Sainidou R, Stefanou N, Psarobas IE, Modinos A (2005) Z Kristallogr 220:848
62. Retsch M (2009) Complex materials via colloid crystallization. PhD thesis
63. Goodwin JW, Hearn J, Ho CC, Ottewill RH (1974) Colloid Polym Sci 252:464
64. Chung-Li Y, Goodwin JW, Ottewill RH (1976) Prog Coll Polym Sci 60:163
65. Shouldice GTD, Vandezande GA, Rudin A (1994) Eur Polym J 30:179
66. Egen M, Zentel R (2004) Macromolecular chemistry and physics 205:1479
67. Stöber W, Fink A, Bohn E (1968) J Coll Int Sci 26:62
68. Giesche H (1994) J Eur Ceram Soc 14:189
69. Bogush GH, Tracy MA, Zukoski Iv CF (1988) J Non-Cryst Solids 104:95
70. Zhang JH et al (2003) J Mater Res 18:649
71. Giesche H (1994) J Eur Ceram Soc 14:205
72. Graf C, Vossen DLJ, Imhof A, van Blaaderen A (2003) Langmuir 19:6693

Chapter 5
Phononic Behavior of Colloidal Systems

5.1 Introduction

The first papers on photonic effects by Yablonovitch [1] and John [2] in 1987 stimulated over the years much theoretical and experimental work on the propagation of electromagnetic waves through appropriately structured materials and subsequently led to the birth of the new research field 'photonic crystals' [3]. The tremendous interest in photonic crystals with specially designed periodic variations in dielectric constant largely originates from their display of propagation band gaps for light. The appearance of band gaps makes an advanced control over light propagation possible and permits as well a series of novel optical phenomena such as slowing and localization of light or negative refraction [3]. Soon after the discovery of photonic crystals, it was found that in analogy to the electromagnetic waves, band gaps also exist for the propagation of acoustic waves, and the so-called phononic crystals [4–10] are the elastic analogue of photonic crystals replacing the role of the dielectric constant by the elastic parameters and density. Such an analogy exists as a consequence of the common origin of the band gaps in both cases, i.e., the destructive interference of Bragg diffracted waves in periodic structures [11, 12], and hence these gaps are also termed as Bragg gaps. However, the different nature of electromagnetic and acoustic waves also guarantees the existence of some important differences between photonic and phononic phenomena. Unlike electromagnetic radiation that is characterized as transverse waves, acoustic waves in general are full vector waves with both longitudinal and transverse polarizations, and their propagation depends additionally on the material density. Even for a homogeneous and isotropic medium, the acoustic wave propagation is governed by three parameters, the two Lamé coefficients and density, in contrast to the single parameter, the dielectric constant, that determines the propagation of light. Evidently, the phononic phenomena are anticipated to be more complex and rich.

For phononic crystals, the band diagram depends on several parameters such as the elastic constants and density of the component materials, symmetry of the lattice, shape of the inclusions, and the filling fraction. The width of the band gap

generally increases with the contrast between the densities and sound phase velocities of the component materials, and the center of the gap can be tuned by changing the lattice parameter [9, 10]. The search for phononic structures started with two theoretical works in 1993, which predicted the existence of phononic band gaps in periodic two-dimensional (2D) elastic composites of parallel cylinders embedded in a host matrix [9, 10]. The experimental verification of phononic band gaps followed few years later, realized in metallic macrostructures with gaps at sonic or ultrasonic frequencies [4, 5, 8, 13]. Further explorations also revealed a number of peculiar phenomena with potential applications associated with acoustic wave propagation including tunneling effect [14], negative refraction and focusing [15], double refraction, etc. [16].

Theoretical calculation of phononic band diagram requires no specification of the lattice constant of the structure or the corresponding wave frequencies as long as the crystal is defined by the same set of frequency-independent elastic parameters. In other words, a fundamental length scale does not exist for phononic phenomena, which is a direct consequence of the invariance of the wave equation of elasticity under the simultaneous transformation of space coordinates and frequency. However, acoustic waves of different frequencies do bear distinct characteristics, particularly when their applications are concerned, and therefore in practice the frequency range of the waves of interest constitutes an important consideration. Recently, growing attention has been paid to hypersonic (GHz) phononic crystals and the first experimental observations of the hypersonic Bragg gaps have been lately reported in three-dimensional (3D) colloidal crystals made by self-assembly [17] and in 2D polymeric porous structures with hexagonal symmetry created by laser interference lithography [18]. Hypersonic waves, owing to their high frequencies, display certain unique features that are not possessed by ordinary acoustic waves such as being thermally excited, acting as the main heat carrier in dielectrics, and interacting with electrons and photons in a rich manner. Consequently, hypersonic crystals with the potential to mold the flow of hypersound may be utilized to achieve high-level control over many important physical processes involving heat transport and complex phonon–photon or phonon–electron couplings. A detailed understanding of phonon propagation in hypersonic crystals thus becomes important.

The fabrication of hypersonic crystals, compared with their sonic and ultrasonic counterparts, is much more demanding as the dimension typifying the structure has to be scaled from macroscopic down to sub-micron scale. On the other hand, advance in relevant nanofabrication, partially driven by the desire of creating various photonic structures of similar dimensions, has offered some available means to achieve such a purpose including, for example, holographic interference lithography [19], direct laser-writing [20], two-photon polymerization [21], or self-assembly [22, 23]. Colloidal superstructures, self-assembled from colloidal particles, represent a promising material class for phononic applications. The maturation of colloidal science enables the preparation of colloidal particles with well-defined size and shape for a great many of materials ranging from organic to inorganic, thus providing abundant building blocks with varied elastic properties.

The progress in colloidal particle self-assembly allows easy and cheap fabrication of large area high quality single crystalline 2D and 3D crystals as well as non-crystalline structures. The appearance of binary [24] and ternary [25] crystals further enriches the available structure types. By filling the interstitials between the colloidal particles with different materials, additional freedom in elastic parameters of the system is provided. Moreover, in most cases the colloidal particles possess a spherical shape due to surface tension effects, thus represent a strong scattering unit when the elastic contrast between the particle and surrounding becomes large, which may cause additional gap formation with origin different from Bragg diffraction as will be encountered later [26].

The experimental exploration of hypersonic crystals, however, faces additional challenge in monitoring the phonons in such small structures. Apparently, the commonly used sonic and ultrasonic transmission techniques for macroscopic sized structures cease to work. It has been demonstrated that Brillouin light scattering (BLS), which takes advantage of the inelastic scattering of photons by thermally excited high frequency phonons, represents a powerful tool to record the phonon dispersion relation in hypersonic crystals.

This chapter deals with the phononic band diagrams of transparent colloidal systems that can be measured by BLS. A short introduction into the nature of the bands in the dispersion relation is given as well as into the properties of the effective medium. Experimental results are discussed treating the effective medium velocity of infiltrated defect doped colloidal crystals and the nature of acoustic band gaps in phononic systems, including the first realization of a hybridization gap.

5.1.1 The Phononic Band Diagram

The information about the propagation of elastic waves in periodic media is described by the band diagram. It contains the dispersion relation frequency as a function of the wave vector, $\omega(\boldsymbol{k})$. Therefore the vertices of the irreducible Brillouin zone (BZ) are connected with a line for each acoustic mode appearing. Figure 5.1a shows for example the band diagram for an *fcc* lattice (see also Fig. 5.5) of lead spheres in a beryllium matrix (filling fraction 8.23%), calculated by Economou and Sigalas using the plane wave method (cf. Sect. 3.4.2 in Chap. 3) [27]. The lowest two branches (indeed, the lowest three as the two very lowest ones are degenerated) are the so-called acoustic ones. At the central point of the BZ, Γ, their frequency is zero, and around Γ the frequencies increase linearly (dispersionless) in all crystallographic directions, i.e., in these regions phase and group velocities of the corresponding acoustic waves are equal.

Away from this long wavelength (small k) limit, when the branches approach the edge of the (first) BZ, the linear behavior vanishes and a bending occurs. That bending can be best explained for the simplest case of a periodic elastic system—an one-dimensional lattice of vibrating identical spheres with mass m connected
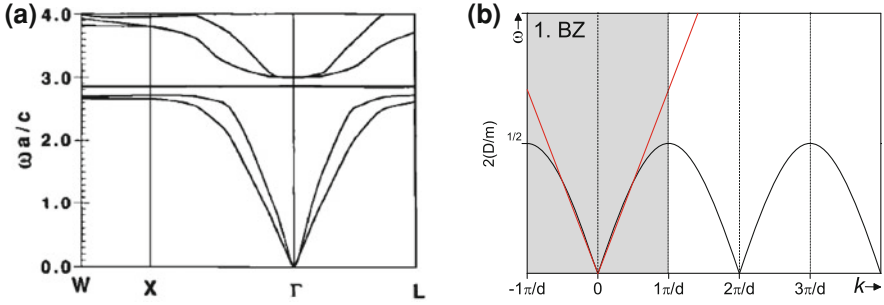
Fig. 5.1 a From (Ref. [27]) calculated acoustic band diagram for lead spheres in a beryllium matrix forming an *fcc* lattice with an occupancy of 8.32 vol% the lowest (transverse) branch is degenerated. The three flat branches around 2.8 $\omega a/c$ are degenerated, too. There are two complete band gaps. **b** Dispersion of the longitudinal waves in a 1D simple crystal (*black line*) over several Brillouin zones. The *dashed line* denotes the dispersionless 'free particle' case

with massless elastic springs with spring constant D and equilibrium distance a as shown in Fig. 5.2 [28, 29]. Let us assume a longitudinal wave, which creates displacement of the spheres in the direction of the chain. When assuming (in reasonable approximation) that the elastic forces that determine a vibration have their origin in the relative displacement only of neighboring particles, symbolized by the compressed and stretched springs in Fig. 5.2 leading to forces (black arrows) in the same direction, while the inertia originates from the absolute displacement of the spheres in space. With $u(na)$ being the absolute displacement of the nth sphere, the harmonic potential between all neighboring spheres becomes

$$U^{\mathrm{harm}} = \frac{1}{2}D \sum_{n} \left(u(na) - u([n+1]a) \right)^2. \tag{5.1}$$

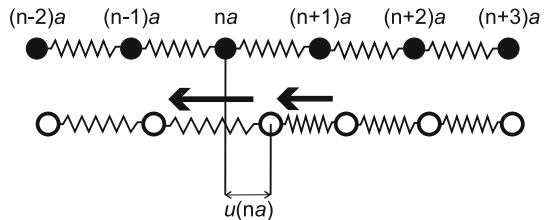Since elastic forces and inertia must compensate each other, the equation of motion becomes

$$m\frac{\partial^2 u(na)}{\partial t^2} = -\frac{\partial U^{\mathrm{harm}}}{\partial u(na)} = -D[2u(na) - u([n-1]a) - u([n+1]a)]. \tag{5.2}$$

Assuming a plane longitudinal wave of the form

$$u(na,t) \propto e^{i(kna - \omega t)} \tag{5.3}$$

Fig. 5.2 Illustration of a longitudinal mechanical wave in an 1D elastic lattice

and inserting into Eq. 5.2 delivers

$$-m\omega^2 e^{i(kna-\omega t)} = -D[2 - e^{-ika} - e^{ika}]e^{i(kna-\omega t)}. \tag{5.4}$$

After algebraic transformation the dispersion relation is obtained:

$$\omega(k) = \sqrt{\frac{2D(1 - \cos(ka))}{m}} = 2\sqrt{\frac{D}{m}}\left|\sin\left(\frac{ka}{2}\right)\right|. \tag{5.5}$$

The dispersion relation for this simple case is shown in Fig. 5.1b for several BZs. The periodicity of the lattice is recovered also in the dispersion relation in reciprocal space. In the long wavelength limit, i.e., $k \ll \frac{\pi}{d}$, Eq. 5.5 can be simplified to

$$\omega(k) \approx \sqrt{\frac{D}{m}}kd, \tag{5.6}$$

using the approximation $\cos(kd) \approx 1 - (kd)^2/2$. This corresponds to the mentioned linear behavior at small ks. In Fig. 5.1b, dashed lines are drawn for comparison that show purely linear slope. This behavior corresponds to the 'free particle' case, i.e., a phonon in a continuum. Of course, in this case the axis caption including the periodicity d is meaningless and k is simply given by $k = 2\pi/\Lambda$ with phonon wavelength Λ. The slopes of the linear regions of the acoustic branches give the effective longitudinal and transverse velocities c_l and c_t.

At the edge of the first BZ ($k = \pi/d$), Eq. 5.5 becomes

$$\omega = \sqrt{\frac{4D}{m}}, \tag{5.7}$$

with corresponding longitudinal phase velocity $c_l = \sqrt{D/m} \cdot 2d/m$ and group velocity zero. Waves that fulfill that condition are reflected into themselves (for normal incidence) and form a standing wave.

Above the acoustic branches, in Fig. 5.1a some flat bands appear around 2.8 reduced wavelength (indeed, there are three of them). Since these branches are apparently almost k-independent and because of their degeneracy, they are identified as eigenwaves basically trapped within the lead spheres with little leaking out [27]. These are resonance modes similar to the eigenvibrations discussed in Chap. 4, however, this time no free boundary conditions exist, but there is an exchange of energy between the spheres and the matrix. Only if the elastic mismatch (i.e., densities and moduli) is large enough between spheres and matrix, such a trapping can happen. With decreasing mismatch the amount of dissipation increases and finally, for no elastic mismatch, the systems behaves like a continuum, i.e., only acoustic modes appear.

At higher frequencies also mixed modes with transverse as well as longitudinal components appear. These modes may become quite numerous even for relatively simple systems. For systems with liquid matrix that do not support shear waves, the calculation might become a bit easier, however, it is still more complex than the analogue investigations for electromagnetic waves. In systems where one

component supports shear waves and the other component does not, one must not ignore the conversion between waves of different nature into each other that is described mathematically by the T-matrix (Eq. 3.28).

Regions in the band diagram where no band exists for all ks are called phononic band gaps. These are frequency regions where no mechanic wave can propagate. Since the existence of such gaps is one of the striking features of the band diagram and promises also some technical importance, the search for and investigation or tailoring of phononic band gaps is a demanding question in the young field of phononics.

In the following parts of the introduction, the properties of the effective medium as well as a short overview over the phononic band gaps is given. The rest of this chapter is concerned with experimental studies on colloidal phononic systems, including the investigation of the effective medium velocities in defect doped opals, the first experimental realization of a hybridization gap and the band diagram of nanostructured systems.

5.1.2 The Effective Medium

The slope at the long wavelength limit in the band diagram gives the longitudinal and transverse sound velocities, c_l and c_t, respectively. While these velocities are well known for the most pure materials, their prediction for composite materials of varying composition and geometric structure is not straight forward and the topic of the effective medium theory (EMT).

A very general approach to predict the effective longitudinal velocity of a two components system is given by Wood's law as the harmonic mean of the moduli [30]:

$$\frac{1}{M_{\text{eff}}} = \frac{\phi_1}{M_1} + \frac{(1 - \phi_1)}{M_2}, \tag{5.8}$$

where $M = c_l^2 \varrho$ is the bulk longitudinal modulus of each component. In principle this approach can be generalized for n components to

$$\frac{1}{M_{\text{eff}}} = \frac{\phi_1}{M_1} + \frac{(\phi_2)}{M_2} + \cdots + \frac{(\phi_n)}{M_n} \tag{5.9}$$

with $\sum_n \phi_n = 1$. For equal mass densities ($\varrho_1 = \varrho_2$), the effective longitudinal velocity would be given as the harmonic mean of the squared sound velocities of the components ($c_l \equiv [\langle 1/c_l^2 \rangle]^{-1/2}$). For transverse sound velocities, it should be sufficient to replace the bulk longitudinal moduli in Eq. 5.8 by the share moduli.

Anyhow, the simple assumption of Wood's law ignores for example the interaction of longitudinal and transverse waves between different components as it (in the longitudinal version) compares only the bulk moduli. However, in certain

cases, these interactions may lead to conversion of energy between bulk and shear waves (T-matrix) and must not be ignored anymore. In the theoretical calculations mentioned above [27], the authors compare the calculated effective velocities for several different cases with the arithmetic mean and the harmonic mean of the sound velocities as well as with the square root of the harmonic mean of the squared velocities of the components—all weighted with the filling fraction, but not with the mass densities. This deviation from Wood's law does not lead to a reproducible result for all cases, since in some cases the one mean is nearer to the calculated result while in other cases another mean is nearer to the theoretical findings. However, even applying Wood's law, which is not done in the paper, does not deliver perfect agreements for all cases, although a relatively large deviation is achieved only in the case of lead inclusions in a beryllium matrix with a filling fraction of 8.23%. Here, using the parameters given by the authors, Wood's law delivers an effective longitudinal sound velocity of 9,250 ms^{-1}, while the calculated velocities are about 10% higher, between 10,226 and 10,619 ms^{-1}, depending on the crystallographic direction.

For the special case of spherical inclusions (and the practical application for approximately spherical inclusions), a more sophisticated but still easy-to-apply EMT method was developed mainly by Gaunaurd and Wertman, reviewed by the same in Ref. [31]. In their calculations they take the ratios of longitudinal and transverse sound velocities for both components into account as well as the ratio of the mass densities. Furthermore, the effective density is calculated differently for the two general subcases of matrices that can only support insignificant amounts of shear ('fluid matrices') and 'elastic matrices' supporting non-negligible amounts of shear.

When calculating the effective longitudinal sound velocities for the different cases in Ref. [27] following this approach (utilizing a small C++ program written by myself), reasonable results are obtained for all subcases (Au/Si, Pb/Si, Pb/Be, and Au/SiO$_2$), although for some subcases from the theoretical band diagram there are different effective velocities in different crystallographic directions, which are described unequally well by this EMT. E.g., for the Pb/Be subcase mentioned above, the program gives an effective sound velocity of 10,820 ms^{-1}, which is only about 2% more than predicted for the Γ–L direction.

In Table 5.1 three general cases of phononic systems with filling fraction ϕ are compared for Wood's law and the EMT of Gaunaurd and Wertman: polystyrene spheres in silicon oil (solid/liquid), alumina spheres in PS (solid/solid), and air bubbles in silicon oil (gas/liquid).[1] For all subcases the values following the Gaunaurd and Wertman approach are given for fluid (GW$_f$) and elastic matrix (GW$_e$), although principally the latter should be meaningful only in the alumina/ PS subcase since silicon oil that is matrix in the other two subcases does not support shear waves.

---

[1] Material parameters: PS: c_t: 1,200 ms^{-1}, c_l: 2,350 ms^{-1}, ϱ: 1,050 kg m^{-3}; silicon oil: c_t: 0 ms^{-1}, c_l: 1,400 ms^{-1}, ϱ: 1,000 kg m^{-3}; Al$_2$O$_3$: c_t: 6,345 ms^{-1}, c_l: 10,850 ms^{-1}, ϱ: 3,970 kg m^{-3}; air: c_t: 0 ms^{-1}, c_l: 343 ms^{-1}, ϱ: 1.2 kg m^{-3}.

Table 5.1 Comparison between calculated effective longitudinal sound velocities (in ms^{-1}) using the EMT of Gaunaurd and Wertman (GW) and Wood, respectively, for three cases and five filling fractions ϕ

ϕ	PS in silicon oil			Al_2O_3 in PS			Air in silicon oil		
	GW_f	GW_e	Wood	GW_f	GW_e	Wood	GW_f	GW_e	Wood
0.74	1,714	1,714	1,925	2,854	2,522	2,590	42	27	27
0.50	1,588	1,587	1,691	2,479	2,104	2,136	34	24	24
0.20	1,466	1,466	1,496	2,362	2,095	2,103	35	30	30
0.05	1,416	1,415	1,422	2,351	2,257	2,258	57	54	54
0.001	1,400	1,400	1,400	2,350	2,348	2,348	364	364	364

GW calculations for fluid and elastic matrix, GW_f and GW_e, respectively

For the first case of PS in silicon oil, it does not make any significant difference which kind of matrix is taken into account. Both calculations come to practically the same results, leading to sound velocities lower than those predicted by Wood's law. With increasing filling fraction the difference increases up to 12% for the dense packing case $\phi = 0.74$.
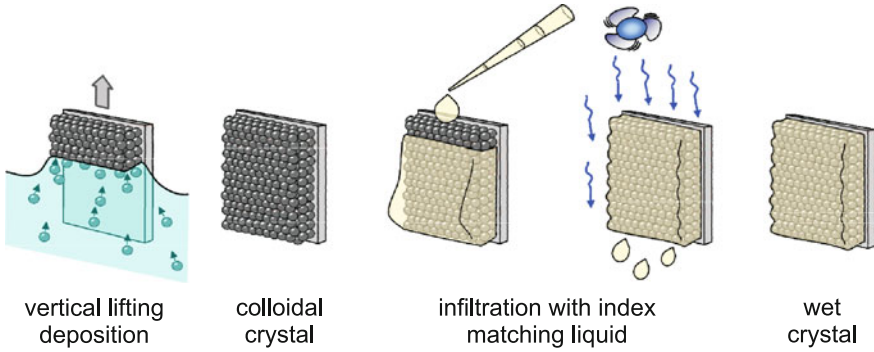
In the subcase of a harder solid embedded in a softer one (alumina in PS), GW_e and Wood's law deliver quite similar results, differing by less than 3% at $\phi = 0.74$, while the theoretically meaningless GW_f delivers significantly higher values.

The last subcase of air bubbles in silicon oil shows that in this case, where both components' transverse sound velocities are set to zero, GW_e delivers exactly the same results as Wood's law, while the GW_f calculations give higher values. However, even for very low filling fractions all theories give extremely low values. This means that even a low amount of air bubbles should slow down the effective sound velocity in a liquid.

Another EMT method is described by Waterman and Truell [32]. Their approach is in principle a full multiple scattering theory including numerical calculation with n equations for n scatterers. For every scatterer the exact form of the multipole coefficient must be known, and so this method is too complicated to be used for simple calculations of the effective sound velocity. Taking the effective sound velocity from the theoretical band diagrams calculated by the multiple scattering method touched on in Sect. 3 in Chap. 3 is very akin to this approach.

5.1.3 Phononic Band Gaps

To measure the phononic dispersion relation of colloidal crystals by BLS, the strong multiple scattering that leads to the eigenmode spectra discussed in Chap. 4 should be overcome. This is achieved by infiltration of the dry opals by a fluid with refractive index close to that of the colloidal spheres (Fig. 5.3). For

vertical lifting | colloidal | infiltration with index | wet
deposition | crystal | matching liquid | crystal

Fig. 5.3 Infiltration of a turbid colloidal crystal with an index matching liquid resulting in a transparent 'wet' crystal (according to [17])

poly(methyl methacrylate) (PMMA, $n = 1.49$) or PS ($n = 1.59$) colloids for example silicon oil ($n = 1.45$) or liquid poly(dimethylsiloxane) (PDMS, $n = 1.41$) are suitable infiltration liquids. Using such 'wet' colloidal crystals, the first experimental access to the phononic band diagram along high symmetry directions in submicrometer artificial crystals was recently reported [17], leading to the observation of phononic band gaps in the GHz-range. Till then, only sonic and ultrasonic crystals had been investigated by other techniques, mostly by sonic- and ultrasonic transmission experiments or by a special video spectroscopy methods applied to 2D [33] and 3D [34] experiments. The observation of a hypersonic band gap in a 2D hypersonic phononic crystal by BLS was subsequently reported [36].

The nature of the observed band gaps is clearly that of a Bragg gap (BG). A BG exists due to annihilation of the incident mechanical wave and the waves scattered on the individual spheres in the crystal. To create a band gap, the periodic structure length in the crystal must be of the order of the relevant phonon wavelength. If the phonon wavelength and the distance between the crystal planes in the direction of the phonon propagation become equal, the scattered mechanical waves interfere constructively and the energy of the incident wave is reflected back opening a phononic gap.

Fcc crystals of sub-micron PS spheres are prepared by vertical lifting deposition. After infiltration with PDMS, the dispersion relation, $f(q)$, was recorded by angle dependent BLS measurements along high-symmetry directions in the reciprocal space. As shown in Fig. 5.4 at low qs, the dispersion relation is that of mechanical waves traveling through a homogeneous medium with an effective sound velocity, i.e.,

$$\omega = 2\pi f = c_{\text{eff}} q. \tag{5.10}$$

As q reaches the edge of the first BZ at $q_{\text{BZ}} = (3/2)^{3/2}\pi/(\sqrt{2}d)$ in the probed Γ–M direction (cf. Sect. 5.1.3), the fulfillment of the Bragg condition leads to a gap opening. Accordingly, the frequency of the observed gap is [5, 35]
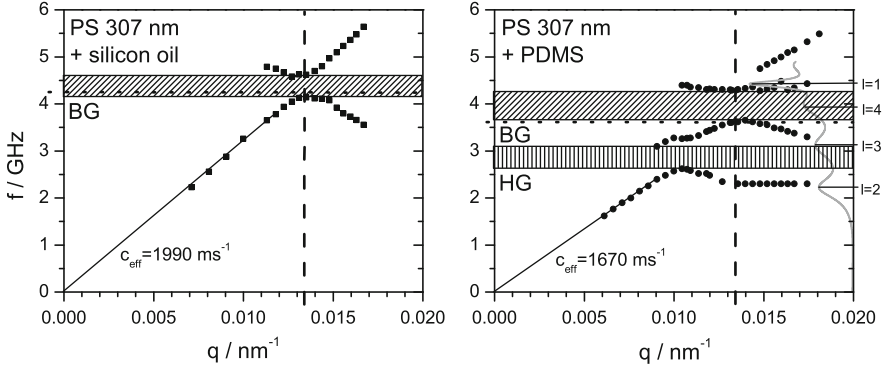
Fig. 5.4 The dispersion relations of a colloidal PS ($d = 307$ nm) opal infiltrated with silicon oil (*left see also Ref.* [17]) and with PDMS (*right, see also Fig. 5.11 and Ref.* [26]) in the Γ–M direction of the *fcc* crystals are compared. In both spectra there is a clear BG (*diagonal pattern*). The *dashed lines* indicate the Γ–M distance in the reciprocal space, hence the edge of the first BZ. The *dotted lines* denote the frequencies that correspond to q_{BZ} (cf. Sect. 5.1.3). For the opal infiltrated with PDMS a HG (*vertical pattern*) appears, too [35]

$$f = q_{BZ} c_{eff}/2\pi. \tag{5.11}$$

The position of the gap can be widely tuned by changing the lattice parameters of the hypersonic phononic crystal due to the linear dependence of the gap frequency from the inverse diameter.

The width of the BG increases with elastic mismatch between the spheres and the infiltrated liquid. In fact, the width of the gap in the wet PS opals systematically increases when the infiltrated liquid changes from glycerin ($c_l \approx 2,200\,\mathrm{ms}^{-1}$) to silicon oil ($c_l = 1,400\,\mathrm{ms}^{-1}$) and to PDMS ($c_l = 1,050\,\mathrm{ms}^{-1}$). According to the results of effective medium theory [31, 37], the value of c_{eff} lays in between the components' individual sound velocities. It is noteworthy that the calculation of effective sound velocities following the approach of Gaunaurd and Wertman [31] tends to result in moderately but certainly too small values compared with the experiment, actually the deviations are smaller than 10%.

In Sect. 5.3.1 the first experimental realization of an additional gap besides the BG, the so-called hybridization gap (HG) is demonstrated [35]. This HG originates from the interaction of the band of quadrupole particle eigenmodes with the band of the effective medium. This kind of gap opens up from level repulsion when two bands of the same symmetry cross each other (in analogy to the linear combination of atomic orbitals) [38]. In this case, the involved bands are the acoustic field of the extended states in the effective medium and the bands from the multipole modes of the interacting spherical particles, which can be treated as local resonant elements.

The first hint on this gap was found in BLS experiments in colloidal suspensions [39, 40], but a clear demonstration, assignment and the concurrent observation along with the BG was just reported in the case of PS and PMMA wet opals infiltrated with PDMS.

5.1.3.1 Normalization

In general, the condition that has to be fulfilled to create a Bragg gap is that the distance between two scattering planes in the direction of the incident wave matches the wave length of the wave, or, in reciprocal space, that the wave vector **q** is half the diameter of the first Brillouin zone in a certain crystallographic direction. By the method of vertical lifting deposition (Sect. 3.1 in Chap. 3) the colloidal *fcc* crystals show a preferred orientation relative to the substrate. When inserting the sample in the same orientation as prepared into the BLS setup and utilizing the special transmission geometry, where the wave vector is parallel to the substrate, the probed direction in the reciprocal lattice is usually the Γ–M direction. The first BZ of an *fcc* lattice is shown in Fig. 5.5. In the Γ–M direction, the distance in reciprocal space between Γ and M is

$$|\Gamma - M| = \frac{\left(\frac{3}{2}\right)^{3/2}\pi}{\sqrt{2}d} \tag{5.12}$$

with sphere diameter d. Therefore, the wave vector q_{BZ} in this crystallographic direction must have the same value to fulfill the Bragg conditions, because $|\Gamma - M|$ is half the diameter of the Brillouin zone D_{BZ}, i.e.,

$$q_{BZ} = \frac{D_{BZ}}{2} = \frac{\left(\frac{3}{2}\right)^{3/2}\pi}{\sqrt{2}d}. \tag{5.13}$$

If one assumes pure acoustic behavior with an effective sound velocity c_{eff} the frequency at q_{BZ} would be

Fig. 5.5 First Brillouin zone (BZ) of an *fcc* lattice. The *black line* denotes the equator for the body standing on a hexagon, on which the point M is located
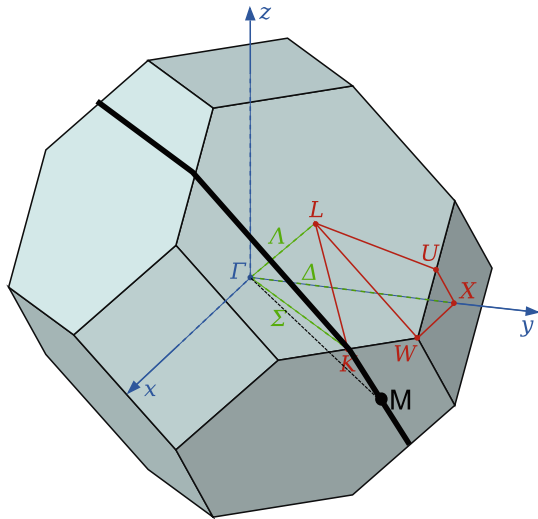
$$f_{BZ} = \frac{c_{eff}q_{BZ}}{2\pi} = \frac{c_{eff}D_{BZ}}{4\pi} = \frac{\left(\frac{3}{2}\right)^{3/2}c_{eff}}{2\sqrt{2}d} \tag{5.14}$$

with $f = \omega/2\pi = cq/(2\pi)$. Now one can normalize the measured values for the frequency and the wave vector to the values at the edge of the Brillouin zone:

$$f_{norm} = \frac{f}{f_{BZ}} = \frac{2f\sqrt{2}d}{\left(\frac{3}{2}\right)^{3/2}c_{eff}} \approx 1.54\frac{fd}{c_{eff}} \tag{5.15}$$

$$q_{norm} = \frac{q}{q_{BZ}} = \frac{q\sqrt{2}d}{\left(\frac{3}{2}\right)^{3/2}\pi} \approx 0.245qd \tag{5.16}$$

5.2 Effective Medium Velocity in Defect Doped Opals

Brillouin light scattering can be used to measure the effective sound velocity in homogeneous materials as well as in structured materials if the structure size is smaller than the traveling phonon, or in other words, if $2\pi/q > d$ with structure spacing d. E.g., for $q = 0.01$ nm^{-1} (that corresponds to an angle of $\approx 50°$ in transmission geometry for the setup described in Sect. 2.3.2 in Chap. 2) the structure must be clearly smaller than 600 nm.

While in bulk, not too thin films of a single polymer of course the polymer's sound velocities (if it support shear waves) are found, in films of thin multilayers of different components, e.g., for two different polymers, the individual sound velocities of both components are found when measuring parallel to the interfaces [41]. If the wave vector is chosen perpendicular to the layers, at least for thin (<30 nm) layers, only one signal corresponding to the effective sound velocity is found. Following the effective medium theories, c_{eff} lays in between the velocities of the individual components [42].

Effective sound velocities are also found in nano- and mesoscopic 3D structures like the infiltrated colloidal crystals presented in Sect. 5.1.3. In Fig. 5.4 c_{eff} is shown for PS colloidal crystals ($\phi = 0.74$) infiltrated with silicon oil (left) or PDMS (right). The effective sound velocities are 1,990 and 1,670 ms^{-1}, respectively. These are between those of PS ($c_l = 2,350$ m/s, $\varrho = 1,050$ kg m^{-3}) and PDMS ($c_l = 1,050$ m/s, $\varrho = 965$ kg m^{-3}) or silicon oil ($c_l = 1,400$ m/s, $\varrho = 1,000$ kg m^{-3}) [26]. The EMT of Gaunaurd and Wertman [31] delivers effective velocities of 1,714 and 1,488 m/s, for silicon oil and PDMS as infiltration liquid, respectively, using the numbers given above. Wood's law, on the other hand, delivers 1,925 and 1,617 m/s, respectively, i.e., both EMTs seem to underestimate the real effective sound velocities, however for Wood's simple law, the error is significantly smaller.

A more systematic study of the influence of the filling fraction on the effective sound velocity in PS colloidal crystals infiltrated with PDMS and the comparison with EMT was performed within the framework of this thesis. Therefore, a set of colloidal crystals consisting of PS colloids ($d = 260$ nm) and a certain amount of silica particles with practically the same diameter ($d = 255$ nm) were synthesized

by my coworker Markus Retsch (who also performed the characterization in Fig. 5.6). Since the size difference is clearly below 5% [44], the particles form random co-crystals during vertical lifting deposition under stirring. Figure 5.6a–d shows the SEM pictures of four different co-crystals with composition of the initial particle dispersion PS:SiO$_2$ between 2:1 (a) and 12:1 (d); the brighter spheres correspond to the silica particles. It can be seen that the samples are nicely crystalline and nearly crack- and defect-free over many micrometer, i.e., the filling fraction ϕ is in good approximation that of an *fcc* lattice, $\phi = 0.74$.

It must be expected that the real composition in the composite crystals differs from that in the initial dispersions due to the different mass density of both types of particles and other possible surface effects that cannot be fully discussed in this context. In order to determine the real ratios, TGA (Fig. 5.6i) and UV/VIS
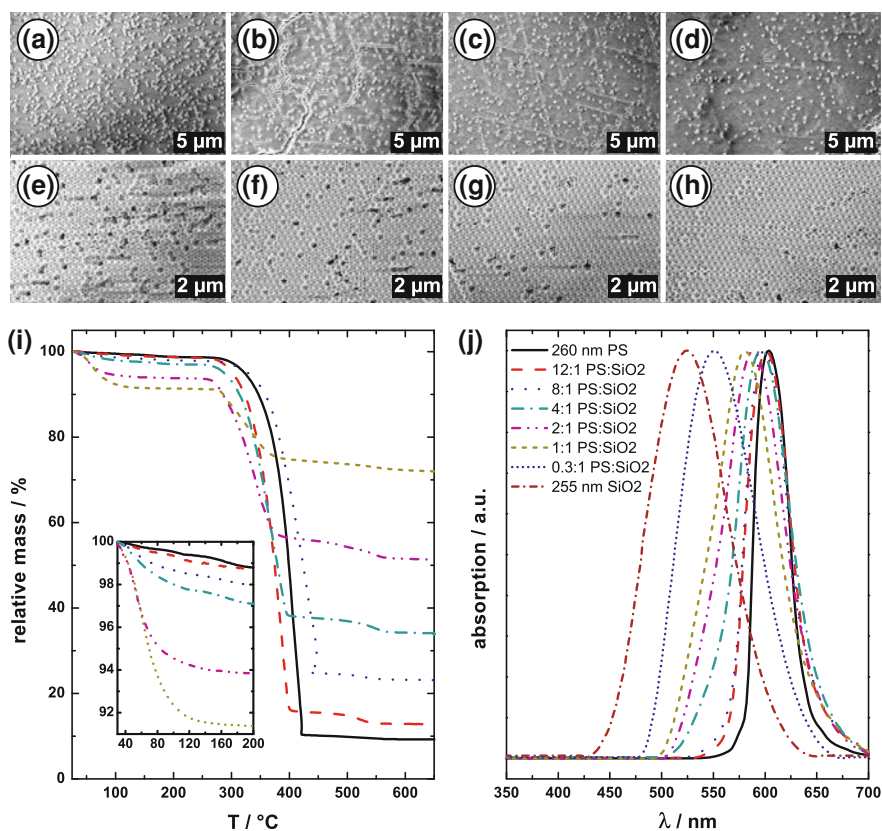
Fig. 5.6 SEM pictures: **a–d** PS:SiO$_2$ colloidal crystals with composition 2:1, 4:1, 8:1, and 12:1; **e–h** The corresponding defect doped crystals after etching away the silica beads. Analytics: **i** TGA measurement on the composite PS:SiO$_2$ colloidal crystals (decomposition of PS). The *inset* shows the loss of water (legend like in **j**); **j** UV/VIS spectra of the PS:SiO$_2$ colloidal crystals shown in **a–d**. For comparison also the spectra of the pure PS colloids, the pure silica colloids and of two mixtures with higher amount of silica are shown (according to [43])

measurements (Fig. 5.6j) were performed and the results were compared with the counting of the SEM pictures. From the TGA measurements it is easy to calculate the PS:silica ratio at high temperatures the PS is decomposed and only the silica spheres remain. By comparing the relative mass loss and taking into account the different mass densities and the exact radius of the spheres the relative amount of the polymer is obtained [43]. It should be noted that it is meaningful to compare the change for the dry samples i.e., to set the starting point of the comparison at $T > 100\,°C$ (inset in Fig. 5.6i).

The counting of the SEM pictures shows that systematically less silica particles are built in the crystals than should be expected from the initial dispersion concentrations. However, the SEM pictures show only the distribution on the imaged surface and, by what reason ever, the ratio inside the opal could be different. Anyhow, the comparison between the data obtained by the TGA measurements and the SEM counting lead to a systematic and consistent result [43]. The amount of silica is always given by approximately 0.8 times the expected fraction, i.e., the real ratio of the '12:1' PS:SiO$_2$ sample is $\approx 12{:}0.8$, etc., however, for the rest of this section the names originating from the initial ratio are kept to avoid confusion.

The so found real compositions are verified by the UV/VIS measurements shown in Fig. 5.6j. From the graph that contains also two additional samples with initial ratio 1:1 and 0.3:1 it can be seen that there is a clear blue shift of the Bragg peak for increasing amount of silica, resulting from the change in the effective refractive index (cf. Sect. 3.3.6 in Chap. 3). The utilization of the modified Bragg equation (Eq. 3.10)

$$\lambda_{\text{Bragg, theo}} = 1.63d\sqrt{0.74\chi_{\text{PS}}n_{\text{PS}}^2 + 0.74\chi_{\text{SiO}_2}n_{\text{SiO}_2}^2 + 0.26n_{\text{air}}^2} \tag{5.17}$$

delivers excellent agreement between the theoretically expected Bragg wavelengths $\lambda_{\text{Bragg, theo}}$ and the experimentally measured λ_{Bragg} as far as refractive indices a bit lower than for the bulk materials are assumed ($n_{\text{PS}} = 1.55$, $n_{\text{SiO}_2} = 1.37$ [43]).

Since the number ratio of PS and SiO$_2$ spheres in the composite is clear now, the next step is to remove the silica spheres by etching with hydrofluoric acid. Figure 5.6e–h shows the SEM pictures of the composite crystals after etching away the silica beads. The removed spheres appear now as randomly distributed hole defects in the colloidal crystal. From the SEM pictures it is obvious that for the chosen compositions the crystalline structure is not disturbed (e.g., by a collapse). Therefore, the filling fraction of the whole crystal is now simply given by 0.74 times the experimental ratio PS:(PS + SiO$_2$) before the etching.

After infiltration with PDMS, the polarized Brillouin spectra are measured by BLS in the long wavelength limit. The results are displayed in Fig. 5.7. All signals increase linearly with q with increasing slope for increasing ratio PS:SiO$_2$ before the etching, i.e., with increasing filling fraction, which is expected due to the higher c_l of bulk PS compared to bulk PDMS. For all samples, c_{eff} is calculated from the linear fits as $c_{\text{eff}} = 2\pi df/dq$.

The experimental c_{eff}, c_{exp}, is compared to theoretical predictions of the EMT in Table 5.3, utilizing the real filling fractions ϕ from the experimental ratio in

Fig. 5.7 Dispersion at low qs and c_{eff} for defect doped PS opals infiltrated with PDMS
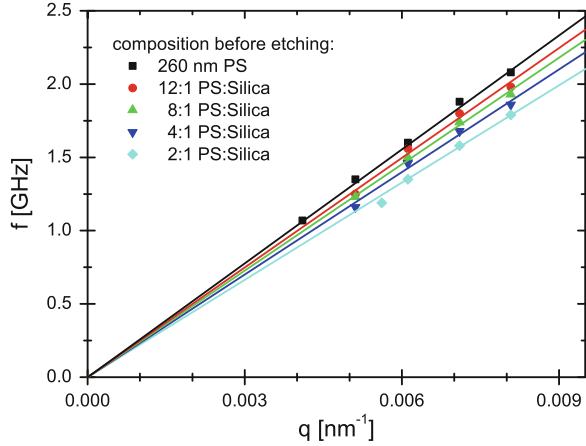

Table 5.2. First, the velocities are compared to the results of Wood's simple law, using the standard elastic parameters for PS and PDMS (given under the table). Interestingly, c_{Wood} seems to capture the experimental values quite well within a non-systematic error of 1.5% or less, which is in the range of the error of ϕ. Using the same parameters in the algorithm of Gaunaurd and Wertman ($c_{GW,s}$) leads to a significant deviation from the experimental values between 6% and more than 9%, while the deviation increases systematically for increasing ϕ.

Anyhow, it is possible to bring the results of their EMT in better accordance with the experimental results when taking $c_l(PS)$, $c_t(PS)$, and $c_l(PDMS)$ as fit parameters in a mean square fit for all five filling fractions. So the $c_{GW,f}$ are obtained, keeping the parameters in relatively reasonable ranges. The PDMS is assumed to be about 8% softer (1,109 ms^{-1} instead of 1,200 ms^{-1}), for the PS the transverse sound velocity must be chosen smaller (1,100 ms^{-1} instead of 1,200 ms^{-1}) and the longitudinal one must be chosen higher (2,470 ms^{-1} instead of 2,350 ms^{-1}). Doing so, the error stays within about 1%, however changing systematically from a little to high values for low ϕ to a little to low values for the undoped crystal. Even better results can be achieved using really free fit parameters without any fitting ranges.

Table 5.2 Characterization of the PS:SiO$_2$ composite colloidal crystals

Initial ratio PS:SiO$_2$	Experim. ratio PS:SiO$_2$	Mass loss[a] (%)	$\lambda^{b}_{Bragg, theo}$ (nm)	λ_{Bragg} (nm)
0:1	0:1	–	533.7	530.0 ± 7.9
2:1	2:0.8	60.7	588.3	586.0 ± 1.6
4:1	4:0.8	75.5	595.3	593.0 ± 3.6
8:1	8:0.8	86.1	599.7	599.0 ± 0.8
12:1	12:0.8	90.3	601.4	601.5 ± 0.5
1:0	1:0	–	605.0	602.1 ± 3.3

The initial ratio is also the name of the samples in Figs. 5.6 and 5.7
[a] $\varrho_{PS} = 1.05$ g cm^{-3}, $\varrho_{SiO_2} = 1.7$ g cm^{-3}, $d_{PS} = 260$ nm, $d_{SiO_2} = 255$ nm
[b] $n_{PS} = 1.55$ g cm^{-3}, $n_{SiO_2} = 1.37$ g cm^{-3}, $d = 260$ nm

Table 5.3 Comparison between experimental effective longitudinal sound velocities and results from Wood's law and the EMT of Gaunaurd and Wertman using standard and fitted parameters (in ms^{-1})

PS:SiO$_2$	ϕ	c_{exp}	c_{Wood}	$\Delta/\%$	$c_{GW,s}$	$\Delta/\%$	$c_{GW,f}$	$\Delta/\%$
2:1	0.529	1,382	1,362	−1.5	1,304	−6.0	1,395	1.0
4:1	0.617	1,464	1,451	0.9	1,372	−6.7	1,473	0.6
8:1	0.673	1,522	1,520	0.1	1,421	−7.1	1,530	0.5
12:1	0.694	1,567	1,548	−1.2	1,441	−8.7	1,553	−0.9
1:0	0.740	1,627	1,617	−0.6	1,488	−9.3	1,609	−1.1

Constant: $\varrho(PS) = 1,050$ kg m^{-3}, $\varrho(PDMS) = 965$ kg m^{-3}, $c_t(PDMS) = 0$ ms^{-1}; c_{Wood}, $c_{GW,s}$: $c_l(PS) = 2,350$ ms^{-1}, $c_t(PS) = 1,200$ ms^{-1}, $c_l(PDMS) = 1,050$ ms^{-1}; $c_{GW,f}$: $c_l(PS) = 2,470$ ms^{-1}, $c_t(PS) = 1,100$ ms^{-1}, $c_l(PDMS) = 1,109$ ms^{-1}

However, the best fit is achieved with unreasonable parameters, especially for PS ($c_l(PDMS) = 1,069$ ms^{-1}, $c_l(PS) = 2,622$ ms^{-1}, and $c_t(PS) = 1,082$ ms^{-1}).

In summary, it can be said that for different filling fractions the investigated colloidal system shows the expected trend in the effective medium sound velocity. The increase in c_{eff} with increasing amount of the harder component was predicted qualitatively by Wood's law as well as by the more elaborated EMT of Gaunaurd and Wertman, developed for the special present case of spheres embedded in an elastic or fluid matrix. However, while the predictions utilizing Wood's law agree also quantitatively well with the experimental results, there is a systematic deviation to the velocities calculated by the other EMT. The reason of the deviation is unclear. It might originate in a kind of size or frequency effect that leads to deviations for small spheres (possibly originating from elastic confinement inside the spheres) or for high frequencies. Anyhow, these assumptions are somehow speculative.

5.3 Band Gaps in Polymer Opals and Disordered Systems

5.3.1 The Influence of the Order in Colloidal Systems

Structured materials with a periodic modulation in the density and elastic coefficients, so-called phononic crystals [11], can exhibit phonon band gaps at Bragg frequencies or wavelengths commensurate to their lattice constant. In addition to Bragg gaps (BG), theory predicts gaps evoked by resonance modes of the constituent components interacting with the extended acoustic branch of the composite structure [45]. These gaps prevent elastic waves with certain frequencies to propagate through the crystal at least in certain crystallographic directions. The width and the position of the BG in general depends on the contrast between the densities (ϱ), longitudinal and transverse sound velocities (c_l and c_t) of the component materials, and on the lattice parameter [9, 10, 33]. Yet, structures with strong localized resonant elements can shift the gap well below the Bragg frequency associated to the lattice constant [8, 46]. Soon after the first

experimental observation of ultrasonic band gaps [4–6, 8, 13], peculiar phenomena with potential applications dealing with the propagation of elastic waves in periodic composite materials such as tunneling [47], negative refraction, focusing [48, 49], and enhanced transmission through 1D gratings [15] have been discovered. Earlier realized systems with periodicity in the millimeter range deal with sonic and ultrasonic frequencies [5–8, 13, 46–49], while periodic patterns at the submicrometer scale becomes necessary to shift the gap to hypersonic frequencies [18, 50]. The phononic dispersion relation of such a single crystalline pattern created by vertical lifting deposition of polymer colloids and measured by BLS led to the first observation of a hypersonic BG along high-symmetry crystallographic directions [17]. By varying the particle size and the infiltrated fluid, the hypersonic frequency and the width of the gap could be tuned. More recently, a hypersonic BG was also observed in 2D structures fabricated by optical lithography [36].

In soft opals, the spherical particles represent local resonant elements and hence the bands, which originate from the multipole modes of these interacting particles, can overlap with the acoustic field of the extended states in the effective medium. As a result of this hybridization, a gap opens up in the vicinity of the eigenfrequency of the quadrupole particle modes [45], which is referred to as hybridization gap (HG). Albeit there was a hint of this HG in colloidal suspensions [25, 39, 40, 51], its demonstration, assignment and the concurrent observation along with the BG has been missing. In this section, the first realization of a double phononic gap in *fcc* colloidal crystals formed by colloidal self-assembly during vertical lifting deposition with subsequent fluid infiltration is presented [52]. The effect of the elastic contrast between the fluid matrix and solid inclusions as well as the crystalline order of the structure on the two gaps is distinct. Furthermore, in amorphous colloidal glasses, only the HG persists.

The fabrication of the colloidal films starts with the deposition of the particles by vertically lifting a glass substrate from the aqueous colloid suspension [53]. For different experiments, two kinds of monodisperse polystyrene (PS) spheres with diameters of $d = 307$ and 360 nm and poly(methylmethacrylate) (PMMA) particles with a diameter of $d = 327$ nm were used for the fabrication of the opals. Additionally, a noncrystalline hybrid film consisting of PS sphere mixture with two different diameters (300 and 360 nm) was prepared in the same way. After complete drying, the films were infiltrated with liquid poly(dimethylsiloxane) (PDMS) and any liquid excess was blown off (Fig. 5.3). By this method uniform wet colloidal films with a thickness of about 10 μm were obtained. The phononic dispersion relation was measured by BLS for the dry and liquid infiltrated state of these films. BLS probes the thermal phonon propagation in the sample along a selected direction determined by the transmission scattering geometry adumbrated by Fig. 5.8 (cf. appendix) [17]. For the given experimental conditions, the scattering wave vector of the photon lies in the (111) plane of the *fcc* lattice and its amplitude $q = (4\pi/\lambda)\sin(\theta/2)$ depends on the scattering angle θ and the wavelength of the incident laser beam λ. At low q values for which the system appears homogeneous, the wave vector of the phonon $\mathbf{k}$ and that of the inelastically scattered light $\mathbf{q}$ are equal. Under these conditions, the BLS spectrum at a given q consists of a doublet

Fig. 5.8 BLS parallel to the substrate in a colloidal crystal
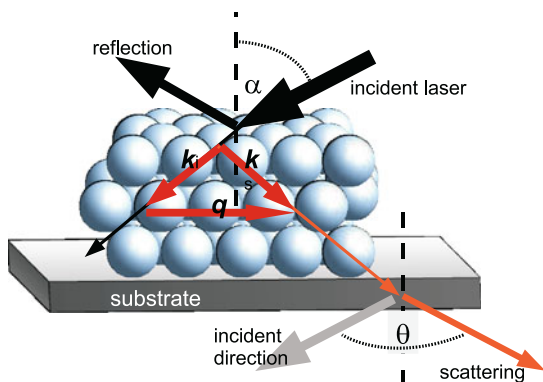
with a Doppler frequency shift $\omega = \pm ck$, where c is the speed of sound with longitudinal (or transverse) polarization in the effective medium (e.g. lowest spectrum in Fig. 5.10, cf. Sect. 2.3 in Chap. 2).

The precursor dry PS and PMMA opals have a highly ordered crystalline morphology as indicated by the SEM image in Fig. 5.9. The single crystalline order extends over a few hundred micrometers. The dry films exhibit strong multiple light scattering due to the large optical contrast between the particles and the surrounding air and due to the particles elastic form factor. The wave vector **q** is, therefore, ill-defined which precludes the measurement of the dispersion relation $\omega(\mathbf{q})$. Nonetheless, the BLS spectrum of the dry opals reveals several localized (q-independent) modes [54, 55]. As discussed in Chap. 4, these are identified as
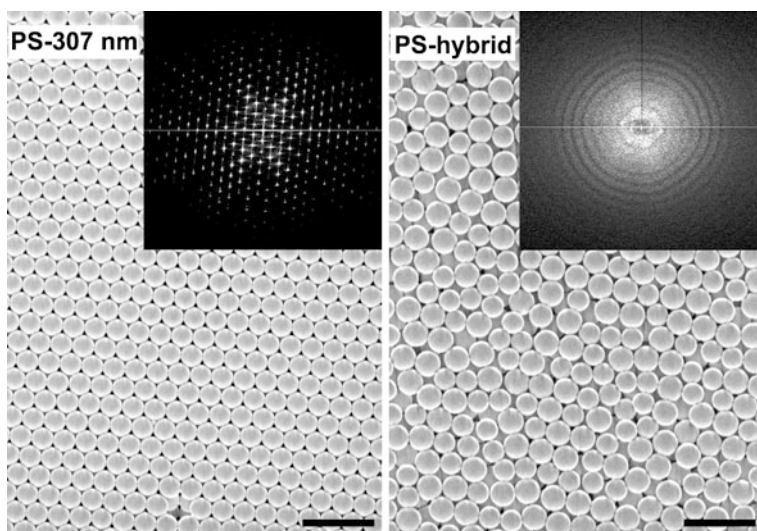
Fig. 5.9 SEM *top-view* images of the PS-307 crystal (*left*) and the PS-hybrid (*right*)—both "dry" before infiltration (*scale bar* is 1 μm). The *insets* display the Fourier-transform images computed from the SEM pictures over an area of about 4 by 4 μm [26]

Table 5.4 Sound velocities, particle sizes and lowest eigenfrequencies in colloid-based phononics

Material	c_t/ms^{-1}	c_l/ms^{-1}	d/nm	$f(1, 2)$/GHz	c/ms^{-1}
PS	$1{,}200 \pm 30$	$2{,}350 \pm 50$	307	3.3[a]	
			360	2.9[a]	
PDMS	0	$1{,}050 \pm 20$[a]			
PS/PDMS		$1{,}670 \pm 30$[a]	307	2.2[b]	1,490[b]
		$1{,}570 \pm 30$[a]	360	1.9[b]	1,490[b]
Hybrid/PDMS		$1{,}510 \pm 20$[a]	300/360		1,400[b, c]
PMMA	1400 ± 40	$2{,}800 \pm 50$	327	4.0[a]	
PMMA/PDMS		$1{,}720 \pm 30$[a]	327	2.3[b]	1,560[b]

Densities ϱ (kg/m^3): PS: 1050, PMMA: 1,190, PDMS: 965
[a]Measured by BLS
[b]Computed for the wet opals
[c]For 65% filling fraction of spheres

vibration eigenmodes of the particles and each mode can be specified by a pair of indices (n,l) defining the lth spherical harmonic of the nth radial mode. The frequencies of these sphere eigenmodes depend on the size of the particle, the mass density and the speed of sound in air and in the particle for both polarizations (i.e. compression and shear moduli). Consequently, the mechanical properties of the samples can be reliably determined from the theoretical fit of the experimental eigenfrequencies. The obtained longitudinal and transverse sound velocities in the two types of particle materials along with the lowest $f(1, 2)$ eigenfrequency are given in Table 5.4. For the particles embedded in the infiltrated PDMS, the eigenfrequencies can be theoretically computed using the elastic parameters of Table 5.4 [51, 56]. Expectedly, $f(1, 2)$ decreases when the spheres are embedded in PDMS.

The infiltration of the thin dry opals by PDMS with a refractive index ($n = 1.45$) close to that of the PS particles ($n = 1.59$) diminishes multiple light scattering and hence **q** is well defined. To obtain the desired dispersion relation $\omega(\mathbf{q})$, the BLS spectra of the wet opals were recorded along the high-symmetry directions of the reciprocal space. In the present case of the *fcc* lattices, the first Brillouin zone (BZ) is a truncated octahedron (Fig. 5.5). The experimental **q** is confined in the hexagon formed by the intersection of the (111) plane with the BZ [17]. The direction of **q** is selected along Γ–M, where M is the edge center of the hexagon and the evolution of the BLS spectra with **q** near the BZ for the PS wet opal is shown in Fig. 5.10. The simple picture of single phonon propagation in the effective medium at low q values becomes complex as q increases towards the BZ boundary. Up to four Lorentzian curves are required to represent the experimental BLS spectrum. In contrast to the PS/silicon oil opal with a single peak splitting across the BZ boundary [17], the same opal infiltrated in PDMS providing higher elastic contrast displays richer spectral features and exhibits a second splitting at lower q values within the first BZ. The experimental dispersion relation is depicted in Fig. 5.11. In the hypersonic PS/PDMS crystal ($d = 307$ nm) only one longitudinal phonon branch is observed at low q values with $c_l = 1{,}670$ ms^{-1}, intermediate between the longitudinal sound

Fig. 5.10 BLS spectra of the wet opal of PS spheres with diameter 307 nm in a PDMS matrix at different wave vectors in the (111) plane of the *fcc* crystalline colloidal film. The edge of the BZ along the probed direction corresponds to $q_{BZ} \approx 0.013$ nm^{-1}. The deconvolution in different spectral components is indicated for the Stokes side of the spectrum. Each spectrum is normalized to the total integrated intensity, for comparison of the relative contributions [57]
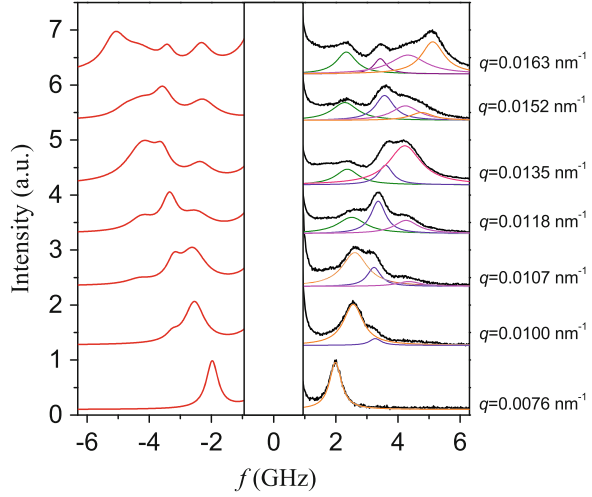
velocities in the pure component materials. Transverse phonons are not observed experimentally, probably PDMS cannot support shear waves and the mechanical contact between the particles is weakened. The most striking feature of the dispersion diagram is the simultaneous presence of two band gaps at about 3 and 4 GHz, respectively. The latter is clearly a BG since it occurs at the edge of the BZ, $q = q_{BZ} \approx 0.0133$ nm^{-1}, that matches the distance Γ–M, i.e. $(3/2)^{3/2}\pi/a$, where $a = \sqrt{2}d$ is the lattice constant of the given *fcc* crystal. An analogue behavior is observed in the second wet opal of the larger PS spheres ($d = 360$ nm) for which the gap positions shift to lower wave vectors and frequencies (open circles in the upper left diagram of Fig. 5.11).

Fig. 5.11 Phononic band diagrams for the different PS wet opals under consideration, along the Γ–M direction (see text). The *hatched bands* mark the phononic gaps and the *vertical arrows* indicate the q values in the corresponding spectra of Figs. 5.10 and 5.12. The *vertical lines* denote the first BZ limit (for $d = 307$ and $d = 360$ nm, respectively). The change in the DOS induced by the corresponding single PS particle in PDMS is shown in the *right-hand panel* [26]
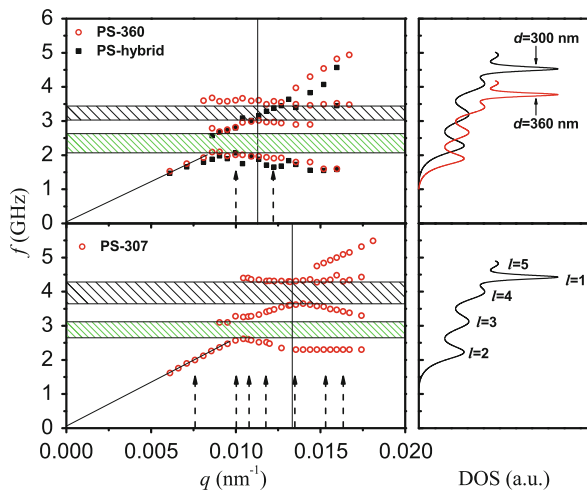
In order to elucidate further the nature of the two gaps, the effect of the crystalline order on the experimental band diagram was examined. The formation of a hybrid colloidal film consisting of a mixture of an equal number of two PS spheres ($d = 300$ nm and $d = 360$ nm) artificially broadens the size distribution beyond the polydispersity limit of about 5% necessary for crystallization [44]. Indeed, the crystallization is prohibited in this hybrid colloidal film, as indicated by the lack of a long-range order in the right-hand panel of Fig. 5.8, leading to an amorphous colloidal glass. The BLS spectra of the infiltrated monodisperse opal and hybrid films are shown in Fig. 5.12 for two wave vectors. The deletion of one peak in the spectrum of the hybrid is due to the disappearance of the BG in the disordered hybrid, as it is clearly shown in the dispersion plot in the upper left diagram of Fig. 5.11 (solid squares). Apparently, the crystalline order is a prerequisite for the BG but not for the newly observed lower frequency HG, which is omnidirectional in the colloidal glass. An identification of the latter as a theoretically anticipated HG [45], through density-of-states (DOS) calculations [56], is examined in Fig. 5.11. The right-hand panel of Fig. 5.11 displays several eigenmodes of the individual PS spheres embedded in the fluid PDMS. The lowest $f(1, 2)$ appears to compare well with the frequency at the crossing with the acoustic branch and the opening of the HG. Moreover, the lowest frequency points at the experimental dispersion at high qs compare very well with the computed $f(1, 2)$. This and the two higher flat bands of localized modes in Fig. 5.11 cause sufficiently strong inelastic light scattering at high qs [51] and compare well with the particle resonances of higher l. Their presence in the BLS spectra obscures the resolution of the phonons in the second BZ. Interestingly, the bands originating from particle resonant modes appear to be considerably narrower and occur at higher frequency than theoretically predicted [45]. This can be ascribed to viscous losses in the liquid matrix that were not taken into account in the theoretical calculations, and which weaken the interparticle interactions as a result of the reduced overlap between the corresponding wave fields. Qualitatively, the opening of the two gaps is also observed in a third wet opal of PMMA with $d = 327$ nm in PDMS (Fig. 5.13). The HG occurs at 2.5 GHz, very close to the $f(1, 2) =$

Fig. 5.12 Exemplary BLS spectra of the PS ($d = 360$ nm)/PDMS wet opal (*bottom*) and the wet PS-hybrid colloidal film (*top*) at two q values indicated by the *arrows* in the corresponding diagram of Fig. 5.11. The deconvolution into different spectral components is shown below each spectrum (note the absence of the BG-induced spectral features in the hybrid) [26]
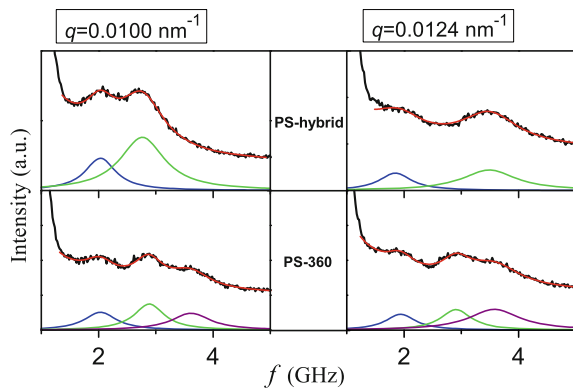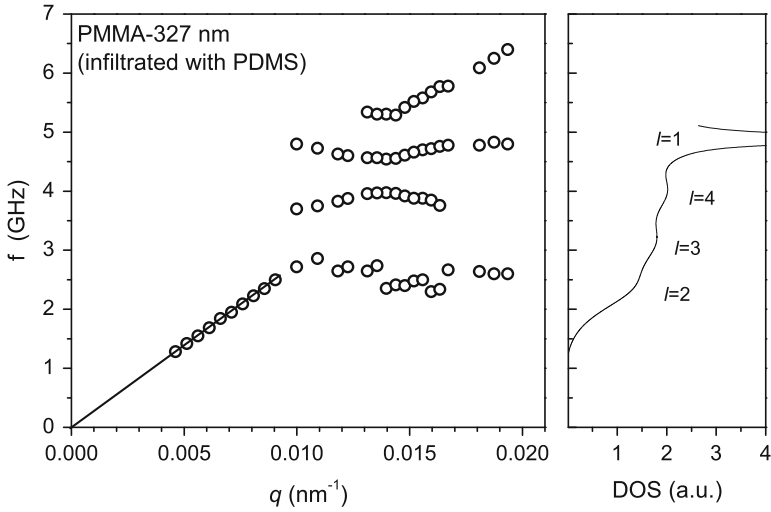
Fig. 5.13 Phononic band diagrams for PMMA wet opals in PDMS with $d = 327$ nm, along the Γ–M direction. The change in the DOS induced by the corresponding single PS particle in PDMS is shown in the *right-hand panel* [26]

2.35 GHz of this particle in PDMS, whereas the wet opal exhibits a sound velocity of $1{,}720 \pm 30$ ms^{-1} in the long-wavelength limit (Table 5.4).

It is worth noting that the various effective-medium theories (EMT) yield sound velocities about 10% smaller than the experiment [31, 37], even if the viscosity in the liquid matrix is taken into account. On the other hand, if one considers the colloidal film as a polymer (solid) matrix with fluid inclusions [37], EMT strongly overestimates the sound velocity. The above, in view also of the fact that measured sound velocities agree generally well with the results of EMT in non-close-packed colloidal crystals [58], suggests the existence of consolidation, at least to some degree that may be different for different samples, in the colloidal films [59]. This also explains why the measured effective sound velocity is different in the two PS/PDMS crystals (see Table 5.4).

In conclusion, this work presents, for the first time, the discovery of two phononic band gaps of different nature coexisting at hypersonic frequencies in the same physical system and elucidated the underlying physical mechanisms. Induced disorder did not destroy the newly demonstrated HG. This study has been possible by taking advantage of the opportunities offered by the colloidal science to tailor the phononic band diagram of nanostructured materials, measured directly by BLS. Manipulating the flow of phonons may allow heat management, e.g. in thermoelectrics. Finally, it was pointed out the need of a detailed quantitative evaluation of the dispersion diagrams of colloid-based phononic structures, by means of full elastodynamic calculations that take into account consolidation and soft matter properties (e.g. structural dynamics of the component materials or interfacial effects), which still remains an open challenging theoretical problem.

### 5.3.2 The Influence of the Composition in Disordered Colloidal Systems

In Sect. 5.3.1 the realization of a hybridization gap (HG) was presented for monodisperse colloidal crystals as well as for disordered 'hybrids', e.g., for the 1:1 number ratio 300:360 nm PS hybrid in Fig. 5.11. However, when discussing the HG at that point, the mixing of two different sizes of colloids was only mentioned in order to introduce structural disorder, i.e., to destroy the colloidal crystal, but the influence of the composition on the position of the HG was not elucidated. Indeed, in the top panel of Fig. 5.11 it seems that the HG for the pure 360 nm opal and the 1:1 hybrid come more or less at the same position. In this section, an experiment is presented in which the number ratio of two kinds of PS colloids with clearly different size (180 and 360 nm) is varied in a wide range. The HG for these systems infiltrated with PDMS is observed and the changes in width and position are discussed; of particular interest is the question if it is possible to tailor this band gap by simply controlling the size composition of the particles.

The set of samples has been realized by Retsch mixing distinct amounts of 180 nm PS beads and 360 nm PS beads in aqueous dispersion and preparing the hybrids by vertical lifting deposition under continuous stirring in order to guarantee the homogeneous distribution of both particles in the whole sample. Doing so, hybrids with composition between 1:1 and 40:1 180:360 nm particles number ratio have been prepared, i.e., the volume ratio varied between 1:8 and 5:1 for the smaller particles compared to the larger ones. After infiltration with PDMS, BLS was performed in transmission geometry and the dispersion relation was obtained fitting the spectra with Lorentzians in the q-range between about 0.006 and 0.020 nm^{-1}. The result is shown in Fig. 5.14.

Figure 5.14 contains the experimental band diagrams for the mentioned systems as well as for bare 180 nm PS particles. The position of the HG is marked by colored rectangles. Note that for all systems only one HG between ≈ 4 and 5.5 GHz was found in the experimentally accessible range, only for the 1:1 hybrid, a second HG was observed between ≈ 2 and 2.5 GHz. By comparison with the HG from the bare 180 nm PS particles and taking into account the scaling of the HG with $1/d$, it is obvious that this gap originates (mostly) from the 360 nm particles. The 1:1 hybrid is the only one whose volume fraction of the larger particles exceeds that of the smaller spheres. Anyhow, in the rest of this section, I want to focus on the higher frequency HG above 4 GHz.

Indeed, when comparing the HGs of the bare 180 nm particles and of the hybrids, one finds that the HG for every hybrid is shifted to lower frequencies in a mostly systematic way. The higher frequency HG of the 1:1 hybrid is distinctly lower and smaller than that of the opal. With increasing amount of 180 nm particles in the mixture, the gap widens up and is shifted to higher frequencies. This is true at least for the 9:1 and the 20:1 hybrid, the 40:1 hybrid, however, seems to contradict the trend, although its HG is still broader and at clearly higher frequency than that of the

Fig. 5.14 Development of the HG in binary PS hybrids infiltrated with PDMS as a function of the composition. The *colored rectangles* mark the HGs for the different systems. The *empty black rectangle* corresponds to the HG from the 180 nm PS opals after correction for effective sound velocity. The *light red rectangle* around 2.5 GHz for the 1:1 hybrid belongs to the HG originating from the larger spheres
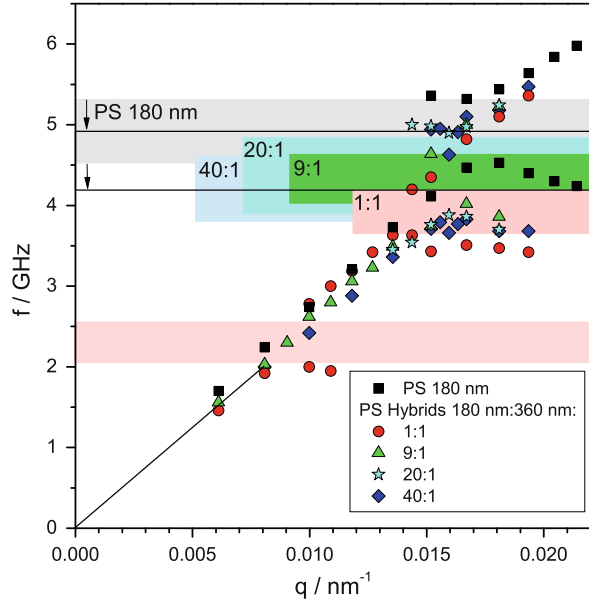
1:1 hybrid. On the other hand, when ignoring the lowest point in the upper branch of the 40:1 sample, also this sample would follow the trend.

When comparing the opal with the hybrids, one should note that for an *fcc* colloidal crystal of course the filling fraction ($\phi = 0.74$) is different than for a disordered system. Approximating a uniform filling fraction of $\phi = 0.65$ for all hybrids [60], which is admittedly a bit arguable especially for the extreme ratios, one can estimate that for the infiltrated opal the effective longitudinal sound velocity c_{eff} should be higher by about 6.3 or 8.5%, applying the EMT of Gaunaurd and Wertman [31] or Wood's law [30], respectively (cf. Sect. 5.2)—in reasonable agreement with the experimental c_{eff}. Since the position of the band gaps scales with c_{eff}, it is possible to normalize the frequencies by that. Doing so, also the HG of the 180 nm opals is shifted towards somehow lower frequencies, still following the trends mentioned above. In Fig. 5.14 the normalized (relative to the amorphous systems) HG of the PS 180 nm opal is symbolized by the open black rectangle.

To rationalize the findings in this experiment one must go back on the nature of the HG (Sect. 5.3.1). The HG originates from the level repulsion between the bands of the linear acoustic mode and those from localized modes, i.e., the eigenvibrations inside the spheres. The generation of a band originating from these eigenvibrations can be described in analogy to the tight coupling method for the electronic states in solids, in which the overlap of atomic orbitals is assumed to be sufficient to require corrections of the picture of the isolated atom, but not so much to render the atomic description completely irrelevant [29]. This theory predicts that in a sample of *N* atoms each electronic state consists of an *N*-fold degenerated level. If the atoms come closer together, i.e., if their wave functions overlap

significantly, the levels broaden up into bands. In the analogy of the phononic system, the individual spheres play the role of the atoms, and instead of electronic wave functions one deals with the acoustic resonance modes of the spheres (as 'acoustic wave functions'), which are both described by the same mathematics (cf. Sect. 2.3.3 in Chap. 2).

This means that in order to obtain a strong band, the spheres must be in close contact to each other and the acoustic wave function must overlap with that of the next neighbor. Since the spheres are close-packed (or randomly close-packed) in all cases, bands can be assumed. The question is how do modes of the same type but from different particles sizes interact with each other. From symmetry considerations, there is no reason for them not to interact, i.e., to hybridize. However, if their energy levels are too different, they should be not able to interact anymore. Anyhow, in the present experiment the frequency of the gaps is shifted, which is a hint on a shift of the position of the resonance band [in this case of the (1, 2)-mode], too. The most reasonable explanation is that, although there is a significant difference in energy for 180 and 360 nm spheres, the (1, 2) modes of the 180 nm spheres couple with those of the 360 nm spheres, leading to shift to lower frequencies with increasing fraction of the 360 nm spheres wave function.

On the other hand, the coupling seems to be weak enough to allow two HGs for the 1:1 hybrid. Since the higher frequency HG is clearly shifted towards lower frequency, it is obvious that there cannot be two fully decoupled bands, at least there must be some influence of the bigger spheres on the localized mode of the smaller spheres. For lower number ratios of the larger spheres the low frequency HG completely disappears, which is another hint for the rightness of the conclusion that this gap must originate from the 360 nm particles, which are too separated in the other hybrids to interact effectively. The smaller width especially for the 1:1 hybrid can be rationalized by the larger average sphere to sphere distance of the small spheres in the sample.

In summary, one can conclude that the experiment can be principally captured qualitatively by simple hybridization considerations. However, there are still open questions that could only be solved with additional experiments and—even more needed—strong theoretical support. From this section, I would like to retain the message that the distribution of colloids of different size has an influence on the hybridization gap. Under certain circumstances, the mixing of particles of different sizes may be a way on which future studies to tailor the band gap could proceed.

5.4 Band Gaps in SiO_2 Colloidal Systems

In the previous sections of this chapter it was shown that the elastic contrast between matrix and scatterers is crucial for phononic phenomena. Another important role is played by the density contrast, which is, however, usually quite weak for polymer/liquid systems. In this section, experiments on silica colloids in liquid or elastic matrix are shown, i.e., the elastic contast is relatively high as well

as the density contrast is. In such systems, additional effects can be found that cannot be fully captured by theory (and the explanations in the previous chapters), yet.

5.4.1 Phononic Behavior of Silica Suspensions

In Sect. 4.2.4 (Chap. 4) a system consisting of dense packed silica spheres in an index-matching liquid ethoxy-ethoxyethyl acrylate (SR256) matrix was introduced to show the q-dependence of the light scattering intensity of the particles eigenmodes. Since the eigenmodes appear at high f compared to the longitudinal acoustic branch, there was no need to go into the development of the acoustic behavior on that point. However, since, in first approximation, the acoustic branch in Fig. 4.12 in Chap. 4 appears to be linear, a more detailed investigation of the dispersion relation of the acoustic mode shows some surprising details, which will be presented in this section.

The investigated materials are the sample presented already in Sect. 4.2.4 (Chap. 4, $d = 375$ nm) as well as an analogue sample with $d = 219$ nm silica spheres. The samples have been synthesized by Kiefer at DKI with an initial concentration (filling fraction) of $\phi = 0.34$. A dense packing ($\phi = 0.74$) was achieved by ultra-centrifugation on the bottom of an NMR-tube (see also Fig. 1.3b in Chap. 1).

Figure 5.15 shows ten exemplary spectra for the dense packed sample of $d = 375$ nm spheres in the range $30° \leq \theta \leq 75°$, i.e., 0.009 nm$^{-1} \leq q \leq 0.020$ nm^{-1}, recorded at low free spectral range. In this q-range, the general shape of the observed signal changes dramatically. Since at the lowest angles the signal is clearly a single peak, the signal broadens rapidly with increasing angle. Furthermore, between $30°$ and $\approx 50°$ the frequency of the signal is virtually unshifted (dashed line), and only the linewidth Γ increases. At higher angles, $f(q)$ is not longer constant and the frequency increases again with q, although the signals remains extremely broad.

The corresponding dispersion relation is shown as open triangles in Fig. 5.15c. For the lowest qs, the acoustic signal behaves as an effective medium with $c_{\text{eff}} \approx c_{\text{SR256}}$. For comparison the pure SR256 is shown as gray squares (with linear fit). From about $q = 0.008$ nm^{-1} the dispersion relation shows an abrupt bending, the effect that is seen in panel a. At $q \approx 0.015$ $f(q)$ increases again. Although the absolute values for $f(q)$ at high qs, due to the large Γ, depend on the chosen limits of the fitting range, the trend is clear and looks for an unchanged fitting range as presented in Fig. 5.15c: $f(q)$ increases monotonically and linearly again, and the slope $\partial f / \partial q$ is essentially the same as that of the longitudinal phonon in the matrix (second linear fit).

An akin dispersion relation is obtained for the smaller silica spheres with $d = 219$ nm. However, the bending starts at higher qs and the second linear range must be expected at qs beyond the range measurable by BLS. In fact, the position of the bending scales with d^{-1}, and it appears about π/d.
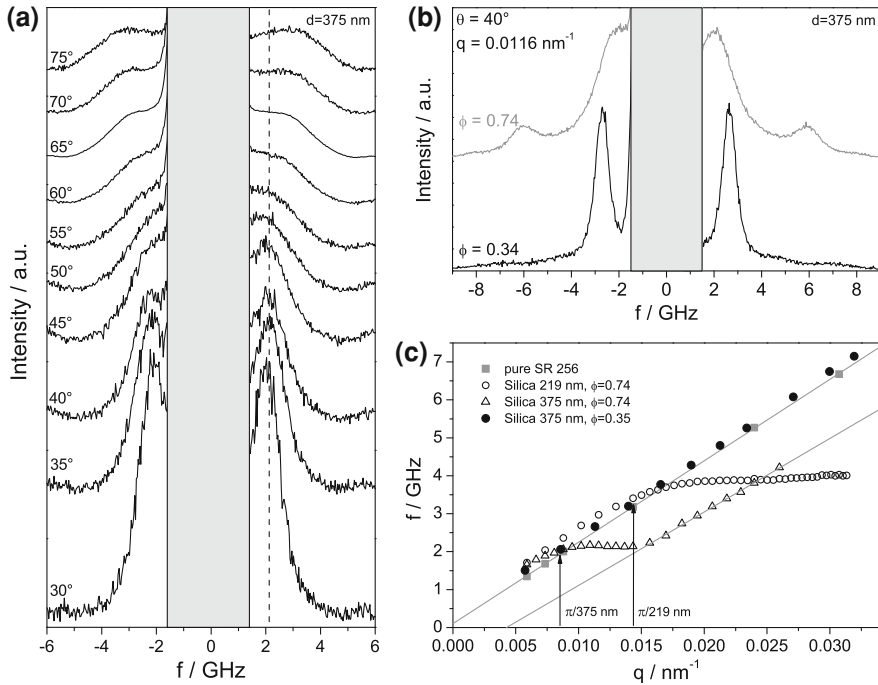
Fig. 5.15 a Development of the acoustic signal in the BLS spectrum of $d = 375$ nm silica spheres in SR256 ($\phi = 0.74$) for $30° \leq \theta \leq 75°$. **b** Exemplary spectra at $\theta = 40°$ for low ($\phi = 0.34$) and high ($\phi = 0.74$) filling fraction. **c** Experimental dispersion relations for dense packed silica spheres with $d = 219$ or 275 nm in SR256. For comparison also pure SR256 as well as silica with $d = 375$ nm and $\phi = 0.34$ are shown

The appearance of the bending requires high filling fraction, since the suspension with $\phi = 0.34$ (black circles) shows only the effective medium acoustic phonon, which appears at slightly higher frequencies than for the pure matrix. This is expected by effective medium theory (cf. Sect. 5.1.2) since the density of the silica inclusions is much higher than that of the matrix. The high density contrast leads to a strong scattering of the phonons on the hard spheres; i.e., the phonons travel mostly through the liquid matrix, and hence, c_{eff} is nearly the same in both cases.

Correspondingly, the linewidth at a given q is smaller for lower filling fraction as is shown for one exemplary angle ($\theta = 40°$) in Fig. 5.15b. Γ is inversely proportional to the phonon lifetime. If the phonon path is disturbed by many scatterers, the phonon lifetime decreases drastically. In fact, if $\Gamma \approx f$, as it is found at higher qs for $\phi = 0.74$, the free phonon pathlength is akin to the phonon wavelength; i.e., the phonon cannot travel anymore within the medium (the group velocity is zero), the system is overdamped. However, at higher qs the group velocity comes back to its value before the damping.

If one wants to summarize the experimental findings, one should start with the fact that there is no band gap. At a certain q-range the group velocity becomes

zero, however, there is no forbidden f-range. Since the centrifugated sample is polycrystalline, the lack of a Bragg gap is not surprising. On the other hand, it is noteworthy that the bending occurs at π/d, which means q equals the shortest intersphere distance of touching spheres. Anyhow, higher qs within the bending correspond to even shorter distances, while other crystallographic directions correspond to $q < \pi/d$.

The lowest particle eigenmodes are found at clearly higher frequencies (≈ 5 GHz for the $d = 375$ nm particles, Sect. 4.2.4 in Chap. 4). Therefore, it can be excluded that the bending originates from a localization of the phonon in the individual spheres, similar to HG (Sect. 5.3.1). On the other hand, a localization in the liquid 'voids' between the spheres is unlikely, since the liquid forms a continuous matrix, hence, there are no closed cavities to apply standing-wave conditions. Also the interpretation of the the cavities as open Helmholtz resonators (similar to those in musical instruments and subwoofers) seems to be not adjuvant [45, 61].

Another possible explanation for strong localization that does not require a periodic structure, but, moreover, has 'large' disorder as a precondition, is the Anderson localization of sound [62, 63]. Only recently, John Page and coworkers could show the realization of the localization of ultrasound in a three-dimensional elastic network consisting of disordered, sintered, monodisperse aluminum beads [64]. However, the theoretical treatment of Anderson localization is extremely demanding. Furthermore, it must be challenged that there is enough disorder in the polycrystalline samples. In addition, in Page's experiment a band gap for certain frequencies was found, which is not the case in the experiment presented here.

The bending must correspond to the appearance of a flat band in the theoretical band diagram due to the folding of bands in an *fcc* lattice [65]. An underlying symmetry can, theoretically, lead to the degeneracy of bands in the theoretical band diagram. The perturbation introduced by actual scatterers in the theoretical lattice may remove this degeneracy, leading to non-degenerated flat bands, which can interact with the acoustic band. In fact, layer multiple scattering calculations performed by Stefanou and Gantzounis at University of Athens [66], can capture the experimental band diagram quite well. Figure 5.16 shows the calculated phononic band structure for an *fcc* crystal of the given materials along two distinct crystallographic directions together with the normalized experimental points. The theoretical band diagram describes nicely the long wavelength limit, but there is also a flat band expected, which agrees with the flat band observed by BLS. However, there should be clear band gaps, which are not found in the experiment, which is most probably caused by a certain directionality in the band gaps, which is not fulfilled in the polycrystalline sample.

Although the band diagram can be quantitatively captured by theoretical calculations, the interesting question remains still unsolved: What is the origin of the flat band? As mentioned above, the explanation given for soft scatterers (Sect. 5.3.1) that the flat band corresponds to a tight-binding-like process from localized single particle modes, i.e., eigenmodes, is not suitable for this case, neither is the localization in single liquid cavities. Rather, the flat band must be
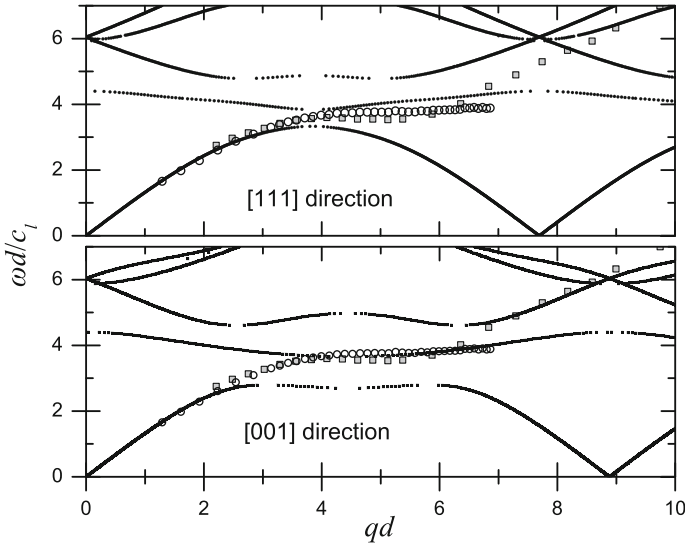
Fig. 5.16 Normalized theoretical band diagrams for *fcc* opals of SiO$_2$ spheres in SR256 matrix along two crystallographic directions. The experimental dispersion relations in Fig. 5.15 are shown as *circles* and *squares*

understood as a multiple-scattering effect. Its details, however, are still unclear and must be developed by theoreticians in the future towards a concrete, descriptive explanation.

5.4.2 Silica–Poly(ethyl acrylate) Films (PhoXonics)

Another realization of silica based phononic materials are melt compressed films with silica inclusions [22, 67, 68]. The technique of melt compression is presented in Sect. 3.2 in Chap. 3 When choosing silica–poly(ethyl acrylate) (PEA) core–shell particles as the starting materials, films can be pressed with different filling fraction of silica particles in a rubbery PEA matrix, i.e., with different spacing of the silica spheres in an *fcc* lattice.

In this section, the results of BLS measurements on several silica–PEA films is presented, with $d_{SiO_2} = 216$ or 253 nm. The total diameter of the initial core–shell particles was chosen between $d_{CSP} = 308$ and 498 nm, leading to filling fractions of $\phi = (d_{SiO_2}/d_{CSP})^3$ between $\phi = 0.08$ and 0.36 in the pressed films. The crystallographic orientation of the silica spheres in the pressed film is known to be an *fcc* lattice with orientation of lines of next neighbors in the radial direction from the center of the film [69]. Due to the melt compression, in the film the silica cores come nearer then in the initial opal, as is schematically shown in Fig. 5.17b. The shortest intercore distance becomes $(0.74)^{1/3}d_{CSP}$ along the direction marked by the white

arrow, which is also the main orientation of **q** in the following experiments. The corresponding lattice constant for an *fcc*-lattice is $a = \sqrt{2}(0.74)^{1/3} d_{CSP}$.

Figure 5.17a shows five exemplary spectra for such a silica–PEA film $(d_{SiO_2}/d_{CSP} = 253/387$ nm$)$ at different qs along the direction marked by the white arrow in panel b. The spectra are represented by a fit of one (lowest q) or two Lorentzian signals on the Anti-Stokes side. Around $q \approx 0.008$ nm^{-1} a band gap opens up. The corresponding band diagram is shown in Fig. 5.17c, normalized by the effective medium sound velocity c_{eff}, measured in the long wavelength limit,
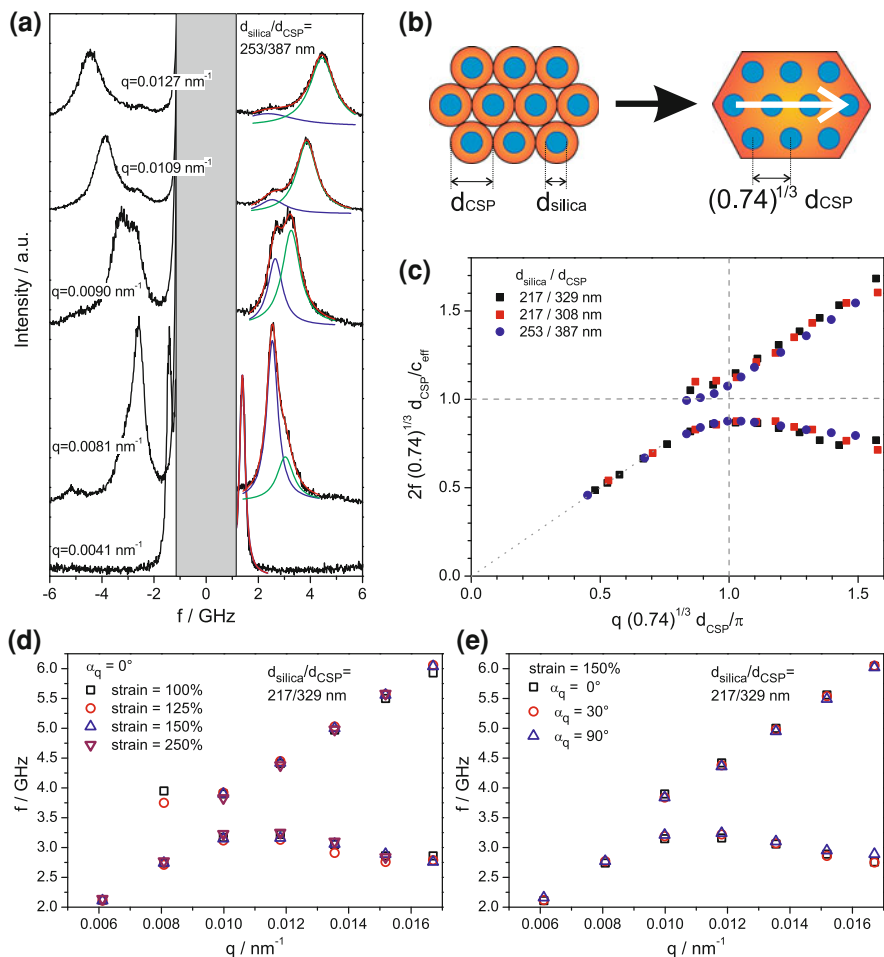
Fig. 5.17 **a** Experimental spectra for a melt compressed film $(d_{SiO_2}/d_{CSP} = 253/387$ nm$)$ at different qs, represented by Lorentzian lines. **b** Scheme of the result of melt compression (Sect. 3.2 in Chap. 3); the *white arrow* indicates the orientation of **q**. **c** Normalized dispersion relations for three different films. **d** Insensitivity of a melt compressed film (217/329 nm) to stretching **e** and the orientation of **q**

and by the intercore distance in the investigated crystallographic direction, which depends only on the initial total diameter of the core–shell particles (see above). The diagram contains also the normalized dispersion relations for two films with $d_{SiO_2} = 217$ and $d_{CSP} = 308$ and $329\,nm$. The dashed lines mark the q_{BZ}, the wavevector whose magnitude is half the diameter of the first Brillouin zone (BZ) along the observed direction, and the corresponding frequency. Obviously, a band gap is observed for all three films at the same normalized q and f, at the edge of the first BZ, hence it is a Bragg gap (BG) as introduced in Sect. 5.1.3.

The films compared in Fig. 5.17 have $\phi \geq 0.28$. In fact, also two films with significantly lower ϕ have been investigated, but neither for $\phi = 0.08$ nor for $\phi = 0.16$ a BG was found. These films show only a linear acoustic branch in the band diagram. These results demonstrate that a certain filling fraction is required to realize a BG, however, for sufficient elastic contrast, even with filling fractions much lower then in the crystalline case ($\phi = 0.74$) or the dense amorphous case ($\phi = 0.65$) (cf. Sect. 5.1.3), a relatively large BG can be realized. The comparison of the three band diagrams in Fig. 5.17c shows that the width of the gap increases systematically with increasing amount of silica in the continuous PEA matrix. Indeed, the ratio w of width of the band gap to its frequency is even higher for the melt flow pressed films ($w = 0.25$ for the 217/308 nm system with $\phi = 0.36$) than for the PS/PDMS opal presented in Fig. 5.11 ($w = 0.18$).

So far, a large BG at low filling fractions was presented in a handy, all solid material, but these results are basically not astonishing. However, additional, more elaborate experiments lead to results that elude the straightforward explanation of BG. Figure 5.17d shows the dispersion relation of the 217/329 nm sample for four different strains. The results were measured by BLS utilizing a stretching machine constructed by my colleague Nikos Gomopoulos. Surprisingly, it turned out that the dispersion relation is virtually unchanged from the unstretched (strain = 100%) film up to strains of 250%, i.e., films stretched to the two and a half fold of their initial length (strain = 250%), while the stretching is in the direction of **q**.

Theoretically, since the band gap is assumed to be a BG, one must expect that the gap scales inversely with the spacing between the spheres, as is also observed in Fig. 5.17c. However, when stretching the film, the distance of the spheres should also change accordingly. From light diffraction experiments on similar samples, also synthesized by DKI, it is experimentally proven that stretching clearly changes the intersphere distances [69]. In the direction of the strain, the distance between the spheres increases, while perpendicular to that the spheres come nearer together. Accordingly, also the BG should be shifted to lower frequencies, which is not the case within the experimental error, or, with other words, the gap is robust against structural variation. At high strains, it is even likely that the crystallographic order vanishes, since the spheres rearrange in a random way.

How can such robustness be explained? As was shown in Sect. 5.1.3, a hybridization gap (HG) originates from the individual scatterers properties. But the present band gap is for sure not a HG, since the position of the HG would

scale with $d_{SiO_2}^{-1}$ and not as observed with d_{CSP}^{-1}. Furthermore, the lowest eigenmodes of silica embedded in the PEA rubber should be not so different from those found in the liquid SR256 matrix in Sect. 4.2.4 in Chap. 4, which appear at clearly higher frequencies than the band gap does in the films. Additional to that, the evidence of the gap being a BG is striking. Not only the scaling with d_{CSP}^{-1}, but also the correct prediction of the gap position by theoretical consideration in the unstretched case, are clear proofs. Moreover, there is no reason why there should be no BG.

So, the open question remains why the gap does not react on the stretching. So far, there can be only speculation on this matter. A possible explanation might be that BLS is probing a kind of 'effective distance' between spheres, which is a somehow averaged value. Therefore, one must assume that the probed phonons are not only on a well defined path like in Fig. 5.17b, which might be explained by strong scattering by the silica spheres. Even at higher strain, the average distance between each two neighboring spheres does not change to much (in fact, it is a function of Poisson's ratio). On the other hand, this explanation seems not to be very satisfactory. If there would be very strong scattering, the phonon lifetime would decrease and the linewidth would increase drastically. Furthermore, an analogue band gap would have to appear also in the dense silica suspensions of Sect. 5.4.1, which is not the case. Therefore, instead of presuming to absurd theories, I would like to let the explanation of this effect as an open question. Additional experiments to determine the crystallographic behavior at high strains (e.g., AFM, TEM) and further theoretical support will be needed to solve this demanding problem in the future.

In summary, both investigated systems with hard silica spheres in soft liquid or elastic matrix show unprecedented phononic effects, which will challenge experimentalists and theoreticians. A dense packing of silica spheres in an index matching liquid shows an unseen dispersion relation with an intermediate flat band only for certain qs, which is probably a result of the folding of bands. In melt flow pressed films containing about 30 vol% of silica cores in a crystalline order, a band gap is presented that can be assigned as a BG. However, stretching of the film results in an unexpected robustness of the gap position, which cannot be explained satisfactory so far.

5.5 Materials

The synthesis of the polymer and silica colloids is already described in Sect. 4.4 in Chap. 4. Opals and disordered opals (hybrids) are obtained by vertical lifting deposition described in Sect. 3.1 in Chap. 3.

For the infiltration of opals shown in Fig. 5.3 silicon oil and PDMS made in house or purchased from Sigma Aldrich were used with no further purification. 2(2-Ethoxyethoxy) ethyl acrylate (SR256) used in the suspensions was purchased from Sartomer with no further purification.

5.5.1 Melt Compressed Silica–Poly(ethyl acrylate) Films

The preparation of the compression molded films is explained in Sect. 3.2 in Chap. 3. The synthesis of the initial core–shell particles was performed by my coworker Diana Kiefer at DKI, Darmstadt and is briefly described here [22, 67, 70].

The synthesis starts with the preparation of the silica core following the Stöber process and subsequent step-by-step growing as described in Sect. 4.4 in Chap. 4. The silica core's surface was functionalized by acryl silanes on which a thin ($\sim$5 nm) PMMA interlayer was crafted by emulsion polymerisation of methy methacrylate (MMA) together with some allyl methacrylate (ALMA) monomer, using sodium dodecylsulfate (SDS) as an emulsifier and ammonium peroxodisulfate and sodium dithionite as a redox initiator system. Finally the PEA shell was crafted onto the allylic double bonds of the ALMA, utilizing again SDS as emulsifier.

References

1. Yablonovitch E (1987) Phys Rev Lett 58:2059
2. John S (1987) Phys Rev Lett 58:2486
3. Joannopoulos JD, Johnson SG, Winn JN, Meade RD (2008) Photonic crystals: molding the flow of light, 2nd edn. Princeton University Press, Princeton
4. Martinez-Salazar R et al (1995) Nature 378:241
5. Montero de Espinosa FR, Jiménez E, Torres M (1998) Phys Rev Lett 80:1208
6. Vasseur JO et al (2001) Phys Rev Lett 86:3012
7. Liu ZY et al (2000) Phys Rev B 62:2446
8. Liu ZY et al (2000) Science 289:1734
9. Sigalas M, Economou EN (1993) Solid State Commun 86:141
10. Kushwaha MS, Halevi P, Dobrzynski L, Djafari-Rouhani B (1993) Phys Rev Lett 71:2022
11. Gorishnyy T, Maldovan M, Ullal C, Thomas E (2005) Phys World 18:24
12. Sheng P, Chan CTZ (2005) Z Kristallogr 220:757
13. Sanchez-Perez JV et al (1998) Phys Rev Lett 80:5325
14. Dobrzynski L et al (1999) EPL (Europhy Lett) 46:467
15. Lu M-H et al (2007) Nat Mater 6:744
16. Lin K-H et al (2007) Nat Nanotechnol 2:704
17. Cheng W et al (2006) Nat Mater 5:830
18. Gorishnyy T et al (2005) Phys Rev Lett 94
19. Campbell M, Sharp DN, Harrison MT, Denning RG, Turberfield AJ (2000) Nature 404:53
20. Deubel M, Wegener M, Kaso A, John S (2004) Appl Phys Lett 85:1895
21. Cumpston BH et al (1999) Nature 398:51
22. Ruhl T, Spahn P, Hellmann GP (2003) Polymer 44:7625
23. Xia YN, Gates B, Yin YD, Lu Y (2000) Adv Mater 12:693
24. Wang L, Baowen L (2008) Phys World 21:27
25. Wang J, Li Q, Knoll W, Jonas UJ (2006) Am Chem Soc 128:15606
26. Still T et al (2008) Phys Rev Lett 100:194301
27. Economou EN, Sigalas MJ (1994) Acoust Soc Am 95:1734
28. Meschede D (2006) Gerthsen Physik, 23 edn. Springer, Heidelberg
29. Ashcroft NW, Mermin ND (1976) Solid state physics. Thomson Learning, London
30. Wood AB (1941) Textbook of sound. Macmillan, New York
31. Gaunaurd GC, Wertman WJ (1989) Acoust Soc Am 85:541

32. Waterman PC, Truell RJ (1961) J Math Phys
33. Baumgartl J, Zvyagolskaya M, Bechinger C (2007) Phys Rev Lett 99:205503
34. Reinke D et al (2007) Phys Rev Lett 98:038301
35. Still T et al (2008) J Phys Condens Matter 20:404203
36. Gorishnyy T, Jang J-H, Koh C, Thomas EL (2007) Appl Phys Lett 91:121915
37. Harker AH, Temple JAG (1988) J Phys D Appl Phys 21:1576
38. Kafesaki M, Economou EN (1995) Phys Rev B 52:13317
39. Liu J, Ye L, Weitz DA, Sheng P (1990) Phys Rev Lett 65:2602
40. Jing X, Sheng P, Zhou M (1991) Phys Rev Lett 66:1240
41. Cheng W et al (2006) Macromolecules 39:9614
42. Gomopoulos N (personal communication)
43. Retsch M (2009) Complex materials via colloid crystallization. Ph.D. thesis
44. Phan S-E, Russel WB, Zhu J, Chaikin PM (1998) J Chem Phys 108:9789
45. Psarobas IE, Modinos A, Sainidou R, Stefanou N (2002) Phys Rev B 65
46. Goffaux C et al (2002) Phys Rev Lett 88
47. Yang SX et al (2002) Phys Rev Lett 88
48. Zhang XD, Liu ZY (2004) Appl Phys Lett 85:341
49. Yang SX et al (2004) Phys Rev Lett 93
50. Jang JH et al (2006) Adv Mater 18:2123
51. Penciu RS et al (2003) J Chem Phys 118:5224
52. Still T et al (2008) Phys Rev Lett 100:194301
53. Fustin CA, Glasser G, Spiess HW, Jonas U (2004) Langmuir 20:9114
54. Kuok MH et al (2003) Phys Rev Lett 90:255502
55. Penciu RS et al (2000) Phys Rev Lett 85:4622
56. Sainidou R, Stefanou N, Psarobas IE, Modinos AZ (2005) Z Kristallogr 220:848
57. Cheng W (2007) Hypersonic elastic excitations in soft mesoscopic structures. Ph.D. thesis
58. Tommaseo G et al (2007) J Chem Phys 126:014707
59. Johnson DL, Plona TJ (1982) J Acoust Soc Am 72:556
60. Yerazunis S, Cornell SW, Wintner B (1965) Nature 207:835
61. Stefanou N (personal communication)
62. Anderson PW (1958) Phys Rev 109:1492
63. Lagendijk A, van Tiggelen B, Wiersma DS (2009) Phys Today 24
64. Hu H et al (2008) Nat Phys 4:945
65. Kafesaki M, Economou EN (1999) Phys Rev B 60:11993
66. Sainidou R, Stefanou N, Psarobas IE, Modinos A (2005) Comp Phys Commun 166:197
67. Spahn P (2008) Ph.D. thesis, Technical University Darmstadt
68. Ruhl T, Spahn P, Winkler H, Hellmann GP (2004) Macromol Chem Phys 205:1385
69. Pursiainen OLJ et al (2008) Adv Mater 20:1484
70. Ruhl T, Hellmann GP Macromol (2001) Chem Phys 202:3502

Chapter 6
Smaller than Colloids: Characterization of Stable Organic Glass

6.1 Introduction

A wide range of packing structures are available to glasses, with more efficient packing leading to higher moduli materials [1]. Aging a glass allows for better packing and a higher modulus, but even long aging times increase the modulus by only a few percent [2, 3]; preparing high modulus materials in this manner is impractical. In this chapter it is shown that physical vapor deposition can be used to circumvent this kinetic limitation and produce glasses whose moduli exceed those of the ordinary glass by up to 19%. These high modulus glasses resist thermal treatment and take at least 10^4 times longer than the structural relaxation time to transform to the supercooled liquid. The ability to easily produce high modulus glasses will prove to be useful for fundamental investigations and coating technologies.

Unlike their crystalline counterparts, glasses have a nearly limitless array of packing arrangements. As a supercooled liquid is cooled, molecular motions eventually slow to such an extent that equilibrium cannot be maintained. Below this transition temperature T_g, a mechanically stable, non-equilibrium glass is formed. Glasses slowly evolve towards equilibrium (i.e., aging) in a process that optimizes packing and creates higher moduli materials. The structural relaxation time τ_α dictates the rate at which this process takes place, and due to the steep temperature dependence near T_g, τ_α is on the order of days only a few degrees below the glass transition temperature T_g. The aging process thus changes the moduli so slowly that in practice changes of only a few percent are possible [2, 3]. If high modulus amorphous materials are to be utilized for science and technology, new preparation techniques are needed which circumvent these kinetic restrictions and allow for more optimized amorphous packing [4].

6.2 BLS Experiments on IMC

This section shows that high modulus glass materials can be made efficiently with physical vapor deposition. Using this preparation technique, one can avoid the kinetic limitations of aging and prepare high modulus glasses in a matter of hours. Enhanced dynamics at the surface of amorphous materials allows for rapid configurational sampling in the top few nanometers [5–9]. Vapor deposition can build an efficiently packed amorphous material in a layer-by-layer fashion by taking advantage of the enhanced surface dynamics and thus is not limited by the slow relaxation dynamics of the bulk [10]. The mechanical properties of vapor-deposited films are determined using Brillouin light scattering (BLS) spectroscopy. Because of the non-destructive nature of BLS, the moduli of the as-deposited glass, the supercooled liquid, and ordinary glass (created by cooling the liquid) can be determined from a single sample.

Physical vapor depositions were performed by my coworker Kenneth Kearns in Prof. Mark Ediger's group at University of Wisconsin, Madison, separately on two organic glass-forming materials: indomethacin (IMC, $T_g = 315$ K) and tris-naphthylbenzene (TNB, $T_g = 348$ K). These two molecules are well-known glass-formers and their glasses have been previously prepared with physical vapor deposition [10–12]. During deposition, the temperature of the substrate $T_{substrate}$ and the deposition rate are the important control parameters. For this work, $T_{substrate}$ was held near $0.85 \, T_g$, i.e., 265 K for IMC and room temperature (≈ 295 K) for TNB. The rate of the deposition in all cases was 0.2 ± 0.03 nm/s. It has previously been shown that these deposition conditions produce glasses with low enthalpy, high density, and high kinetic stability [10–14]. $T_{substrate}$ was controlled by attaching the SiO_2 substrates to a copper temperature stage (Fig. 6.1a). The deposition rate was controlled by adjusting the temperature of the crucible. Further details are given in Methods (Chap. 3).

In the BLS experiment, the incident laser polarization was chosen to be perpendicular to the scattering plane. Scattered light polarized perpendicular and parallel to the incident polarization was measured in separate experiments, providing access to scattering from longitudinal and transverse phonons, respectively. The scattering from these two polarizations is shown in Fig. 6.1d for vapor-deposited IMC glass at 298 K (lower panel) and supercooled liquid IMC at 336 K (upper panel). Stokes and anti-Stokes shifts by the longitudinal (L) and transverse (T) phonons are observed to the left and right of the Rayleigh line region (shaded area), respectively. The vertical lines drawn on the Stokes side of the spectrum illustrate the temperature-independent scattering of the SiO_2 substrate and the temperature-dependent scattering of the IMC. The absence of longitudinal phonons in the transverse spectrum indicates no birefringence in the vapor-deposited film within the sensitivity.

The peaks in the BLS spectra provide access to the phase velocities $c_{l,t}$ for the L and T polarizations and through this route the moduli can be obtained. Spectra similar to those found in Fig. 6.1d were obtained at multiple temperatures for both
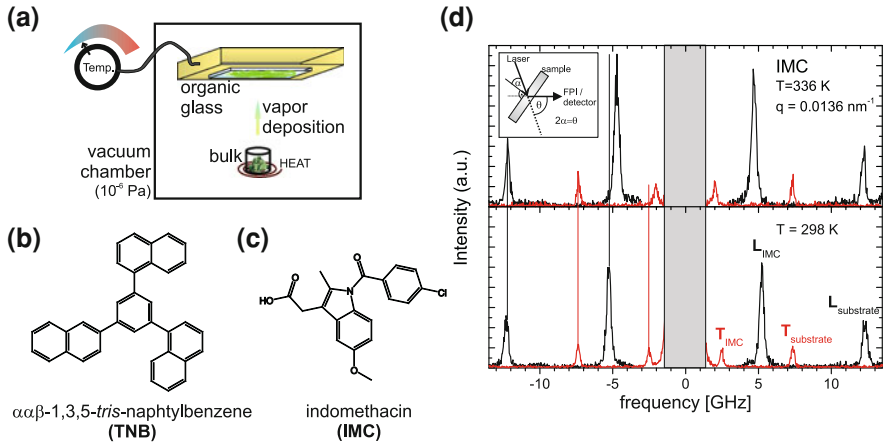
Fig. 6.1 **a** Schematic representation of the physical vapor deposition chamber with temperature controlled substrate. **b**, **c** Chemical structures of TNB and IMC, respectively. **d** Representative BLS spectra for a stable vapor-deposited IMC glass (*lower panel*) and supercooled liquid (*upper panel*) at the wave vector $q = 0.0136$ nm^{-1}. (*Inset* transmission scattering geometry with scattering angle θ of 70°.) The Rayleigh line region (*shaded area*) was removed for clarity. Both the longitudinal (L, *black*) and transverse (T, *red*) spectra are shown. Longitudinal and transverse phonon scattering for the IMC glass (L$_{IMC}$ and T$_{IMC}$, respectively) and amorphous SiO$_2$ substrate (L$_{substrate}$ and T$_{substrate}$, respectively) are indicated in the *lower panel*. The *vertical lines* drawn near the Stokes scattering peaks illustrate the difference between the supercooled liquid and as-deposited glass [15]

IMC and TNB. Each peak was fitted with a Lorentzian lineshape yielding the linewidth $\Gamma_{L,T}$ and the peak frequency $f_{l,t}$. The corresponding phase velocities $c_{l,t}$ for the L and T polarizations were calculated using $c_{l,t} = 2\pi f_{l,t}/q$, and are plotted in Fig. 6.2. Four experiments are shown in Fig. 6.2; in each case, the as-deposited stable glass was heated to a temperature above T_g, held isothermally until equilibrium was attained, then further heated, and finally cooled. During the initial heating of the stable glass (SG), c_l and c_t have high values as compared to the ordinary glass (OG), indicating high moduli. During isothermal annealing above T_g (arrow 2), significant decreases in the phase velocities are observed. This change, discussed in detail below, signifies the transformation of the stable glass into the supercooled liquid (SCL). Once the transformation is complete, the sample, now a supercooled liquid, is heated still higher and then cooled to 295 K (arrows 3 and 4). A characteristic kink in the temperature-dependent phase velocity indicates T_g and the value obtained is in reasonable agreement with the value obtained from differential scanning calorimetry [11, 12].

From the phase velocities $c_{l,t}$ in Fig. 6.2, the moduli of the stable glass and the ordinary glass can be calculated. The longitudinal bulk modulus $M = \varrho c_l^2$, the shear modulus $G = \varrho c_t^2$ and the commonly used Young's modulus $E = 9MG/(3M + G)$ can all be determined from c. For the stable as-deposited glass of IMC, M, G, and E moduli were determined to be 8.3, 1.7, and 4.9 GPa at T_g,
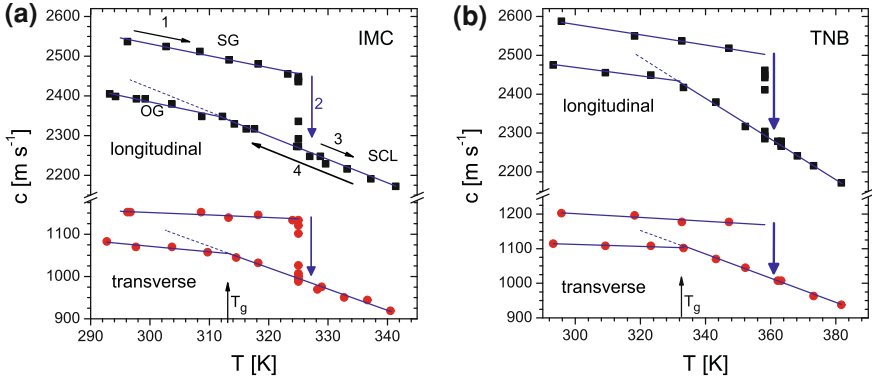
Fig. 6.2 **a** Temperature dependence of phase velocity c for IMC. The longitudinal (*squares*) and transverse (*circles*) c are shown for the stable as-deposited glass (*SG*), the supercooled liquid (*SCL*), and the ordinary glass (*OG*). *Arrows* indicate the progression of the heating and cooling cycles. *Arrow 2* indicates the isothermal transformation of the SG to the SCL at $T_g + 10$ K. **b** Temperature dependent longitudinal and transverse c of TNB for the SG, OG and SCL. The thermal cycle is similar to the one described for **a** [15]

respectively. The moduli calculated for the ordinary glass of IMC are smaller than those obtained for the stable glass samples. At 312 K, M for the stable as-deposited IMC glass is 14% greater than the ordinary glass while G and E are 19% greater. A similar situation holds for TNB where M, G, and E are 10, 15, and 14% greater, respectively, for the stable glass samples as compared to the ordinary glass. To obtain these values, the published densities of 1.31 g/cm^3 for IMC [16] and 1.16 g/cm^3 for TNB [17] were used. The stable as-deposited glass was assumed to be 1.5% more dense than the ordinary glass in accordance with previous measurements on TNB vapor-deposited under similar conditions [10, 14]. Notably, the Poisson ratio σ has the same value (0.36 ± 0.01) in both stable and ordinary glass samples and increases for the supercooled liquid as expected [18].

In contrast to the results presented here, aging experiments on glass-forming systems show only small improvements in mechanical properties during aging. BLS experiments were performed on glycerol by quenching from above T_g to T_g −4.2 K; in this experiment, a 0.6% increase in modulus was achieved over 20 days [3]. For silicone oil, temperature down-jumps of 1.5 K near T_g resulted in a 2.7% increase in the modulus during the 10^4 s equilibration time [2]. Based on calorimetry measurements [10, 12], it was previously estimated that IMC and TNB samples vapor-deposited under the conditions utilized here have properties similar to those expected after aging an ordinary glass for more than 300 years. Thus it is not surprising that aging for hours or days does not produce the large modulus changes reported here. Pressurization experiments have been shown to change moduli by up to 20%, but this effect is reversible and upon pressure release, the system reverts back to the ordinary glass value rendering it of little use for potential applications [19].

Notably, the high modulus IMC and TNB glasses produced by vapor-deposition exhibit remarkable thermal stability. Figure 6.3a and b shows the change in c_l and c_t for vapor-deposited IMC during isothermal annealing above T_g. In these experiments, the temperature of the stable as-deposited glass was increased to 325 K in about 15 min and then held for several hours. Both phase velocities (and moduli) remain relatively unchanged for the first 120 min of the experiment. After this induction time, the phase velocities begin to decrease from the high values of the stable glass to the supercooled liquid values. Approximately 200 min is needed to complete the transformation to the supercooled liquid. To put this value into context, the structural relaxation time τ_α of the IMC supercooled liquid at 325 K is about 1 s based on dielectric spectroscopy studies [20]; thus the isothermal transformation of stable vapor-deposited IMC into the supercooled liquid requires about $10^4 \tau_\alpha$. Similar results are obtained for TNB where the stable as-deposited glasses required $10^{4.8}\tau_\alpha$ to transform into the supercooled liquid at 358.2 K [21].

Conceptually similar experiments have been performed on ordinary glasses that have stabilized by aging. For example, Kovacs aged poly(vinyl acetate) for 2 months below T_g and then performed dilatometry during isothermal annealing above T_g. He observed the transformation into the supercooled liquid in a period of
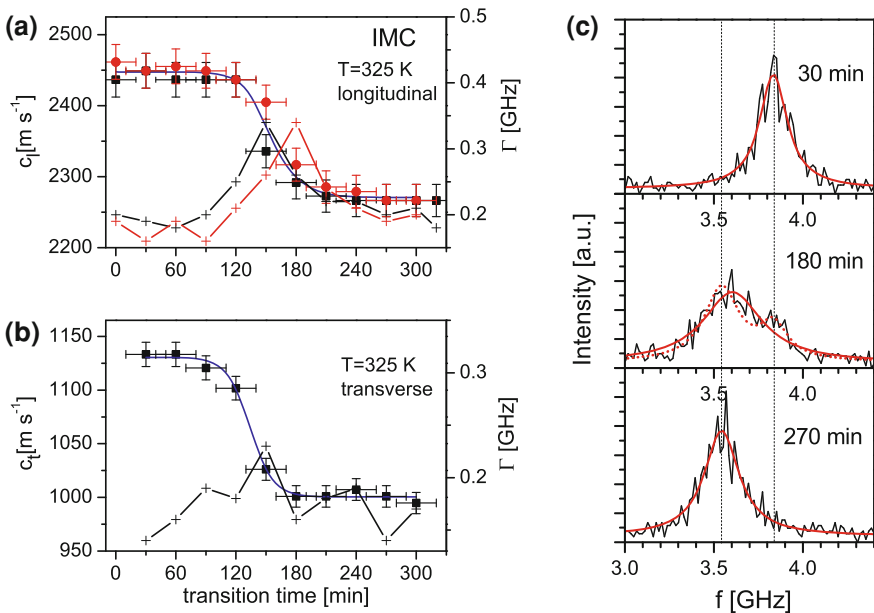
Fig. 6.3 BLS experiments on vapor-deposited IMC glasses during isothermal annealing above T_g (325 K). **a** Longitudinal, c_l, and **b** transverse, c_t, phase velocity changes as a function of time. Sigmoidal fits are given as guides to the eye. Two different samples (*squares* and *circles*) are shown in **a** to demonstrate the reproducibility of the transformation. In **a** and **b**, the full width at half height linewidth, Γ, is shown as crosses. **c** Spectral line shapes and Lorentzian fits (*solid lines*) at three different times during isothermal annealing [15]

$35\tau_\alpha$ [22]. Thus, in comparison to glasses prepared by cooling a liquid and then aging, the vapor-deposited IMC and TNB samples maintain their extraordinarily high modulus for a remarkably long time.

Changes observed in the BLS spectral linewidth during isothermal annealing provide insight into the mechanism by which the stable glass transforms into the supercooled liquid. Figure 6.3a shows that a maximum in Γ is reached near the midpoint of the transformation (Γ is read from the right axis). A similar feature is observed in Fig. 6.3b although the smaller signal of the transverse scattering makes this less apparent. The observation of a change in Γ during the transformation of a glass to a liquid is unprecedented. The increase in Γ indicates that the sample is heterogeneous on the 500 nm ($\sim 2\pi/q$) length scale during the transformation. Figure 6.3 shows the BLS spectral lineshapes at three times during isothermal annealing at 325 K. Before the transition begins (30 min) and after the transition ends (270 min), narrow lines are observed. In contrast, near the midpoint of the transformation (180 min), a broad line is observed. The shape of the line suggests that the sample is a mixture of the supercooled liquid and the stable glass at this stage. This point is illustrated by the dotted red curve in Fig. 6.3c which is a linear combination of narrow lineshapes from the 30 min (stable glass) and 270 min (supercooled liquid) data. This conclusion is consistent with a recent quasi-isothermal differential scanning calorimetry study of these materials [13]. While that work suggested that stable glasses transform to the supercooled liquid via two-phase intermediate state, the spatial extent of these regions (at least 500 nm) has not been known prior to this BLS study.

Significantly increasing the modulus of amorphous solid materials using conventional aging methods is a time consuming and ineffective process. The work presented in this chapter shows that physical vapor deposition can be used to prepare glasses with moduli that are as much as 19% greater than those made by cooling the liquid. These glasses resist thermal treatment and retain their high modulus values for at least 10^4 times longer than the structural relaxation time of the glass at temperatures significantly above T_g. During this slow transformation, a mixture of supercooled liquid and glass is observed on length scales greater than 500 nm. High modulus vapor-deposited glasses may prove useful for applications because of their remarkable mechanical properties but also their extraordinary thermal stability. Given the known correlation between amorphous packing and modulus, new insights into this packing could be realized through fundamental studies of these materials.

6.3 Materials and Methods

6.3.1 Stable Glass

IMC and TNB stable glass films were prepared by my coworker Kenneth Kearns at University of Wisconsin in Madison, WI.

IMC was purchased from Sigma Aldrich and was used without further purification. TNB was synthesized by McMahon and co-workers using published methods [23]. SiO_2 substrates (5 mm diameter and 0.15 mm thick, Fisher Scientific coverglass) were attached to a copper temperature stage using double-sided conductive carbon black tape (SPI Supplies). The temperature of the substrate during deposition was controlled using a Lakeshore 340 temperature controller. To deposit the IMC and TNB glass films, a quartz crucible containing the crystalline material was heated inside a vacuum chamber ($\sim 10^{-8}$ torr) such that the desired rate of 0.2 nm/s was achieved. The rate of deposition was controlled by maintaining the temperature of the quartz crucible, and the rate was monitored with a quartz crystal microbalance (Sycon instruments). Deposition continued until a 10–15 µm film was deposited. After deposition, the substrates were removed from the deposition chamber, placed in desiccant and stored in dry ice prior to analysis.

6.3.2 BLS Measurements

BLS was performed in a transmission geometry to obtain the phase velocity and thus modulus values. The transmission, as opposed to the commonly used reflective geometry, was used to remove the influence of refractive index on the measurements, and the details of this geometry are described in detail elsewhere [24–26]. For all experiments, the sample holder was initially flushed with argon gas and desiccant was placed in the holder to eliminate any possible plasticization by atmospheric water [27, 28]. The sample temperature was monitored with a platinum RTD and controlled to within 0.5 K with a temperature controller which was built in-house. For each data point in Fig. 6.2, the temperature was allowed to stabilize for 15 min and then the BLS spectra were acquired for 5 min. The heating/cooling rate between each temperature measurement was approximately 2–3 K/min. The temperature history establishes an effective heating/cooling rate of approximately 0.1 K/min. For isothermal experiments, the temperature was changed from room temperature to the annealing temperature in 15–20 min.

References

1. Dyre JC, Olsen NB, Christensen T (1996) Phys Rev B 53:2171
2. Olsen NB, Dyre JC, Christensen T (1998) Phys Rev Lett 81:1031
3. Miller RS, MacPhail RA (1997) J Chem Phys 106:3393
4. Royall PC, Williams SR, Ohtsuka T, Tanaka H (2008) Nat Mater 7:556
5. Forrest JA, Dalnoki-Veress K, Stevens JR, Dutcher JR (1996) Phys Rev Lett 77:2002
6. Keddie JL, Jones RAL, Cory RA (1994) Faraday Discuss 98:219
7. Fakhraai Z, Forrest JA (2008) Science 319:600
8. Bell RC et al (2003) J Am Chem Soc 125:5176
9. Ellison CJ, Torkelson JM (2003) Nat Mater 2:695

10. Swallen SF et al (2007) Science 315:353
11. Kearns KL et al (2007) J Chem Phys 127:154702
12. Kearns KL et al (2008) J Phys Chem B 112:4934
13. Kearns KL, Still T et al (2010) Adv Mater 22:39
14. Kearns KL et al (2009) J Phys Chem B 113:1579
15. Swallen SF et al (2008) J Chem Phys 128:214514
16. Yoshioka M, Hancock BC, Zografi G (1994) J Pharm Sci 83:1700
17. Plazek DJ, Magill JH (1966) J Chem Phys 45:3038
18. Novikov VN, Sokolov AP (2004) Nature 431:961
19. Bezot P, Hesse-Bezot C (1990) J Non-Cryst Solids 122:160
20. Carpentier L, Decressain R, Desprez S (2006) J Phys Chem B 110:457
21. Richert R, Duvvuri K, Duong L-T (2003) J Chem Phys 118:1828
22. Kovacs AJ (1963) Fortschr HochpolymForsch 3:394
23. Bonvallet PA et al (2007) J Org Chem 72:10051
24. Still T et al (2008) J Phys Condens Matter 20:404203
25. Cheng W et al (2007) Macromolecules 40:7283
26. Penciu RS et al (2003) J Chem Phys 118:5224
27. Andronis V et al (1997) J Pharm Sci 86:346
28. Dawson KJ et al (2009) J Phys Chem B 113:2422

Chapter 7
Concluding Remarks

7.1 Conclusions

Colloidal self-assembly by vertical lifting is a potential and versatile method to create and design artificial sub-micron periodic structures of hard (e.g., SiO_2) and soft (polymers) colloidal particles. The fabrication of high quality crystals as well as the creation of artificial glasses by the introduction of structural disorder is possible. Such structures have spatial dimensions of their components in the order of the wavelength of visible light, hence they act as artificial opals. In addition, they show interesting phononic properties in the hypersonic (GHz) range.

Brillouin light scattering (BLS) is found to be a powerful technique to measure the elastic properties of nanostructured materials at hypersonic frequencies. In case of dry, non-transparent, multiple scattering colloidal samples, BLS measures **q**-independent localized modes of the individual spheres. In particular, for soft spheres these spectra are found to be richer with increasing diameter. This finding is explained by theoretical and geometrical considerations. Nearly all predicted modes (especially those that appear at frequencies significantly below that of the acoustic phonon in the back-scattering case) are found experimentally and assigned to their corresponding spheroidal eigenmodes. The analysis of the eigenmode spectra yields the longitudinal c_l and transverse sound velocity c_t, allowing the calculation of the Young and shear elastic moduli at the nanoscale. Additionally, the analysis of the line shape can provide information on the size polydispersity and on interactions with surrounding medium [1, 2].

Based on the studies of several binary colloidal mixtures, the eigenfrequencies do not depend on the crystalline order or on the kind and number of the neighboring spheres (Sect. 4.2.2 in Chap. 4). Only in the extreme case of dilute large spheres in a sea of small spheres a small blue shift was observed [1]. On the open discussion with regard the eigenmode BLS activity [3, 4], density of states and finite element calculations have shown that all eigenmodes (n, l) can contribute to the light scattering spectrum of spheres with diameter in the order of magnitude of the probing laser wavelength. The limitation on even 'quantum numbers' l, as claimed

by others, is disputed (Sect. 4.2.1 in Chap. 4). Further, the utilization of densely packed silica spheres in an index matching liquid led to the first verification of the theoretical predictions for the **q**-dependent amplitude of the eigenmode spectrum; the frequency of these localized modes is expectedly **q**-independent.

After these fundamental questions concerning the spectrum of the resolved modes in homogeneous colloidal spheres have been convincingly addressed, the effect of the elastic constants on the particle vibrational modes was best addressed in the case of random copolymer (PMMA-PnBA) spherical particles, where the elastic constants vary with the composition (Sect. 4.2.3 in Chap. 4). The randomness of the copolymer and the amorphous state of the particle was verified by the presence of single T_g by DSC, further confirmed by the single a-relaxation obtained by dielectric spectroscopy, i.e., both kind of segments feel the same energy landscape. The systematic red shift of the eigenfrequencies with increasing composition of the softer (PnBA) component as well as the effective medium velocities measured in bulk copolymer films were theoretically captured when a higher 'effective glassy sound velocity' was assumed for the PnBA in the copolymer than in its bulk state.

Two additional elaborate BLS experiments on nanostructured core–shell hybrid systems were presented herein: (1) hard silica colloids surrounded by a soft polymer shell show eigenmode spectra that are dominated by the scattering from the soft polymer shell (larger compressibility). Nevertheless, due to the boundary conditions and displacements in the composite material, it becomes feasible the extraction of the elastic constants in parts, core and shell at the nano- and mesoscale. The spatial confinement causes a hardening of the thin polymer chain (Sect. 4.2.2 in Chap. 4) [5]; (2) in the inverse particle architecture, where the polymeric core is embraced by a thin silica shell, the former dominates the eigenmode spectrum. A temperature dependent study has revealed a striking hardening of the polymeric core as compared to the bare polymer spheres implying a modified glassy state under confinement. The glass transition temperature T_g of the core, however, remained virtually constant whereas the thin silica shell assured a robust shape persistent polymeric core at temperatures well above its T_g ('nano armor', Sect. 4.3.1 in Chap. 4) [6].

Since the hypersonic phonons are in the order of magnitude of few hundreds nanometers, they do not only probe the effective medium structured in a molecular scale (like in the copolymers), but also in the mesoscale. By infiltration of the dry samples with a liquid close to optical matching, it is possible to overcome the multiple light scattering and, by that, to get access to the collective acoustic behavior of the colloidal systems. Pure effective medium behavior is observed by BLS for such systems in the long wavelength limit, i.e., for small q's, where the phonon wavelength exceeds the structure length of the colloidal system. Section 5.1.2 in Chap. 5 presents a short overview over the most important established effective medium theories, while in Sect. 5.2 in Chap. 5 their applicability on a system of defect doped liquid infiltrated opals is presented.

At higher q's, BLS can be used to record directly the dispersion relations that led to the first demonstration of a distinct hypersonic Bragg gap at the edge of the

first Brillouin zone of a colloidal crystal by Cheng et al. [7]. In this thesis, the resonant character of the particles was realized to demonstrate, for the first time, the presence of an additional band gap—the hybridization gap, theoretically predicted six years earlier. This HG originates from the interaction of the acoustic band of the effective medium and bands from the multipole modes of the individual particles (Sect. 5.3.1. in Chap. 5), i.e., the eigenmodes. Hence, its realization demonstrates the strong correlations between the individual colloid's elastic properties (the 'music') and the phononic characteristics of the ensemble (the 'concert'). For polymer colloids infiltrated with an index matching liquid like PDMS or silicon oil, the HG is found to open up at frequencies below that of Bragg gap.

Increase of the mechanical mismatch by going from soft to hard opals based on silica spheres significantly changes the propagation characteristics (Sect. 5.4 in Chap. 5). This includes an unseen bending in the band diagram of polycrystalline silica colloids in a liquid matrix as well as a Bragg gap, which is peculiarly robust against structural deformation, in silica/rubber phoXonic films.

7.2 Outlook

Phononic materials might have interesting potential applications starting with the obvious use as acoustic shields or vibration isolators. However, for most practical applications, gap frequencies in the range of sonic or ultrasonic seem to be of higher interest than those in the hypersonic range. On the other hand, if the blocked phonon's wavelength is comparable to the structure dimensions, i.e., $\lambda \sim d$ then the structure's components for ultrasonic devices must be near to the millimeter-range and even larger to stop sound between kHz and Hz. The ultimate goal would be to create materials, which can realize gaps at wavelengths much larger then the inherent length scale of the gap material ($\lambda \gg d$). Ping Sheng and coworkers demonstrated an approach going in this direction [8]. They prepared locally resonant sonic materials by combining a spherical lead core and a silicone rubber coating in the millimeter size range and building up a crystal out of these. The resulted superstructure exhibits a band gap around 400 Hz, which corresponds to a wavelength two orders of magnitude bigger than the diameter of the spheres. Like HG the explanation is due to localized modes mostly in the soft shells. Advances in colloidal science can be utilized to provide materials with new functions. For example core–shell particles with varying composition, hybrid materials, or materials with even hierarchical order can allow tailoring the phononic properties of small but smart materials to frequencies, where a broad range of applications is conceivable.

When we turn our attention back to the manipulation of the phonon flow in the GHz range, hypersonic phononic materials hold promise to control heat flow in insulators and semiconductors. The typical phonon wavelength responsible for the heat transport is even smaller (≈ 10 nm) than the structures investigated in this

thesis. If we will control the flow of elastic energy by building phonon guiding devices in full analogy to the lossless light guidance in photonics or by building devices with a strong anisotropy of phonon transmission, we can also attain new knowledge in advanced heat management. In this direction, colloidal science could offer new materials, e.g., multilayer structures with different particle sizes in each structure that could split and direct the elastic energy. Other analogies to photonics, e.g., acoustic superlenses already exist [9], but still impose challenges for high frequency acoustics. It should be mentioned that hypersonic phononics can simultaneously act as photonics for wavelengths in the visible spectrum allowing the realization on photonic and phononic band gaps at the same time (PhoXonics) [10]. The coupling of optical and mechanical degrees of freedom can be applied to influence the optomechanical dynamics of small systems, utilizing the radiation pressure of light [11]. The upper frequency limit for such systems is, so far, in the MHz-range, however, colloidal systems like those presented in this thesis may expand the investigation of such effects to the GHz-range, giving raise to novel fascinating phenomena.

In parallel to the development of materials with new phononic functions, there is also a need for new experimental techniques to measure the band diagrams of non-transparent structures exhibiting also strong phononic gaps. BLS is a powerful technique for transparent samples with serious shortcomings in opaque systems such as dry opals and in measuring hypersonic transmission spectra. The main problem is the availability of a selective and continuous generation of phonons in the GHz-range, which will be hopefully overcome in the near future.

References

1. Still T et al (2008) J Phys Condens Matter 20:404203
2. Cheng W et al (2005) J Chem Phys 123:121104
3. Montagna M (2008) Phys Rev B 77:045418
4. Li Y et al (2008) Chem Phys Lett 461:111
5. Still T et al (2008) Nano Lett 8:3194
6. Still T, D'Acunzi M, Vollmer D, Fytas G (2009) J Coll Int Sci 340:42
7. Cheng W et al (2006) Nat Mater 5:830
8. Liu ZY et al (2000) Science 289:1734
9. Zhang XD, Liu ZY (2004) Appl Phys Lett 85:341
10. Maldovan M, Thomas EL (2006) Appl Phys Lett 88:251907
11. Kippenberg TJ, Vahala KJ (2008) Science 321:1172

Chapter 8
Appendix: Scattering Geometry

8.1 Transmission Case

Since Brillouin light scattering (BLS) is a quasi-elastic scattering technique, incident and scattered wave vector can be regarded as of equal length (Fig. 8.1):

$$|\mathbf{k}_i| = |\mathbf{k}_s| = \frac{2\pi n}{\lambda}. \tag{8.1}$$

With Snell's law:

$$n \sin \beta = \sin \alpha \Rightarrow \beta = \sin^{-1}\left(\frac{1}{n}\sin \alpha\right), \tag{8.2}$$

$$n \sin \gamma = \sin \theta - \alpha \Rightarrow \gamma = \sin^{-1}\left(\frac{1}{n}\sin \theta - \alpha\right). \tag{8.3}$$

The length of the scattering wave vector $\boldsymbol{q}$ is the length of the third side of the isosceles triangle spanned by $\boldsymbol{k}_i$ and $\boldsymbol{k}_s$. Dividing it into two right-angled triangles allows to apply simple trigonometric rules:

$$q = |\boldsymbol{q}| = 2\frac{2\pi n}{\lambda}\sin\frac{\beta + \gamma}{2} \tag{8.4}$$

and with Eqs. 8.2 and 8.3

$$q = \frac{4\pi n}{\lambda}\sin\left[\frac{1}{2}\left(\sin^{-1}\left(\frac{1}{n}\sin(\theta - \alpha)\right) + \sin^{-1}\left(\frac{1}{n}\sin \alpha\right)\right)\right]. \tag{8.5}$$

Under the distinct condition that the incident angle α is half the scattering angle, $\boldsymbol{q}$ becomes equal to its component parallel to the surface, and Eq. 8.5 can be further simplified for this special case:

$$q = q_{\mathrm{para}} = |\boldsymbol{q}_{para}| \quad \text{for} \quad \gamma = \beta \Rightarrow \theta = 2\alpha \tag{8.6}$$

Fig. 8.1 Transmission geometry

$$q_{\text{para}} = \frac{2\pi n}{\lambda}(\sin\beta + \sin\gamma) \tag{8.7}$$

$$q_{\text{para}} = \frac{2\pi}{\lambda}(\sin\alpha + \sin(\theta - \alpha)) = \frac{4\pi}{\lambda}\sin\frac{\theta}{2}. \tag{8.8}$$

In the last equation, valid only in this special case, the refractive index disappears.

8.2 Reflection Case

Starting from the same point as in the transmission geometry,

$$|\mathbf{k}_i| = |\mathbf{k}_s| = \frac{2\pi n}{\lambda}, \tag{8.9}$$

applying Snell's law and the internal angle of a triangle, we can define a couple of angles shown in Fig. 8.2:

$$\beta = \sin^{-1}\left(\frac{1}{n}\sin\alpha\right) \tag{8.10}$$

$$\gamma = 180° - \alpha \tag{8.11}$$

$$\rho = 180° - (90° - \beta) - \epsilon = 90° + \beta - \epsilon \tag{8.12}$$

$$\epsilon = 90° - \delta \tag{8.13}$$

$$n\sin\delta = \sin 180° - \theta - \alpha \tag{8.14}$$

Now it is possible to express the angle γ in the sample between $\mathbf{k}_i$ and $\mathbf{k}_s$ as a function of α and θ

Fig. 8.2 Reflection geometry

$$\gamma = 180° - 90° - \sin^{-1}\left(\frac{1}{n}\sin\alpha\right) + \left(90° - \sin^{-1}\left(\frac{1}{n}\sin\left(180° - \theta - \alpha\right)\right)\right)$$

$$= 180° - \sin^{-1}\left(\frac{1}{n}\sin\alpha\right) - \sin^{-1}\left(\frac{1}{n}\sin\left(\theta + \alpha\right)\right),$$

$$(8.15)$$

and q turns out to become:

$$q = \frac{4\pi n}{\lambda}\sin\left[\frac{1}{2}\left(180° - \sin^{-1}\left(\frac{1}{n}\sin\alpha\right) - \sin^{-1}\left(\frac{1}{n}\sin\left(\theta + \alpha\right)\right)\right)\right]$$

$$= \frac{4\pi n}{\lambda}\cos\left[\frac{1}{2}\left(\sin^{-1}\left(\frac{1}{n}\sin\alpha\right) + \sin^{-1}\left(\frac{1}{n}\sin\left(\theta + \alpha\right)\right)\right)\right]$$

$$(8.16)$$

The angle η between q and k_i or k_s is

$$\eta = \frac{180° - \gamma}{2}$$

$$= \frac{1}{2}\left[\sin^{-1}\left(\frac{1}{n}\sin\alpha\right) + \sin^{-1}\left(\frac{1}{n}\sin\left(180° - \theta - \alpha\right)\right)\right].$$

$$(8.17)$$

Using this equation, the relation between q and its component perpendicular to the surface, q_{perp}, can be expressed again as a function of the two angles θ and α,

$$\frac{q_{\text{perp}}}{q} = \cos\left(\beta - \eta\right)$$

$$= \cos\left[\sin^{-1}\left(\frac{1}{n}\sin\alpha\right) - \frac{1}{2}\left\{\sin^{-1}\left(\frac{1}{n}\sin\alpha\right) + \sin^{-1}\left(\frac{1}{n}\sin\left(\theta + \alpha\right)\right)\right\}\right]$$

$$= \cos\left[\frac{1}{2}\left\{\sin^{-1}\left(\frac{1}{n}\sin\alpha\right) - \sin^{-1}\left(\frac{1}{n}\sin\left(\theta + \alpha\right)\right)\right\}\right]$$

$$(8.18)$$

and q_{perp} becomes

$$
\begin{aligned}
q_{perp} &= q \cdot \cos\left(\beta - \eta\right) \\
&= \frac{4\pi n}{\lambda} \sin\left[\frac{1}{2}\left\{180° - \sin^{-1}\left(\frac{1}{n}\sin\alpha\right) - \sin^{-1}\left(\frac{1}{n}\sin\left(\theta + \alpha\right)\right)\right\}\right] \quad (8.19) \\
&\times \cos\left[\frac{1}{2}\left\{\sin^{-1}\left(\frac{1}{n}\sin\alpha\right) - \sin^{-1}\left(\frac{1}{n}\sin\left(\theta + \alpha\right)\right)\right\}\right].
\end{aligned}
$$

By comparison with Eq. 8.16 it is clear that $q = q_{perp}$ if the last term on the right side becomes one. Due to the periodicities of the inverse sine function, this is the case for

$$
\alpha = \frac{\theta - 180°}{2}. \quad (8.20)
$$

i.e., when chosing this special geometry in the BLS experiment, the wave vector lies fully perpendicular to the substrates surface. However, the careful comparison with Fig. 2.6 in Chap. 2 shows that the fulfillment of this geometry would lead to a reflection of the laser directly into the Fabry–Pérot. Therefore, only geometries very near to that can be chosen in practice, in order not to destroy the detector, and the qs probed in reflection geometry are only approximately equal to the q_{perp}s.

Curriculum Vitae

Tim Still
Date of Birth: April 3, 1982
Place of Birth: Neuwied, Germany
Nationality: German
ResearcherID: A-3286-2009

Since November 2009
Max Planck Institute for Polymer Research, Mainz, Germany
Postdoctoral Researcher

March 2007–November 2009
Max Planck Institute for Polymer Research, Mainz, Germany
Promotion by Johannes Gutenberg University Mainz
Degree obtained: Doctor in Natural Science (Dr. rer. nat.)

April 2002–January 2007
Institute for Physical Chemistry, Department of Chemistry, Philipps University Marburg, Germany
Degree obtained: Diploma in Chemistry (Dipl. Chem.)
Thesis: Inelastische Neutronenstreuung an geschmolzenen Natriumhaliden

Publications

2010

(8) T. Still, D. Kiefer, G. Fytas, N. Stefanou,... *Collective Hypersonic Excitations in Strongly Multiple Scattering Colloids*, under review.

(7) F. Stadler, T. Still, G. Fytas, C. Bailly, *Elongational Rheology and Brillouin Light Scattering of Entangled Telechelic Polybutadiene Based Temporary Networks*, under review.

(6) T. Still, M. Retsch, U. Jonas, R. Sainidou, P. Rembert, K. Mpoukouvalas, G. Fytas, *Vibrational Eigenfrequencies and Mechanical Properties of Mesoscopic Copolymer Latex Particles*. Macromolecules 2010, **43**, 3422.

(5) K. Kearns, T. Still (equal contribution), G. Fytas, M. D. Ediger, *High-Modulus Organic Glasses Prepared by Physical Vapor Deposition*. Adv. Mater. 2010, **22**, 39.

2009

(4) T. Still*, M. D'Acunzi, D. Vollmer, G. Fytas, *Mesospheres in Nano-Armor: Probing the Shape-Persistence of Molten Polymer Colloids*. J. Coll. Interf. Sci. 2009, **340**, 42.

2008

(3) T. Still, R. Sainidou, M. Retsch, U. Jonas, P. Spahn, G. P. Hellmann, G. Fytas, *The Music of Core-Shell Spheres and Hollow Capsules: Influence of the Architecture on the Mechanical Properties at the Nanoscale*. Nano Lett. 2008, **8**, 3194 (with 'Top down, Bottom up' in Nature Nanotech. 2008, **3**, 614).

(2) T. Still, W. Cheng, M. Retsch, U. Jonas, G. Fytas, *Colloidal Systems: A Promising Material Class for Tailoring Sound Propagation at High Frequencies*. J. Phys. Condens. Matt. 2008, **20**, 404203.

(1) T. Still, W. Cheng, M. Retsch, R. Sainidou, J. Wang, U. Jonas, N. Stefanou, G. Fytas, *Simultaneous Occurrence of Structure-Directed and Particle-Resonance-Induced Phononic Gaps in Colloidal Films*. Phys. Rev. Lett. 2008, **100**, 194301.

Presentations in International Conferences

2009

ICPPP 15, Leuven, Belgium, 07/20–23/2009:
T. Still, A. Sato, G. Fytas (**oral presentation**): *Tailoring Phonon Propagation by Mesoscopic Engineering of Soft Matter*
APS March Meeting, Pittsburgh, PA, USA, 03/16–20/2009:
T. Still, R. Sainidou, G. Hellmann, G. Fytas (**oral presentation**): *The 'Music' of Silica-Poly(methyl methacrylate) Core-Shell Spheres: Eigenvibrations and Mechanical Properties at the Nanoscale*

K. L. Kearns, T. Still, G. Fytas, M. D. Ediger (poster): *Brillouin Light Scattering Measurements of High Modulus Glasses Produced by Physical Vapor Deposition*

Makromolekulares Kolloquium 2009, Freiburg, Germany, 02/26–28/2009:
M. Retsch, T. Still, W. Cheng, R. Sainidou, U. Jonas, N. Stefanou, G. Fytas (poster): *Phononic Properties of Colloidal Particles and Nanostructured Films*

2008

16th Ostwald Colloquium, Leipzig, Germany, 09/22–24/2008:
T. Still, M. Retsch, R. Sainidou, U. Jonas, G. Fytas (**oral presentation**): *High Frequency Acoustics in Colloidal Systems by Spontaneous Brillouin Light Scattering*

Son et lumière 2008, Cargèse, Corse, France, 01/01–13/2008:
T. Still, M. Retsch, R. Sainidou, W. Cheng, U. Jonas, G. Fytas (**oral presentation +** poster): *GHz Acoustics in Colloidal Systems by Spontaneous Brillouin Light Scattering*

Acoustics'08, Paris, France, 06/29–07/04/2008:
T. Still, M. Retsch, R. Sainidou, U. Jonas, G. Fytas (**oral presentation**): *High Frequency Acoustics in Colloidal Systems by Spontaneous Brillouin Light Scattering* (J. Acoust. Soc. Am. 2008, **123**, 3555)

Index